Blunt, Matthew Oliver (2007) Far-from-equilibrium nanoparticle assemblies : patterns, transport and dynamics. PhD thesis, University of Nottingham.

Far-From-Equilibrium Nanoparticle Assemblies: Patterns, Transport and Dynamics.

Matthew Oliver Blunt, MSci.

Thesis submitted to the University of Nottingham
for the degree of Doctor of Philosophy

February 2007

Abstract

This work is centered on the study of self-organisation and pattern formation in a prototypical nanostructured system, namely colloidal nanoparticle assemblies. The particular system chosen for investigation, Au nanocrystals spin cast onto silicon substrates from a solvent, despite being chemically rather simple exhibits a rich variety of complex patterns. In the majority of experiments discussed in this thesis, far-from-equilibrium conditions are attained by a spin-casting process which drives rapid solvent evaporation.

A systematic study was carried out to determine the various factors affecting the morphology of nanoparticle assemblies produced in this manner. These factors include the concentration of the nanoparticle solution, the particular solvent used, and the chemical/physical nature of the substrate. Changing these variables can affect both the strength of interactions between individual nanoparticles and between nanoparticles and the substrate. The various morphologies of the nanoparticle structures produced were studied using atomic force microscopy (AFM).

Particular attention is paid to the role of the substrate's surface chemistry in pattern selection. A range of different substrates are used to gauge the influence of differing surface chemistries. In addition, scanning probe lithography was employed to microscopically pattern surfaces. This facilitated the observation of effects caused by the presence of two radically different surface chemistries in the micron size range. This patterning process provides the experimenter some measure of control over the morphology of the nanoparticle assembly, allowing the enforcement of predefined length scales onto the network. Simulations of drying nanocrystal films produced using code written by Martin *et al* [1] have been shown to accurately reproduce the experimental results. These simulations are used to develop theoretical explanations of the experimental data in terms of the varying solvent evaporation rate on the substrate and the manner by which the solvent dewets on chemically and topologically differing areas of a surface.

A remarkable probe-induced coarsening of nanoparticle assemblies by repetitive scanning with an AFM probe has been studied. Repeated scanning

of colloidal nanoparticle systems causes the irreversible growth of nanoparticle assemblies. The size distribution of structures produced by this growth is shown to be self-similar. With the size of the domains growing with a power law dependence on scan time. From a combination of these results the growth of structures is explained using a model of coarsening based on cluster diffusion and coalescence. This model is subtly different from coalescence in a thermally driven system due to the novel nature of the mechanical coarsening process.

Electrical transport through different array morphologies produced via the spin-coating process was studied using D.C. electrical measurements and electrostatic force microscopy (EFM). Measurements over temperatures ranging from 4.5K to room temperature were made. Variations in the manner that power law scaling of the conduction behaviour alters for different arrays is linked to the topological characteristics of the arrays.

List of publications

C. P. Martin, M. O. Blunt, P. J. Moriarty, **Nanoparticle networks on silicon: Self-organized or disorganized?** *Nano. Lett.* **4**, no.12, pp.2389-2392, **(2004)**.

M. O. Blunt, M. Suvakov, F. Pulizzi, C. P. Martin, B. Tadic, and P. J. Moriarty, **Electronic Transport in Cellular Nanoparticle Networks: 2D or not 2D?** *submitted to Nano. Lett.* **(2007)**.

M. O. Blunt, C. P. Martin, M. Ahola-Tuomi, E. Vajour, P. Sharp, P. Nativo, M. Brust, P. J. Moriarty, **Coerced coarsening of nanoparticle assemblies: A mechanical drive towards equilibrium.** *Nature. Nanotech.* in press, **(2007)**.

M. O. Blunt, C. P. Martin, E. Vajour, P. J. Moriarty, **Colloidal nanoparticle corrals [based on the work discussed in Chapter 5].** *In preparation.* **(2007)**.

Acknowledgments

Contents

"The length of this document defends it well against the risk of its being read."

Winston Churchill.

Chapter 1

Introduction

It seems that recently in the field of nanoscience or nanotechnology (depending on your preferred name for the subject), it is almost a necessity to begin any formally written report by mentioning how much room there is at the bottom. The almost ritualistic referencing of Feynman's seminal talk of 1959 [2], however, is probably less a result of a lack of imagination shown by modern scientific authors and more a testament to the intellect of the orator in question. In the few simple words of the title of his talk Feynman seems to have grasped, and in a simple fashion explained, the magnitude of technological possibilities that would be made available by the development of methods for the control of matter over the atomic to micrometric dimensions. I doubt, however, that even Feynman would have believed the scope of the current nanotechnology phenomenon. Heralded simultaneously as the possible saviour and destroyer of modern society, nanotechnology is one of the most intriguing areas of 21st century scientific research.

Giving a concise definition of nanotechnology is a very difficult process. As with most of the names given to new, fashionable areas of scientific study,

nanotechnology encompasses ideas and expertise from a range of disciplines including biology, solid state physics, surface science and quantum mechanics to name but a few. Nanotechnology at its core concerns the manipulation and physical properties of matter over the nanometre size range. Over this size range, matter behaves in radically different ways as compared to its macroscopic form. Effects which are minimal when considered for pieces of matter at larger sizes can have drastic consequences when we start to reduce the size to microns and below. It is by the control of effects that are unique to the nanometer size range that nanotechnology offers the promise of new *designer materials* having optical, magnetic and electronic properties tailored to suit a specific task.

Top-down or bottom-up?

Current manufacturing techniques used in the semiconductor microelectronic industry centre on the use of lithography to produce structures and devices. In these methods a bulk material is taken and a pattern is imposed upon it in some way either by selective exposure to a particular type of radiation or by mechanical pressure with a pre-patterned mask coated with a transferable coating of molecules. This patterning alters some property of the surface allowing other processes such as chemical etching to remove some of the material and leave behind structures which are defined by the original patterning process. Processes such as this, where material is removed from a bulk sample to create smaller structures, are referred to as *top-down* techniques.

The obvious counterpart to this kind of technique is the *bottom-up* approach. In this case the constituent parts (atoms or molecules) are brought together to form the desired structure with no waste material produced. The

initial advantage of this kind of process over the top-down approach appears obvious. However the task of bringing each individual constituent part of a complex nanostructure together individually and placing them in exactly the right place seems a daunting task. This is also coupled with a time constraining factor: for any nano-device to perform a task effectively there will surely need to be a massive number of the devices working in parallel.

At first glance even if the bottom-up manufacturing process takes only a fraction of a second to make one device, to make enough devices will take a prohibitive amount of time. The answer to this problem, as has been the case with many technological problems, can be found by observing how evolution has allowed nature to produce its own functioning nano-devices via *self-assembly* and *self-organisation.*

Self-assembly and self-organisation

Self-assembly and self-organisation are both processes by which ordered structures may be created over a vast range of different length scales. The distinction between self-assembly and self-organisation concerns the equilibrium state of the structure which is formed. Self-assembled structures are in a stable or metastable state of equilibrium, whilst self-organised structures are maintained out of equilibrium by a flow of energy/matter or a gradient in field.

Examples of self-assembly are myriad in nature, from the recombination of DNA strands to the folding of protein molecules into a desired protein macromolecule. The basic principle of self-assembly is that all of the information required to form a structure is contained within the individual constituent parts of that structure and the rules which govern how those constituent parts interact with each other and their environment.

3

Take, for example, a solution of molecules. The Brownian motion of the molecules in solution will cause them to sample a wide range of structural configurations. If, due to the structures of the individual molecules, one configuration is more energetically favourable than the rest, this structure will emerge from an initially random arrangement.

This encoding can come in many different forms, from the obvious information contained within the base pair sequences of a strand of DNA to something as simple as the difference in polarity between the two ends of a surfactant molecule. The possible advantages of self assembly for the nanotechnologist are immense, and span, for example, the ability to quickly produce as many nanostructures as needed, to placing nano-devices on a surface and have them spontaneously form into larger pre-defined hierarchical structures. Due to these possibilities self-assembly has been the subject of a significant amount of research. These studies have ranged in focus from the self assembly of mono-layers of thiol molecules on gold surfaces (SAMs) [3], to the use of DNA functionalisation to force the self-assembly of nanoparticles into larger structures [4].

The important distinction between self-assembled and self-organised structures is that self-assembled structures have reached a state of equilibrium. Returning to the example of molecules in a solution, the structure which emerges will be the one possessing the locally lowest potential energy. This may be a metastable state represented by a local minimum in the free energy or the thermodynamic ground state. The important factor is that the structure is in equilibrium, no flow of energy is required to maintain it.

Self-organisation concerns pattern formation in systems that are maintained out of equilibrium, examples include convection patterns, and reaction-

diffusion systems, such as the Belousov-Zhabotinsky reaction. Self-organisation is very often linked to a phase transition. Imagine a system at a certain temperature where a particular configuration of that system (phase) has the lowest free energy. If we now change the temperature we can drive the system *through a phase transition* to a point where a different configuration of the system has the lowest free energy. The individual molecules/atoms of the system will now be driven to adopt this new configuration. Importantly though, this change in configuration is not instantaneous. Finite timescales are required for the reordering of the system, and these time scales can be *very* long. Therefore, in certain situations a sharp change in a parameter, most often temperature, can cause a system to be effectively frozen at different non-equilibrium stages of this reordering process. Patterns can be formed which, while not representing equilibrium states of the system, do possess a high degree of order. For a detailed review of non-equilibrium pattern formation see Cross and Hohenberg [5].

Nanoparticles

Nanoparticles, or nanocrystals, as the names would suggest, are a small crystalline piece of solid with dimensions in the nanometre size range. These particles can contain anywhere from a few to a few thousand atoms. The small size of the nanoparticles gives them some truly unique properties. Quantum confinement of electrons radically alters the electronic structure of the nanoparticle as compared to the bulk material. This in turn can affect the optical, magnetic and electrical transport properties of the nanoparticle. In addition, the extremely high surface-to-volume ratio of the nanoparticles can dramatically affect their chemical properties.

Nanoparticles can be separated into two main categories: surface grown nanoparticles (perhaps more commonly referred to as quantum dots) and colloidal nanoparticles. The first are only stable on surfaces and can be formed using a variety of techniques such as electron beam lithography and the thermal breakdown of thin films of materials on surfaces. Colloidal nanoparticles, however, are stable when dissolved in a solvent. This stability is achieved by overcoming the nanoparticles' natural tendency to aggregate into much larger particles. This may be achieved by a variety of methods including the use of charged nanoparticles and a polar solvent to create charge stabilised nanoparticles or by the bonding of passivating ligands to the surface of the nanoparticles.

The early 1990s saw the development of a number of important methods for the production of size tunable, mono-disperse colloidal nanoparticles of a number of different materials. One of the most important [6] was used to produce ~2nm Au nanoparticles with an outer covering of thiol molecules. These nanoparticles were shown to be extremely stable both in and out of solution. Indeed, the solvent could be evaporated, leaving the nanoparticles as a dry film for periods of weeks, which could subsequently be re-dissolved to recover the original nanoparticle solution.

Work by Andres *et al* [7] demonstrated that colloidal nanoparticles could self-assemble into ordered close-packed hexagonal arrays when deposited from solution in conditions where the solvent evaporation was slow; i.e. where near-equilibrium conditions were maintained. For solutions of nanoparticles possessing a bimodal size distribution Kiely *et al* reported that for similar near-equilibrium conditions nanoparticles spontaneously formed into bimodal arrays. An example of such an array can be seen in Figure 1.1 (Kiely *et al* [8]).
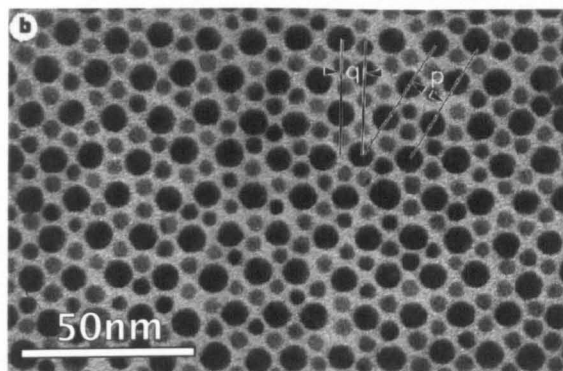
Figure 1.1: Bimodal array of 4.5 and 7.8nm diameter nanoparticles (Kiely *et al* [8]).

The drying of nanoparticle solutions on solid surfaces has proven to be a particularly rich source of pattern formation. This is due in part to the wide range of pattern formation mechanisms which are possible in this system and in part to the nature of the nanoparticle motion in the absence of solvent. The nanoparticles become immobile on substrates in the absence of solvent and this allows the effective *freezing* of self-organised patterns at different points in their evolution.

Patterns ranging from labyrinthine structures attributed to spinodal decomposition [9], to rings and hexagonal structures attributed to the Marangoni effect [10], have all been observed in the drying of nanoparticle solutions. Building on the work of Brus *et. al.* [9], work by Moriarty *et al* [11] demonstrated that nanoparticles deposited under far-from-equilibrium conditions, *i.e.* during a forced evaporation of the solvent, could form a wide array of different pattern morphologies.

One of the most notable recurring patterns was that of the *cellular network*. As illustrated in Figure 1.2, the cellular network is a pattern that is ubiquitous in nature and is seen in fracture patterns in drying mud flats, the patterning on the skin of a giraffe, the foam on a pint of beer, and even the large scale

structure of the universe.
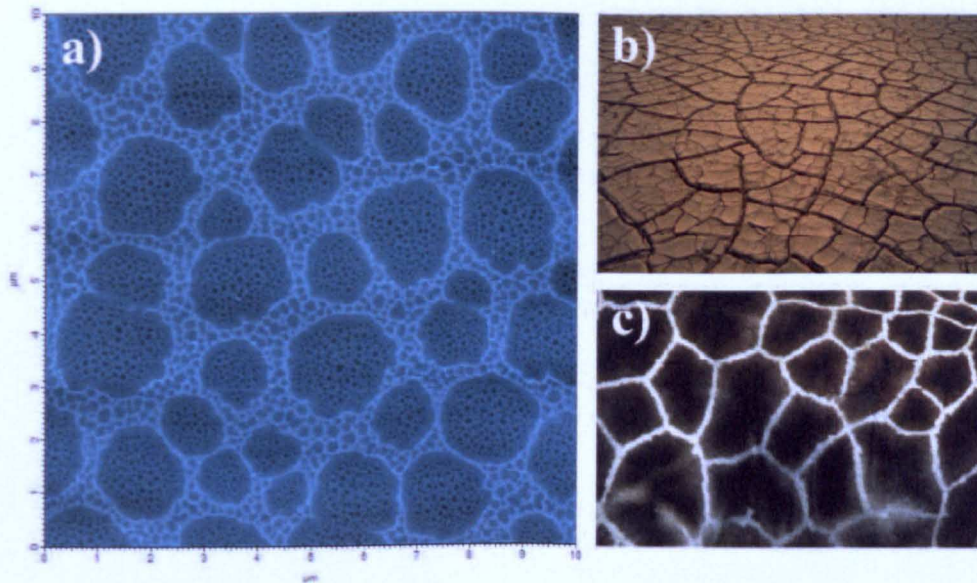
Figure 1.2: Examples of *cellular networks*, **(a)** Bi-layer nanoparticle cellular network, **(b)** fracture patterns of drying mud flats and **(c)** patterns on the skin of a giraffe.

Cellular networks are of particular interest due to the rigorous mathematical treatment and description they have already received from many sources [12]. Using these techniques and associated image analysis methods cellular networks can be classified and compared to each other. Perhaps most intriguingly, these methods allow a value for the geometric entropy associated with a particular network to be calculated.

Thesis outline

This thesis presents a detailed study, (mainly using scanning probe microscopy) of the morphology of self-organised nanoparticle structures formed by the spin coating of nanoparticle solutions onto solid substrates. Investigations are carried out into the various factors that affect the morphology of the structures that are produced and how the morphology of the resulting structures affects

8

their electrical transport properties. Both surface modification and external mechanical driving forces are employed to control the morphology of nanoparticle assemblies over micron and sub-micron length scales. At various points in this thesis (chapter four and chapter five) Monte Carlo simulations of the drying of thin nanoparticle/solvent films are used to help gain physical insight to the processes underlying nanoparticle pattern formation. All such simulations were written and carried out by C. P. Martin at the University of Nottingham [1].

Chapter two: An overview of the current scientific knowledge concerning both theoretical and experimental studies of the structure and properties of colloidal nanoparticles will be given, along with a discussion of intermolecular forces and phase transitions.

Chapter three: This chapter will centre on a description of the main experimental techniques employed in this study, namely atomic force microscopy (AFM) and some of its derivative techniques.

Chapter four: A systematic study of the factors affecting the morphology of nanoparticle networks produced by the spin casting process is carried out. Experiments studying the effect of variation in nanoparticle solution concentration, variation in the substrate surface chemistry, and the use of different solvents are all discussed.

Chapter five: Scanning probe lithography is used to selectively pattern hydrogen terminated surfaces with areas of silicon dioxide, with line widths as small as 50nm. The resulting closely spaced areas are shown to possess rad-

ically different surface chemistries and are used to tune the morphology of sub-monolayer nanoparticle assemblies.

Chapter six: Mechanical coarsening of nanoparticle assemblies is induced by repeated scanning with an AFM probe. The scaling of nanoparticle aggregate size with the number of scans and the functional form of the aggregate size distribution are linked to the novel nature of the mechanically driven coarsening process.

Chapter seven: The electrical conduction properties of two-dimensional nanoparticle arrays of varying morphologies and thiol capping ligand lengths are studied. D.C. electrical measurements taken over a range of lateral array sizes and temperatures from 4.5K to 80K were collected. Scaling properties of the electrical conduction are related to the topology of the nanoparticle arrays. Electrostatic force microscopy (EFM) is also used to observe charge transport in a nanoparticle network at room temperature.

Chapter eight: Discussions of all the main results of the thesis will be given along with suggestions for the future directions of the research.

Chapter 2

An overview of nanoparticle science and phase transitions

An overview of the current scientific knowledge concerning both theoretical and experimental studies of the structure and properties of colloidal nanoparticles will be given, along with a discussion of intermolecular forces and phase transitions.

2.1 Introduction

Nanoparticles have been studied and used (sometimes unwittingly) in different forms for hundreds, if not thousands, of years. From the ancient Egyptians to Michael Faraday [13], the properties of small particulates of matter dispersed in solution, also know as *colloids*, have been of great interest. In this chapter the structural properties of colloidal nanoparticles will be discussed. Their stability in solution and the dependence of their physical properties on their size are amongst the key topics. A particularly important synthesis route by which colloidal nanoparticles may be fabricated will be detailed, along with a

discussion of the size-dependent electrical properties of individual nanoparticles.

Due to the importance of inter-particle forces when considering pattern formation in nanoparticle assemblies, a brief discussion of the theoretical basis for these interactions will be provided, followed by an overview of the theory of phase transitions and how it relates to pattern formation.

2.2 The structure of nanoparticles

Nanoparticles are crystalline pieces of matter with dimensions in the nanometre size range. This reduction in size from the bulk material to dimensions in the range $\sim 1nm$ to $\sim 100nm$, causes drastic changes to many of the fundamental physical properties of the material used to form the nanoparticle. These changes can come about due to a number of reasons ranging from the extremely small capacitance of such particles to quantum effects caused by the confinement of electrons within the dimensions of the nanoparticle.

The extremely small size nanoparticles means that they have very high surface to volume ratios. A nanoparticle will therefore contain a far higher proportion of surface atoms than a bulk specimen of the same material. For example, a typical cluster of 1000 atoms will have approximately 25% of these atoms present at the surface of the cluster. For this reason, unterminated nanoparticles possess high numbers of unfilled dangling bonds at their surfaces. This in turn gives them extremely high surface free energies and makes free nanoparticles extremely reactive. This high reactivity can be responsible for uncontrolled and irreversible aggregation of nanoparticles, or oxidation of their surfaces. Neither of these effects are particularly desirable when the intriguing properties of nanoparticles brought about by their small size and chemical

specificity are of interest.

To overcome these issues the high surface free energy of the nanoparticle must be reduced. The most obvious means of doing this is to reduce the number of dangling bonds present at the surface. In bulk materials high surface free energies can be lowered by a reorganisation of the surface layer of atoms into a different crystal structure from that of the bulk. By adopting a crystal structure which presents a lower number of dangling bonds at the surface the surface free energy is thus reduced. This process is know as *reconstruction*.

A similar process may occur in nanoparticle formation, where a different crystalline structure from that normally found in the bulk material is adopted within the nanoparticle. This process alone cannot, however, completely remove the problem of high surface free energies. There are effective ways of further lowering the surface free energy of nanoparticles, and two of the most prevalent methods employed are detailed in the following section.

2.2.1   Charge-stabilised nanoparticles

Charge stabilisation methods for colloidal nanoparticles involve the creation of charged nanoparticles, and the use of oppositely charged co-ordination molecules/ions to form a terminating layer around the nanoparticle. When present in an ionic solution the charged nanoparticles will attract a surrounding cloud of oppositely charged ions. This cloud of ions will provide repulsion between the nanoparticles and overcome their natural tendency to coalesce.

An example of this is the method developed by Frens *et al* [14] for the synthesis of citrate/chloride stabilised gold nanoparticles. In this method an aqueous solution of hydrogen tetrachloroaurate is reduced via the addition of sodium citrate. It is believed [15] that the charge state of the nanoparticles is

that of a Au^0 core surrounded by an Au^1 shell. The positively charged outer shell of the nanoparticle is coordinated with a shell of negatively charged citrate and chloride anions, thus forming a stable nanoparticle solution.

However, charge stabilisation techniques can also place limitations on the experimental usefulness of the nanoparticles. These may range from the restriction to the use of ionic or markedly polar solvents, to the difficulties involved in forming close packed arrays of such nanoparticles when deposited onto surfaces. As noted by Andres *et al.* [7], the repulsive forces between like-charged nanoparticles make it extremely unlikely that they will form close packed structures when deposited onto surfaces. To overcome these obstacles a charge neutral surface passivation technique is preferred.

2.2.2 Ligand-stabilised nanoparticles

Nanoparticles may also be stabilised via the direct covalent bonding of molecules to the nanoparticle surface. Molecules used to perform this kind of task are often referred to as *ligands*. As opposed to charge stabilisation methods, where Coulombic repulsion is used to keep the nanoparticles apart, the ligand stabilisation method lowers both the surface free energy of the nanoparticle *and* introduces a steric hinderance to the coalescence of the nanoparticles. Direct covalent bonding of molecules to the surface of the nanoparticle occupies many of the dangling bonds, and thus lowers the surface free energy of the nanoparticle. The simple physical presence of a shell of molecules around the nanoparticles surface also hinders other nanoparticles approaching too closely, thus preventing coalescence.

One of the most scientifically important nanoparticle-ligand systems to have been developed over the last few decades is that of thiol-terminated

gold/silver particles. The basis for the development of this system came from work on *self assembled mono-layers* (SAMs) of alkane thiol and other organo-sulphur molecules on gold surfaces [16,17]. Alkane thiol molecules consisting of a hydrocarbon chain with a sulphur atom at the end have been shown to form a wide array of ordered assemblies on single crystal gold surfaces. The strong affinity of the sulphur atom for the gold surface makes thiol molecules the perfect stabilisation ligand for gold nanoparticles. The thiol termination produces nanoparticles that are extremely chemically stable, both in and out of solution, and are also soluble in a wide range of organic solvents.

2.2.3 Colloidal nanoparticle synthesis

The nanoparticle synthesis method which is used to produce the majority of the nanoparticle solutions used in the experiments described in this work is based on that developed by Brust *et al.* in 1994 [6] and, for the work described in this thesis, was carried out mainly in Nottingham. This is a simple wet chemical preparative technique involving the reduction of a gold containing salt in the presence of surface terminating thiol molecules.

The method is described as being a *"two phase, liquid-liquid"* process. The two liquid phases mentioned here refer to organic/inorganic or polar/non-polar phases. In this case ionic solutions containing gold are transferred from an aqueous (polar) solution to an organic (non-polar) solution by the use of a phase transfer agent. The phase transfer agent used is a surfactant molecule. Surfactants are termed *amphiphilic*, meaning they contain a hydrophilic part, generally known as the head, and a hydrophobic part known as the tail. In the method developed by Brust *et. al.* [6], the surfactant molecule used is tetraoctylammonium bromide ((C_8H_{17})$_4$NBr) which will subsequently

be referred to here as TOAB for simplicity (see Figure 2.1 for a schematic representation of this molecule).

○ = Carbon

N⁺ = Nitrogen

Br⁻ = Bromine

Covalent bond

Ionic Bond
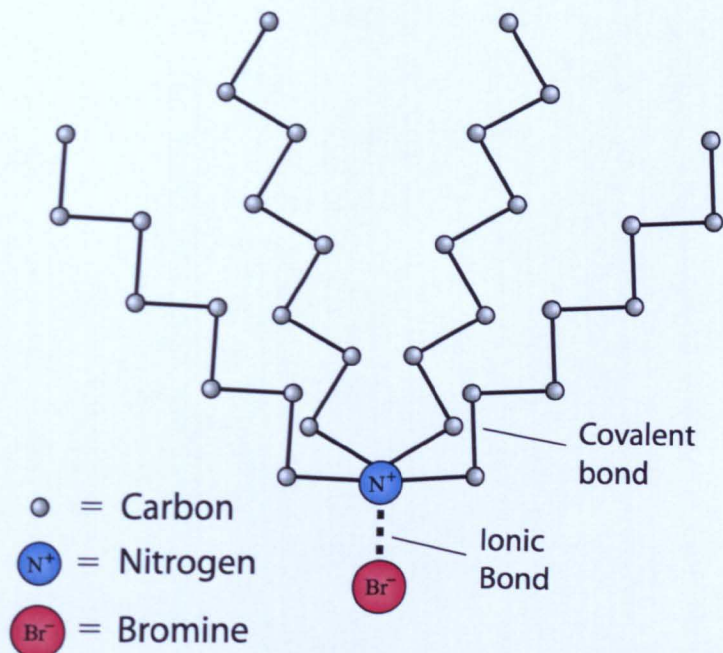
Figure 2.1: Schematic representation of tetraoctylammonium bromide (TOAB) molecule.

The molecule consists of four aliphatic carbon chains, each consisting of eight carbon atoms connected to a central nitrogen atom. Consequently, the central nitrogen atom is positively charged and forms an ionic bond with a negatively charged bromide ion. The ionic complex consisting of the charged nitrogen and bromine atoms provides one end of the TOAB molecule with a highly polar nature whilst the aliphatic carbon chains at the opposite end of the molecule are non-polar. This disparity in the polar nature of the two ends of the molecule leads to the molecule spontaneously forming a range of self assembled structures when dissolved in certain solvents. The type of structure formed is dependent on both the nature of the solvent (polar/non-polar) and the concentration of TOAB molecules. The structure of particular interest in

this case is that of a *reverse micelle*, formed when the molecule is dissolved in appropriate concentrations in organic solvents.

Figure 2.2 shows a schematic representation of a reverse micelle structure. For the sake of simplicity on the diagram the four carbon chains present on each TOAB molecule are represented by a single chain on each molecule, referred to as the tail. The reverse micelle is a spherical structure in which the polar head groups of the TOAB molecule are oriented inwards and the non-polar tails outwards. This arrangement lowers the free energy of the structure by minimising contact between the polar head groups and the non-polar solvent, and maximising it for the non-polar tail groups.

TOAB surfactant molecule.

} Tail (non-polar).

} Head (polar).
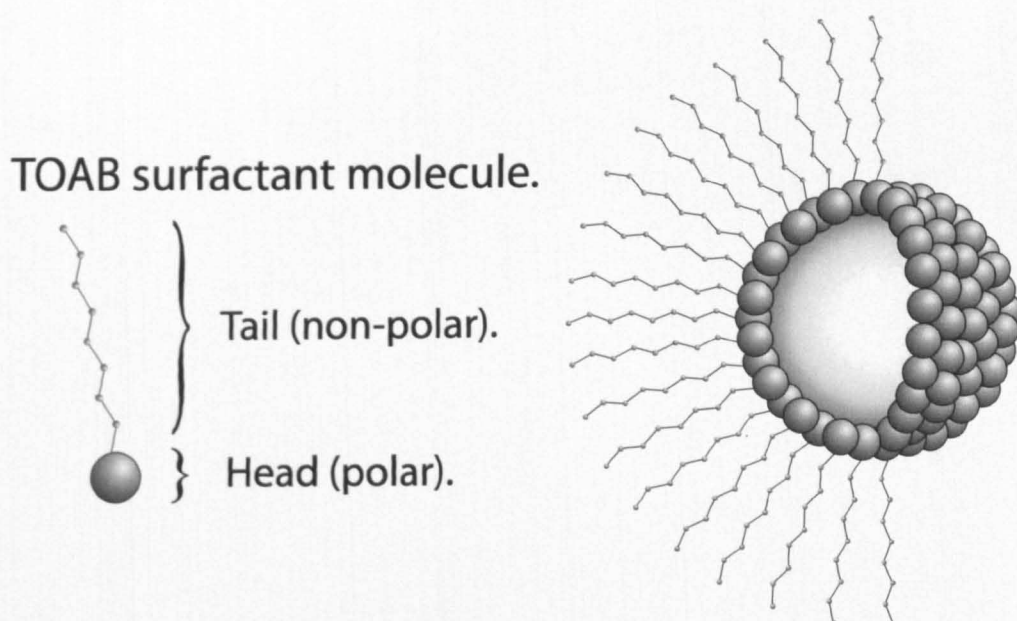
Figure 2.2: Schematic representation of a reverse micelle structure formed by TOAB surfactant molecules when they are dissolved in toluene.

It is this reverse micelle structure that provides the *two phase liquid-liquid* nature of the reaction, referred to in the title of Brust's work [6]. The two phases are the polar and non-polar environments present on the inside and outside of the reverse micelle. Along with a solution of TOAB in toluene,

a second solution consisting of hydrogen tetrecholoroaurate ($HAuCl_4.xH_2O$) dissolved in water is also prepared. This produces an ionic solution containing $AuCl_4^-$ ions. These two solutions are then mixed together.

The $AuCl_4^-$ ions would normally be extremely insoluble in an organic solvent such as toluene. The presence of the reverse micelle structures, however, allows the $AuCl_4^-$ ions to dissolve in the toluene solution by providing a polar environment within the toluene solution, namely that present at the center of the reverse micelles. The aqueous and organic parts of the mixture are then separated, leaving a toluene solution with reverse micelles that contain $AuCl_4^-$ ions. To this solution thiol molecules are added, followed by a slow, drop-wise addition of an aqueous solution of sodium borohydride ($NaBH_4$).

The sodium borohydride acts as an electron source and reduces the Au^{3+} species to $Au(0)$. Upon creation of the $Au(0)$ species aggregation into nanoparticles begins to occur. This aggregation process, is however, controlled by the presence of the thiol molecules. As the nanoparticles grow their surfaces are terminated by a layer of thiol molecules thereby arresting the growth of the nanoparticles at a certain size. The final size of the nanoparticles produced can be roughly controlled by alteration of the ratio of thiol to gold in the reaction mixture [18].

The mixture then undergoes a number of cleaning procedures to remove any leftover TOAB and excess thiol molecules. These cleaning steps involve the addition of an excess of ethanol to the toluene nanoparticle solution, and then placing this mixture in a low temperature environment ($\sim$-18°C). Excess thiol and TOAB molecules remain soluble in an ethanol/toluene mixture while the nanoparticles fall out of solution and aggregate into a dark precipitate; the low temperature is not a required step, however it greatly speeds this process. This

mixture is then filtered and thiol and TOAB contaminants are washed through the filter while the nanoparticle precipitate is trapped. The nanoparticles may then be re-dissolved with toluene, or any other desired solvent, to give clean nanoparticle solutions.

The nanoparticles produced by this method have been shown to be highly stable both in and out of solution, even to the point where they can be precipitated and redissolved several times without any significant degradation. The synthesis procedure is also extremely versatile. By a simple substitution of hydrogen tetrachloroaurate with silver nitrate ($AgNO_3$) silver nanoparticles may be produced instead of gold.

The reaction is also very robust to variation of the size and type of thiol molecule used to terminate the nanoparticles. Molecules used as capping ligands range from alkanethiolates with varying chain lengths (C_3-C_{24}) [19] to more complex molecules such as diakyl sulfides [20], and even non-polar ligands such as arenethiolate [21]. The only prerequisite for the molecule used as a capping ligand is that it has an unhindered sulphur atom that can bond to the noble metal surface. The synthesis method developed by Brust *et al* [6] has been used as the basis for developing techniques to synthesise a wide range of different types of nanoparticles, ranging from semiconductor to magnetic nanoparticles.

2.3 Electronic properties of single nanoparticles

In bulk crystalline materials, electrons occupy what are essentially continuous energy bands. The separation and degree to which these bands are occupied are the determining factors for many of the fundamental optical and electrical properties of the material. Occupying the opposite end of the spectrum we

have electrons which are present in atomic and molecular systems. Within such systems electrons are confined to distinct energy levels. Once again it is the occupancy and separation of these levels that defines the physical properties of the system. The nanoparticle represents a middle ground between these two extremes, with neither the sharp well defined energy bands of the atomic system or the continuous energy bands of the bulk material. Combined with properties such as their extremely small capacitance, this makes nanoparticles an attractive medium for the study of electronic transport at the nanoscale.

2.3.1 Size effects

Size effects are simply alterations of the physical properties of a material that occur due to a reduction in size of a specimen of that material. At this point a distinction should be made between *size effects* and *quantum size effects*. A *size effect* is a change in the material's physical properties due to some classical parameter which is size dependent. An example which is of particular relevance to the current study is the reduction in capacitance which accompanies a reduction in size for spherical particles, this will be discussed in more detail shortly.

A *quantum size effect* is a change in the material's properties due solely to the quantum confinement of electrons as the size of the material specimen is reduced. The most obvious quantum size effect, mentioned briefly above, is the alteration of the material's bulk electronic band structure. In essence when we reduce the size of a material we are reducing its dimensionality. By this we mean we are reducing the number of dimensions that the electrons of the material are free to move in.

2.3.2 Band structure

To see how the density of electronic states in a metal is altered by a reduction in dimensionality we shall use the *free electron model* [22]. In this model all the valence electrons of the metal atom are assumed to be completely free of that atom: the electrons behave as a *free electron gas*.

The removal of the valence electrons from the atom cores leaves behind a lattice of positively charged ions. The potential produced by these ions is then assumed to be constant throughout the metal. These assumptions remove all of the detail in the band structure introduced by the periodicity of the crystal structure. However, this model will suffice to show qualitatively how reduced dimensionality affects the electronic band structure.

Take a three dimensional cube of the metal in its bulk state, with sides of size L which has its faces perpendicular to the x, y and z axes. To find the allowed energy levels of electrons confined within this cube, we solve the (time-independent) Schrodinger equation:

$$-\frac{\hbar^2}{2m} \nabla^2 \psi = E\psi \qquad (2.1)$$

If we take the uniform potential within the cube to be zero and assume periodic boundary conditions such that,

$$\psi(x + L, y + L, z + L) = \psi(x, y, z) \qquad (2.2)$$

then the solutions of Schrodinger's equation are travelling plane waves,

$$\psi(x, y, z) = \frac{1}{V^{\frac{1}{2}}} e^{i(k_x x + k_y y + k_z z)} \qquad (2.3)$$

where $V = L^3$ is the volume of the cube and the factor $1/V^{1/2}$ ensures that the wavefunction is normalised. To satisfy the periodic boundary conditions stated in equation 2.2 the wavevector components are limited to the values of

$$k_x = \frac{2\pi p}{L}, \qquad k_y = \frac{2\pi q}{L}, \qquad k_z = \frac{2\pi r}{L} \qquad (2.4)$$

with p, q and r taking any positive or negative integer value or zero. This solution to the Schrodinger equation corresponds to an energy of

$$E = \frac{\hbar^2 k^2}{2m} = \frac{\hbar^2}{2m}(k_x^2 + k_y^2 + k_z^2) \qquad (2.5)$$

We use the equation for the number of allowed k states in a spherical shell of k-space of radius k and thickness dk, centered on the origin [22],

$$g(k)dk = \frac{Vk^2}{2\pi^2}dk, \qquad (2.6)$$

where $g(k)$ is the density of states per unit magnitude of k. This result can be used to determine the number of allowed electronic states per unit energy range $g(E)$, also referred to as the *density of states*. The fact that electrons have a spin value of $\frac{1}{2}$ means that each k state represents two possible electron states of the same energy. Therefore the number of electronic states in a spherical shell between k and $k + dk$, which correspond to energies between E and $E + dE$, may be written as

$$g(E)dE = 2g(k)dk, \qquad or \qquad g(E) = 2g(k)\frac{dk}{dE}. \qquad (2.7)$$

Combining equation 2.7 with equations 2.5 and 2.6 and rearranging gives the electronic density of states as

$$g(E) = \frac{V}{2\pi^2\hbar^3}(2m)^{\frac{3}{2}}E^{\frac{1}{2}}. \tag{2.8}$$

The electronic density of states shows a smooth $\sqrt{E}$ dependence on the energy. This is shown in Figure 2.3 **(a)**. The situation we have just studied is three-dimensional: the electrons are free to move in all three dimensions (x, y, and z).

Now let us consider a situation where one of the dimensions of our system has been drastically reduced. Instead of a cube of side L, our system now consists of a thin square film of size L in the x and y directions, and d in the z direction, (where $d \ll L$), see Figure 2.3 **(b)**. Adopting the same approach as used for the three dimensional situation, we again need to solve the time independent Schrodinger equation for our system. As before, periodic boundary conditions will be used for the x and y directions, (equation 2.2). In this case, however, the z dimension of our system has been greatly reduced, constraining the electrons to the small length scale represented by d. To include this change in our solution the periodic boundary condition are replaced in the z direction by infinite potential barriers at $z=0$ and $z=d$. The presence of these barriers means that the wavefunction is forced to zero at $z=0$ and $z=d$. In effect, the electrons are free to move in the x and y directions and we have a one dimensional infinite square potential well in the z direction. In this case the solution to the time independent Schrodinger equation is

$$\psi(x, y, z) = e^{ik_x x}e^{ik_y y}\sin(k_z z) \tag{2.9}$$

This solution is now plane travelling waves in the x and y directions, and standing waves in the z direction. To satisfy the altered boundary conditions
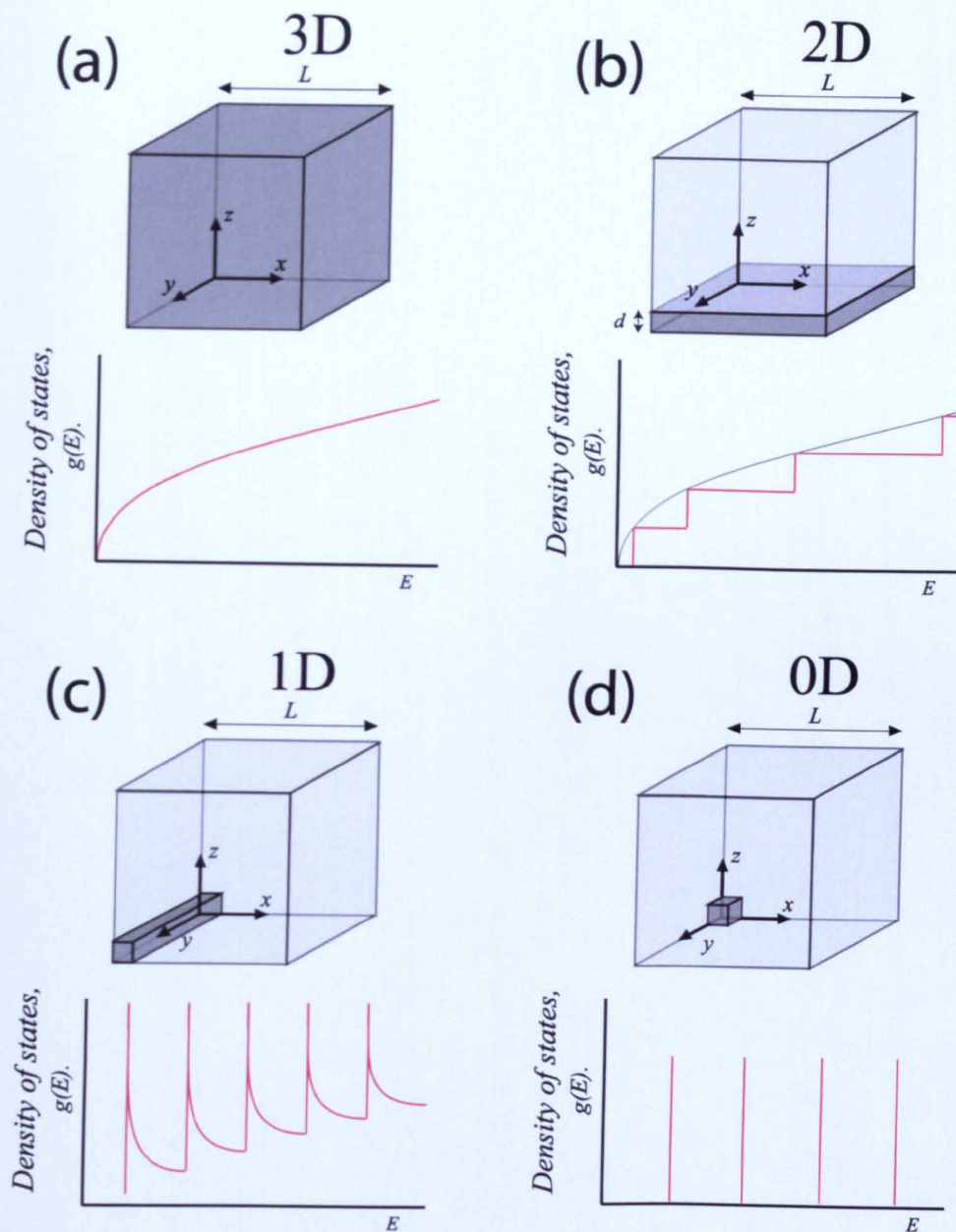
Figure 2.3: Schematic representations of the reduction in dimensionality of a material system from 3D to 0D (part **(a)** to **(d)**) and the consequent effect on the material's band structure. **(a)** In a 3D system the density of states shows a smooth $\sqrt{E}$ dependence. **(b)** In a quasi 2D system, such as a quantum well structure, the density of states appears as a step like function of E. **(c)** In a quasi 1D system, such as a quantum wire structure, the density of states has a $1/\sqrt{E}$ form within each band. **(d)** In a 0D system, such as a quantum dot or nanoparticle, the density of states consist of discrete delta like functions.

the allowed values of k_x, k_y and k_z are now

$$k_x = \frac{2\pi p}{L}, \qquad k_y = \frac{2\pi q}{L}, \qquad k_z = \frac{n\pi}{d}. \qquad (2.10)$$

The allowed components of the wave vector are the same for k_x and k_y as in the 3D system. However in the z direction the wavefunction corresponds to the stationary states of a 1D infinite square potential well. The k_z values are those that fit an integral number of half wavelengths into the square well. Following the same method as before we obtain the energy eigenvalues as:

$$E = \frac{\hbar^2}{2m_e}(k_x^2 + k_y^2 + k_z^2) = \frac{\hbar^2}{2m_e L^2}(p^2 + q^2) + \frac{n^2 h^2}{8 m_e d^2}. \qquad (2.11)$$

The final term in this equation equates to the energy levels of an infinite square potential well, while the term containing (p^2+q^2) is the energy associated with motion in the xy plane. The implications of this energy level scheme can be seen in Figure 2.3 **(b)**.

The lowest energy state with $n{=}2$ (that with $p = q = 0$) is $3h^2/8m_e d^2$ higher in energy than the lowest $n{=}1$ state. Thus for small enough confinement lengths (d) the thermal energy at readily obtainable experimental temperatures $(k_B T)$ will be less than this difference. Therefore all of the electrons will be effectively trapped in the $n{=}1$ state. This freezes motion in the z direction; the electrons will behave as free particles in a 2D space.

Following a similar method to that used for the 3D system the density of electronic states for a quasi 2D system, for a fixed value of n, is given by

$$g(E) = \frac{m_e}{\pi \hbar^2}. \qquad (2.12)$$

So for a fixed value of n the density of electronic states is independent of

the energy. Of course, as the energy is increased, more of the stationary states in the infinite potential well that makes up the z direction can be occupied. The leads to a step like dependence of the electronic density of states, as seen in Figure 2.3 **(b)**.

Similar methodologies can be applied to 1D and 0D systems, leading to the density of states relationships shown in Figure 2.3 **(c)** and **(d)**. Thus for a true 0D system we have electrons confined in all three spatial dimensions, i.e. the *particle in a box* problem in quantum mechanics. The electronic energy levels produced by such confinement are discrete, delta function-like spikes. It is these discrete electronic energy levels produced by 0D systems, such as nanoparticles, that has led them to be dubbed by many as *artificial atoms* [23,24]. However, unlike atoms, where the energy level spacing is strictly controlled by the numbers of protons and neutrons in the nucleus, the electronic energy levels of a nanoparticle are tuneable by alteration of the dimensions of the nanoparticle.

2.3.3 Single electron charging

Along with the alteration of a nanoparticle's band structure due to quantum size effects, the electronic structure is also complicated by the extremely small capacitance of the nanoparticle. Under certain conditions this classical size effect can give rise to a process known as *single electron charging*. The extremely small capacitance of nanoparticles can lead to an appreciable charging energy (E_c) per electron. For small enough nanoparticles this charging energy can become comparable to thermal energies at readily obtainable experimental temperatures.

In a bulk specimen of a conductive material, attaching source and drain

electrodes to the material and applying a potential across the specimen causes the motion of vast numbers of delocalised valence electrons. The massive numbers of electrons involved in the charge flow means that even though there is a quantisation of charge for the individual electrons, the charge flow is essentially continuous and obeys Ohm's law (see Figure 2.4 (a)).

In a 0D system, such as a nanoparticle, where the electrons are localised on the nanoparticle by the presence of tunnel barriers between the nanoparticle and the electrodes, charge flow can be controlled at the single electron level. These structures have been described as 'electron turnstiles' for this reason. A certain voltage between the electrodes must be exceeded (i.e. above the nanoparticle's charging energy) before an electron can tunnel from the electrode onto the nanoparticle, see Figure 2.4 (b). It is this controlled transfer of electrons as discrete entities onto and off the nanoparticle that is known as *single electron charging*.

Extending the analogy introduced earlier of nanoparticles as artificial atoms, the charging energy is analogous to the ionisation potential of an atom. Typical ionisation potentials for atoms are in the range of a few electron volts, (the first two ionisation potentials for gold are 9.225eV and 20.521eV). This means that to study the electronic energy levels of atoms optical and other electromagnetic spectroscopic methods are usually employed. The much lower values obtained experimentally for the charging energies of metallic nanoparticles, (2.1nm Pt nanoparticles, $E_c = 50\text{meV-}500\text{meV}$ [25]) means that the electronic energy level structure of the nanoparticle may be probed by studying its electronic transport properties.

Consider the system depicted in Figure 2.5; a ligand passivated nanoparticle on a conducting substrate with an STM tip placed directly above it. This

(a)

(b)
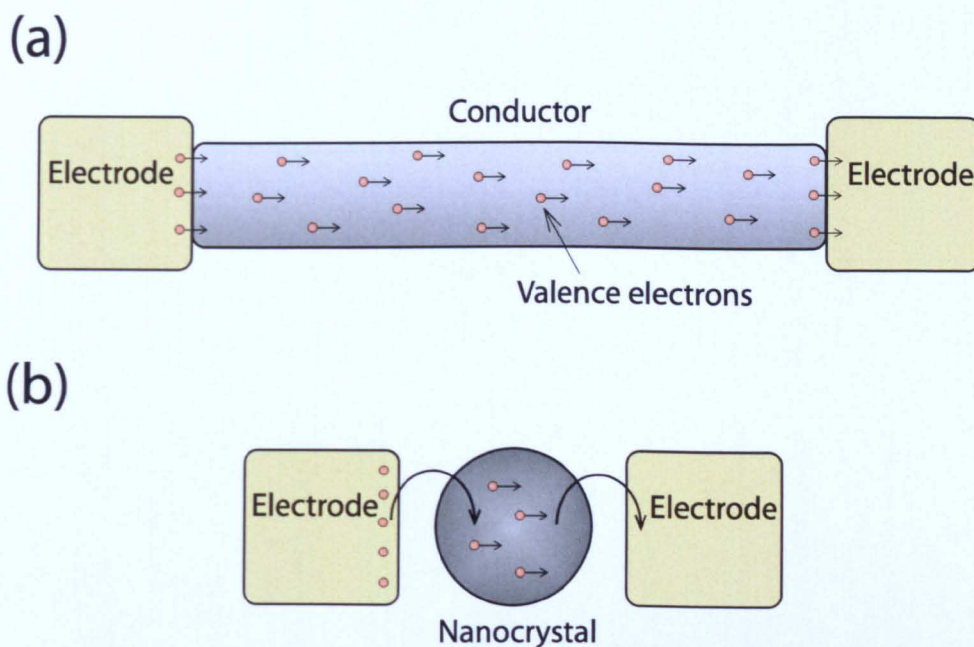
Figure 2.4: Representation of charge flow in a bulk specimen of a conductor, and a nanoparticle. **(a)** In a bulk specimen of a conductor between electrodes an applied potential causes the migration of the conductor's delocalised valence electrons. The charge flow is essentially continuous due to averaging over the vast numbers of electrons involved. **(b)** In a system composed of a sufficiently small nanoparticle separated from electrodes by tunnel barriers, however, the electrons move on and off the nanoparticle as discrete entities.

system is analogous to the electrode-nanoparticle-electrode system depicted in Figure 2.4 **(a)**, with the STM tip and the conducting substrate representing the electrodes. The ligands act as tunnel barriers separating the electrodes from the nanoparticle.

If we assume that the tunnel barriers are high enough such that there is no overlap between the wavefunctions of electrons on the electrodes and electrons on the nanoparticle, *i.e.* the quantum coupling between the electrodes and the nanoparticle is minimal, then the number of electrons on the nanoparticle is an integer value N; thus, the charge on the nanoparticle is Ne. Now let us allow an electron to tunnel onto the nanoparticle.

The charge on the nanoparticle has risen by the quantised amount e. The
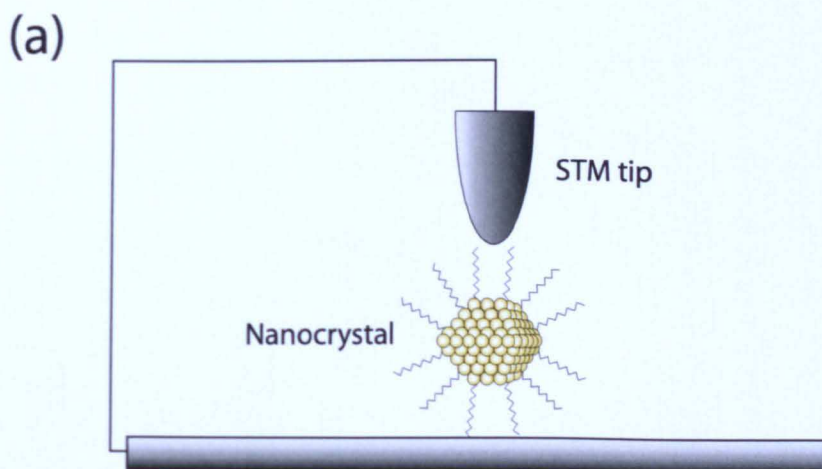
Figure 2.5: Schematic representation of an electrode-nanoparticle-electrode system: a ligand passivated nanoparticle on a conducting substrate with an STM tip in close proximity. The STM tip is the source, the conducting substrate the drain, and the passivating ligands provide tunnel barriers between the nanoparticle and the electrodes.

change in the nanoparticle's charge changes its energy: the electrostatic potential of the nanoparticle has risen. This rise in electrostatic potential is equal to the charging energy. The charging energy may be expressed by combining the equations for the energy of a capacitor $E = (1/2)CV^2$ and the relation between capacitance, charge, and voltage $Q = CV$, where the charge is equal to e. In this particular case the capacitance will be that of the collective tip-nanoparticle-substrate system rather than just the capacitance of the nanoparticle.

$$E_c = \frac{1}{2}\frac{Q}{V}V^2 = \frac{e^2}{2C}. \tag{2.13}$$

The rise in the nanoparticle's electrostatic potential makes it subsequently harder for more electrons to tunnel onto the nanoparticle, and the charging energy must be exceeded again before this can happen. To truly observe single electron charging, the charging energy (E_c) must be substantially greater than

the thermal energy of the system $(k_B T)$. If this requirement is not met then electrons will be thermally excited onto and off the nanoparticle irrespective of the potential across it.

Classically, the capacitance of a spherical object is given by the equation

$$C = 4\pi\epsilon_r\epsilon_0 R, \qquad (2.14)$$

where ϵ_r is the dielectric constant of the material surrounding the nanoparticle and R is its radius. If we take a value of $\epsilon_r=3$ (calculated for a thiol self assembled monolayer on gold [26]), we find that the charging energy becomes equal to the thermal energy at room temperature $(k_B T \sim 0.03\text{eV})$ for nanoparticle radii of $R\sim16$nm. Of course, to ensure that single electron charging takes place we would require the radius to be lower still so that the charging energy is well above the thermal energy at room temperature. This criterion is easily met by colloidal gold nanoparticles, which can have radii as small as 0.5nm.

Another necessary criterion for single electron charging to take place in nanoparticle systems is that the electrons are *localised* to the nanoparticle. The tunnel barriers need to be high enough such that the electrons are either located on the source, on the drain, or on the nanoparticle. The quantum fluctuations in the number N of electrons on the nanoparticle needs to be $\ll 1$ over the time scale of the measurement. It has been shown that this criterion is met for tunnel resistances much greater than the resistance quantum h/e^2 = 25.813kΩ [27]. If these two criteria are fulfilled then we have the possibility of single electron charging taking place.

Returning to the system depicted in Figure 2.5, we have essentially a nanoparticle between two electrodes (a source and a drain). From the discussion so far we can see that, with a finite value for the charging energy, if we

increase the potential across the nanoparticle from zero there will be a range of voltages around zero for which no conduction will occur: this is known as *Coulomb blockade*. As we increase the voltage across the nanoparticle further the level of current flowing goes up in a set of discrete steps known as a *Coulomb staircase*. To understand what is happening as electrons flow through the nanoparticle we need to examine the system in terms of a schematic representation of the energy level landscape of the source, drain, and nanoparticle.

Figure 2.6 **(a)** shows a nanoparticle in the Coulomb blockade regime. The source and drain have electrons occupying levels up to their Fermi levels (E_f). The nanoparticle has N electrons filling its energy levels up to μ_N, the next available energy level is one charging energy higher than this at μ_{N+1}. The Fermi level of the source is below the first empty level available in the nanoparticle; thus no charge flows through the nanoparticle.

If the potential across the nanoparticle is raised to a value which puts the Fermi level of the source above the energy level required to have *N+1* electrons on the nanoparticle an electron can tunnel onto the nanoparticle occupying the μ_{N+1} energy level, Figure 2.6 **(b)**. However, once occupied the μ_{N+1} energy level is now above the Fermi level off the drain contact, and thus the electron can tunnel from the nanoparticle to the drain. The process repeats itself and we have a fixed level of current flowing through the nanoparticle.

Figure 2.6 **(c)** is an idealised *I(V)* relationship for such a nanoparticle circuit, showing Coulomb blockade with zero conductance around zero potential across the nanoparticle. The current increases in a stepwise fashion (Coulomb staircase) with progressively larger potentials as more energy levels in the nanoparticle become available for electrons to tunnel into.

The *I(V)* relationship shown in Figure 2.6 **(c)** is an idealised relationship

(a)

Empty states.

E_c

E_f

$\mu(N+1)$

$\mu(N)$

E_f

Source

Drain

Filled states.

(b)

E_f

E_f

Source

Drain

(c)

Current (I).

Coulomb staircase.

Voltage (V).
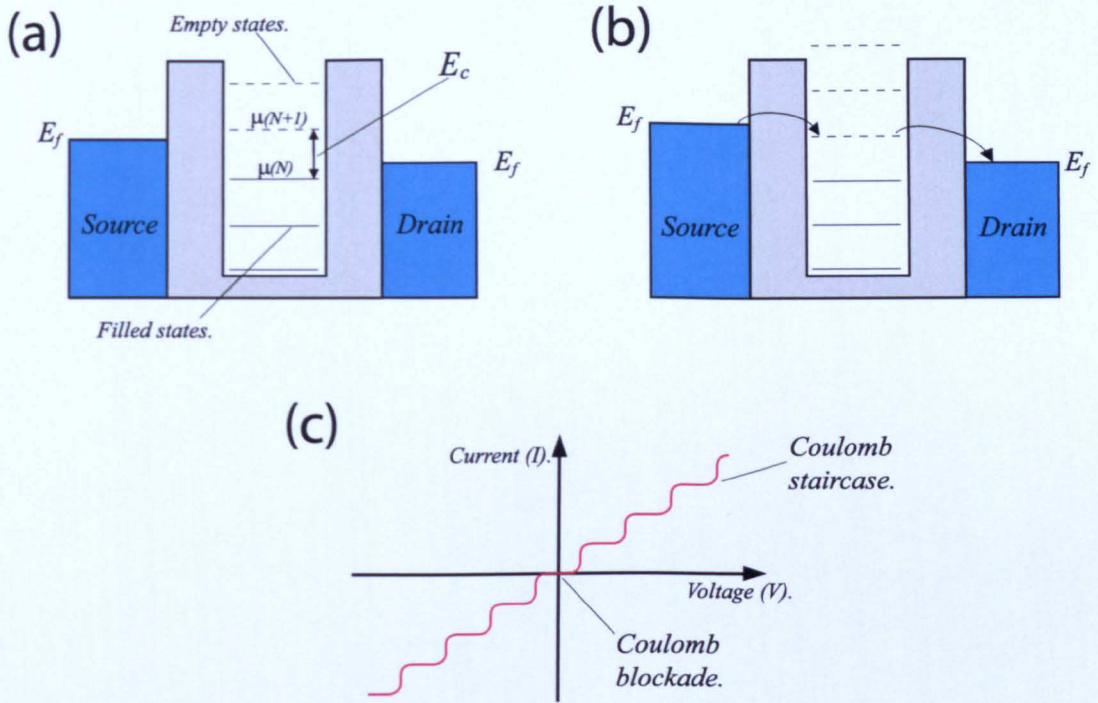
Coulomb blockade.

Figure 2.6: **(a)** Shows an energy level diagram of a nanoparticle in the Coulomb blockade regime. The source contact is occupied by electrons up to its Fermi level. The nanoparticle has N electrons occupying energy levels up to μ_N. The energy levels of the nanoparticle are separated in energy by the charging energy of the nanoparticle (E_c). The Fermi level of the source is not above that of the first unoccupied level on the nanoparticle (μ_{N+1}). Therefore no electrons can flow onto the nanoparticle. **(b)** The potential V is raised such that the Fermi level of the source is raised above the first unoccupied level of the nanoparticle. An electron may now tunnel from the source onto the nanoparticle occupying the μ_{N+1} energy level. However, the μ_{N+1} energy level is now above the Fermi level of the drain contact so the electron now tunnels from the nanoparticle to the drain. The process repeats itself and a constant current flows through the nanoparticle. **(c)** Shows a typical $I(V)$ relationship for such a circuit, showing Coulomb blockade and the Coulomb staircase effect which occurs as more energy levels in the nanoparticle become available for electrons to tunnel into.

only taking into account the effects of the nanoparticle's charging energy. Experimental measurements on similar nanoparticle arrangements have produced *I(V)* curves where the step heights and widths do not remain constant, and additional structure to that expected from simple single electron charging effects is seen [28, 29]. These differences are attributed to the discrete energy levels of the nanoparticle caused by quantum confinement and asymmetries in the structure of the nanoparticle and the height of the tunnel barriers. Random offset charges in the substrate may also play a role by shifting the internal energy levels of the nanoparticle.

2.4 Intermolecular forces

In the following section the physical interpretation of intermolecular forces will be discussed along with various methods that have been developed to quantify them on both microscopic and macroscopic scales. Intermolecular forces are of particular importance to this study in that they play a pivotal role in defining many of the patterns formed in nanoparticle assemblies but they are also the basis for the main experimental tool used in this work, the atomic force microscope.

Intermolecular forces (also commonly known as van der Waals forces) are essentially electrostatic in nature. In this (loose) sense they are based on the same interaction as are ionic bonds. In the case of ionic bonds the interactions are between charged species that are created by the wholesale transfer of electrons. This transfer of electrons is, however, not the only basis for electrostatic interactions between atoms and molecules. Indeed there are universal attractions present between any atomic or molecular species irrespective of charge or structural configuration.

The Van der Waals interaction is the sum of three distinct interactions, namely, orientation interactions, induction interactions, and dispersion interactions. The orientation and induction interactions are dependent on the presence of molecular structures with fixed dipoles. In the absence of these fixed dipoles the orientation and induction interactions do not occur. The dispersion interaction however, is a ubiquitous force occurring between *any* set of atoms or molecules.

The orientation interaction is an attractive interaction which occurs between two fixed dipoles. The name *orientation* interaction arises specifically because the strength of these interactions is dependent on the orientation of the fixed dipoles with respect to each other. The induction interaction, also attractive, relies on the presence of a fixed dipole inducing transient dipoles in nearby species. These transient dipoles then interact with the fixed dipole creating the induction interaction.

Finally we have the dispersion interaction. We shall cover this particular interaction in some detail as it is the most relevant to the work described in this thesis. The nanoparticles used in this study are charge neutral and possess no permanent electric dipoles. As such, it is dispersion interactions that will dominate the interparticle interactions. To understand the basis of the dispersion interaction, it is useful to start with a simple classical model. Elements of a more complicated quantum mechanical approach will be introduced later.

Consider two classical Bohr hydrogen atoms. At any one point in time, due to the relative positions of the nucleus and the orbiting electron, such an atom will have an instantaneous dipole moment. This dipole will induce a transient dipole in the second atom. The energy of the interaction between these dipoles can be calculated using purely classical arguments to give

$$V = \frac{2h\nu\alpha^2}{(4\pi\epsilon_0)^2 R^6},$$ (2.15)

where ν is the electronic orbital frequency, α the polarizability of the atoms, and R^{-6} is the separation of the atoms [30]. London performed the calculation using quantum mechanical methods and found that the same R^{-6} distance dependence was obtained. In fact, the classical and quantum mechanical results agreed to within a numerical constant [31].

The strength of the dispersion interactions can be quite large considering they seem to appear from nowhere. Dispersion interaction strengths between atoms in contact can be of the order of $\sim k_b T$. It is therefore not surprising that the interaction strength between macroscopic objects can be considerable. The London theory of dispersion interactions [31] makes the assumption that the field from a transient dipole is instantaneously experienced by the atom it is interacting with. In actuality the field takes some finite time to traverse the distance between the atoms. For distances where the separation is of the same order as the wavelength of the electric field fluctuations ($\leq$ 10nm [32]) the non-retarded R^{-6} relationship holds [33]. At distances much greater than this ($\geq$ 50nm [32]) the retarded R^{-7} dependence dominates, with a smooth transition from R^{-6} to R^{-7} between these separations.

Based on these calculations there are several different interaction potentials which have been defined in order to model the interactions of atoms and molecules. The potential functions must combine both the attractive dispersion forces and repulsive short range interactions due to electronic orbital overlap. Probably the most well known is the Lennard-Jones potential (also known as the 6-12 potential, Figure 2.7). This potential models Van der Waals attractions in the non-retarded regime with the R^{-6} term, while the short range

repulsive forces are modelled by the R^{-12} term.

$$V(R) = 4\varepsilon\left[\left(\frac{\sigma}{R}\right)^{12} - \left(\frac{\sigma}{R}\right)^{6}\right]$$
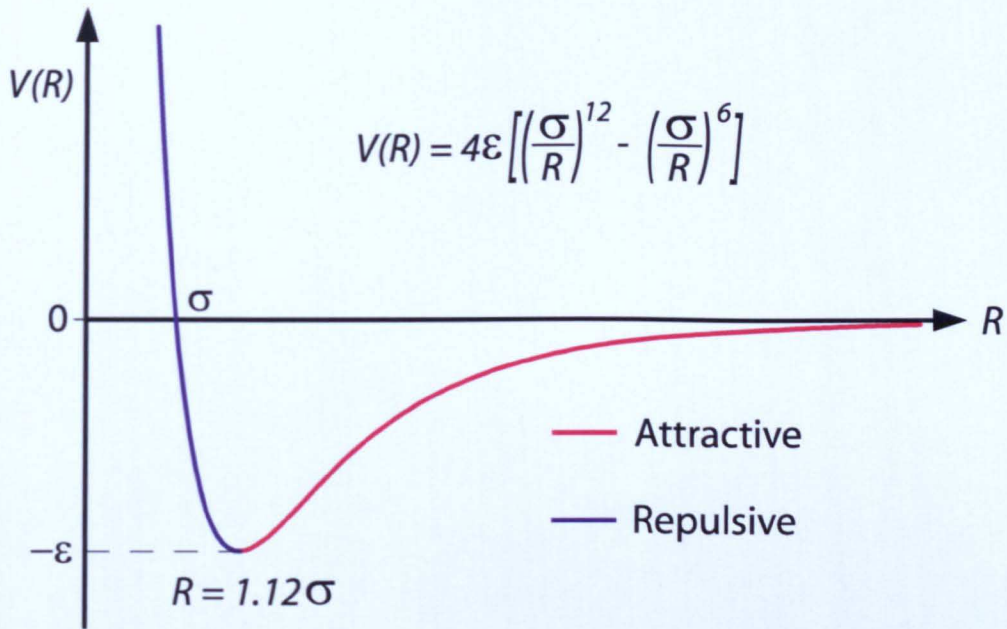
Figure 2.7: The Lennard-Jones potential. The terms σ and ϵ are the hard sphere diameter of the interacting species and the depth of the interaction. These are material dependent properties specific to the system in question.

The atomistic/molecular view of the Van der Waals force was first extended to encompass the interactions between macroscopic objects at small separations by Hamaker [34]. Making the assumption that the atomic Van der Waals interactions are additive, the interaction between macroscopic objects was calculated by a simple integration over their geometric shapes. Using this method Hamaker calculated equations for the interaction between a range of geometric shapes. For example, the equation for the Van der Waals interaction between two semi infinite slabs separated by a distance L is given by [30, 34],

$$V = -\frac{A}{12\pi L^2}, \tag{2.16}$$

The constant A is dependent on the physical properties of the material which make up the two slabs and the intervening media. This material depen-

dent parameter is known as the Hamaker constant. The Hamaker constant for a particular system is directly linked to the strength of the Van der Waals interactions in that system. As such, the Hamaker constant is an oft quoted value, used to quantify the strength of interactions between various materials separated by different media.

In the simple model of pairwise addition of atomic interactions put forward by Hamaker [34], the Hamaker constant is only dependent on the atomic density and polarizability of the interacting media. This theory fails to incorporate many-body effects: the interaction between two atoms will be influenced by their neighbouring atoms. A later, more complete treatment of these interactions was presented by Lifshitz [35]. In this approach the materials are treated as continuum objects with certain dielectric properties. The Hamaker constant is then calculated directly from these dielectric properties. This approach has the advantage of automatically incorporating many-body effects.

Due to the complexity of Lifshitz theory we limit out discussion to the calculation of the Hamaker constant for an interaction between two media, 1 and 2, across a third medium 3. The Hamaker constant for such a system can be calculated using the following equation,

$$A_{123} = \frac{3}{4}k_b T \left(\frac{\varepsilon_1 - \varepsilon_2}{\varepsilon_1 + \varepsilon_2} \right) + \frac{3h}{4\pi} \int_{\nu_1}^{\infty} \left(\frac{\varepsilon_1(i\nu) - \varepsilon_3(i\nu)}{\varepsilon_1(i\nu) + \varepsilon_3(i\nu)} \right) \left(\frac{\varepsilon_2(i\nu) - \varepsilon_3(i\nu)}{\varepsilon_2(i\nu) + \varepsilon_3(i\nu)} \right) d\nu \tag{2.17}$$

where ε_1, ε_2, and ε_3 are the static dielectric constants for the three media. However, at nonzero values of frequency the dielectric response function is complex. An estimate of this value can be obtained via knowledge of the absorption spectrum for the material (related to the imaginary part of the

dielectric response function) and the use of the Kramers-Kronig (K-K) relations which relate the real and imaginary parts of a complex function [36]. $\varepsilon(i\nu)$ are the values of the complex dielectric response functions for the three media calculated at the frequency,

$$\nu = \left(\frac{4\pi^2 k_b T}{h}\right).$$

(2.18)

The dielectric response of a material is then estimated using the following equation [37],

$$\varepsilon(i\nu) = 1 + \frac{C_{UV}}{1 + (\nu/\omega_{UV})^2}$$

(2.19)

where C_{UV} and ω_{UV} are, respectively, the absorption strength and the characteristic absorption frequency (in the ultra-violet range).

2.5 Phase transitions

In the previous sections we have discussed the properties of individual colloidal nanoparticles. We have described how they are synthesised, how their small size affects their electronic structure and individual conduction properties, and how the forces that govern their interactions with each other are derived. From this discussion we see that nanoparticles possess some extremely interesting, and technologically useful, physical properties. In order to exploit these properties to their full potential, however, methods for the controlled deposition of nanoparticles into ordered structures need to be developed. The goal of arranging nanoparticles into hierarchical structures with predefined length scales has been the subject of much scientific endeavour and a wide variety of differing techniques have been suggested and studied.

Nanostructures and molecular assemblies have been formed via the direct manipulation of individual components, such as using an AFM or STM tip to arrange individual molecules [38]. This approach gives the experimenter a high degree of structural control but can be prohibitively time consuming for the formation of large, or multiple, structures.

As discussed in the introduction, ordered patterns are often produced in nature via self-organisation processes which are often related to a phase transition. A system which shows a marked propensity for such self-organisation is that of thin liquid films on solid substrates. Patterns ranging from the micron up to millimeter length scales have all been observed in thin fluid layers. These patterns can be caused by an array of different physical processes, including the dewetting of the fluid layer from the surface, and hydrodynamic effects such as the Marangoni effect. This appears extremely advantageous for the production of ordered structures from colloidal nanoparticle solutions. We need only apply a thin film of the solution to a surface and, by careful control of experimental parameters, patterns of the desired length scale should spontaneously form.

Given that phase transitions play such a pivotal role in pattern formation mechanisms, it is imperative that we understand the underlying physics of phase transitions, *i.e.* why and how certain patterns form and how they will evolve in time. The following section gives an overview of the physics of phase transitions by focussing on the de-mixing of a two component liquid system. Quite apart from the fact that this particular phase transition may play an important role in nanoparticle pattern formation (the two liquid components being represented by the nanoparticles and the solvent), the ideas behind it are universal and may be applied to many other processes common in thin

fluid layers such as wetting transitions.

2.5.1 Liquid-liquid de-mixing

Phase transitions may loosely be described as a change in the relative importance of two or more factors. In the example of the de-mixing of two liquids these factors are the enthalpy of mixing and the entropy [39]. As we will see later, in the wetting transition underlying the dewetting of thin liquid films on surfaces the factors of interest are the surface free energy and the intermolecular interactions within the liquid.

This balance between factors controlling the phase transition is reflected in the free energy of the system. The choice of which specific free energy value best applies is dependent on the system. For the liquid-liquid de-mixing problem [40], a free energy with the same form as the Helmholtz free energy is applicable (*i.e.* where changes occur at a constant volume).

$$F = U - TS. \tag{2.20}$$

In this situation, U is the internal energy of mixing and S is the entropy associated with mixing. The system in question will always strive to adopt the structure/composition of lowest free energy. However, a simple knowledge of the equilibrium phases with the lowest free energy is not sufficient to explain the wide variety of structures obtainable in such systems. Knowledge of the *kinetics* of the specific process by which the phase separation occurs is needed to interpret the many patterns observed [41]. In reality, on passing through a phase transition the atoms/molecules of a system will not instantaneously rearrange themselves into the structure with lowest free energy. The constituent parts of the system need time to rearrange themselves into this equilibrium

structure.

The time scales for this rearrangement may be long compared to experimental timescales. Thus, the system can be seen to be passing through a number of different structures, and in some instances even though these structures are not in equilibrium they can be effectively frozen into place by appropriate choice of experimental parameters.

To understand fully the variety of structures that can be produced we need to understand the mechanisms by which the phase transitions occur, and how these mechanisms affect the structures formed en route to equilibrium. By plotting the free energy with respect to a changing parameter of the system, e.g. the thickness of the film in the case of de-wetting, or the volume fraction of one of the components in the case of the mixture of two liquids, we can observe qualitatively why phase separation occurs. Figure 2.8 shows a representation of the free energy curve with respect to volume fraction of one of the components, for a mixture of two liquids, under two different sets of conditions. The two different situations of **(a)** and **(b)** represent the same system at two different temperatures. Let us first consider the system described by **(a)**.

We begin with a mixture having a volume fraction of ϕ_0 and separate this into two mixtures with respective volume fractions of ϕ_1 and ϕ_2. By consideration of conservation of the total amount of liquid [40], the free energy of the separated system can be interpreted graphically.

Connecting the points on the free energy curve corresponding to ϕ_1 and ϕ_2, and then reading off the value of free energy on this line corresponding to a volume fraction of ϕ_0 gives the free energy of the separated system (F_{sep}). By comparing this value to the free energy of the original composition (F_0) we observe that there is a free energy cost associated in moving the system
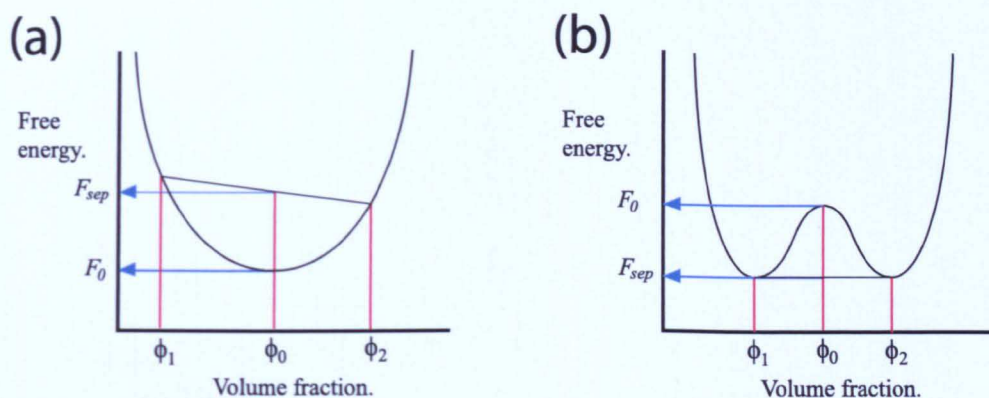
41

Figure 2.8: The free energy of mixing is plotted with respect to the volume fraction of one component of a two liquid system (liquid A and liquid B). Graphs **(a)** and **(b)** represent the same system with a different value of the interaction parameter χ. χ is the energy change in units of $k_b T$ of taking a molecule of A from a pure environment of A and placing it in a pure environment of B. For such a system, where the interaction energies between different species are held constant, χ is a function of the temperature alone; thus **(a)** and **(b)** represent the same system at two different temperatures.

from the original composition into two separate mixtures with the two new compositions.

From a cursory examination of the concave free energy curve shown in **(a)** we can see that an *increase* in free energy is required for *any* separation of the mixture with volume fraction ϕ_0 into two mixtures, one having a volume fraction greater than ϕ_0 and one having a volume fraction lower than ϕ_0. The concave nature of the free energy curve also implies that *any* initial composition (value of ϕ) of the system will be stable not just ϕ_0, as energy is required in order to separate this system into two mixtures, one with a higher and one with a lower volume fraction of one of the components.

However, if the interaction parameter is changed (essentially changing the temperature, if we leave the rest of the system unaltered), we can move to the situation depicted in **(b)**. Here the free energy of mixing curve has two minimum values separated by a local maximum. Therefore there is now a range

of initial compositions which can achieve a lowering of energy by separating into two phases with different compositions, namely ϕ_1 and ϕ_2, referred to as the *coexisting* compositions.

From Figure 2.8 **(b)** it can be seen that the limiting compositions for this area of instability are ϕ_1 and ϕ_2. The locus of points that the coexisting compositions trace out as the interaction parameter is changed is known as the *coexistence curve*, or the *binodal*.

However, this is not the whole picture. If we examine the area of the free energy curve between the coexisting compositions we can see two distinct situations depending on the particular value of the initial composition, (see Figure 2.9). The curvature of the free energy function,

$$\frac{d^2 F}{d\phi^2},$$
(2.21)

may either be positive or negative for initial compositions within the coexistence curve. By the same graphical method as used earlier we qualitatively calculate the free energy cost of a separation of a certain initial composition into two slightly different compositions.

In Figure 2.9 **(a)** the composition ϕ_1 is in a region of positive curvature. We can see that the free energy cost incurred, ΔF_1, is positive. Phase separation is therefore energetically unfavourable. However, if the compositions into which ϕ_1 is separated are pushed further apart, we reach a point where the phase separation does become energetically favourable.

Compositions within the coexistence curve which have a positive value for the curvature of the free energy are referred to as metastable. Small alterations in composition of the system are energetically unfavourable, but past a certain critical size they become favourable. Thus, a small fluctuation in composition

will not grow, unless it surpasses a certain critical magnitude. In this region phase separation occurs via *nucleation*, a composition fluctuation of a certain size needs to be *nucleated* before it will spontaneously grow.
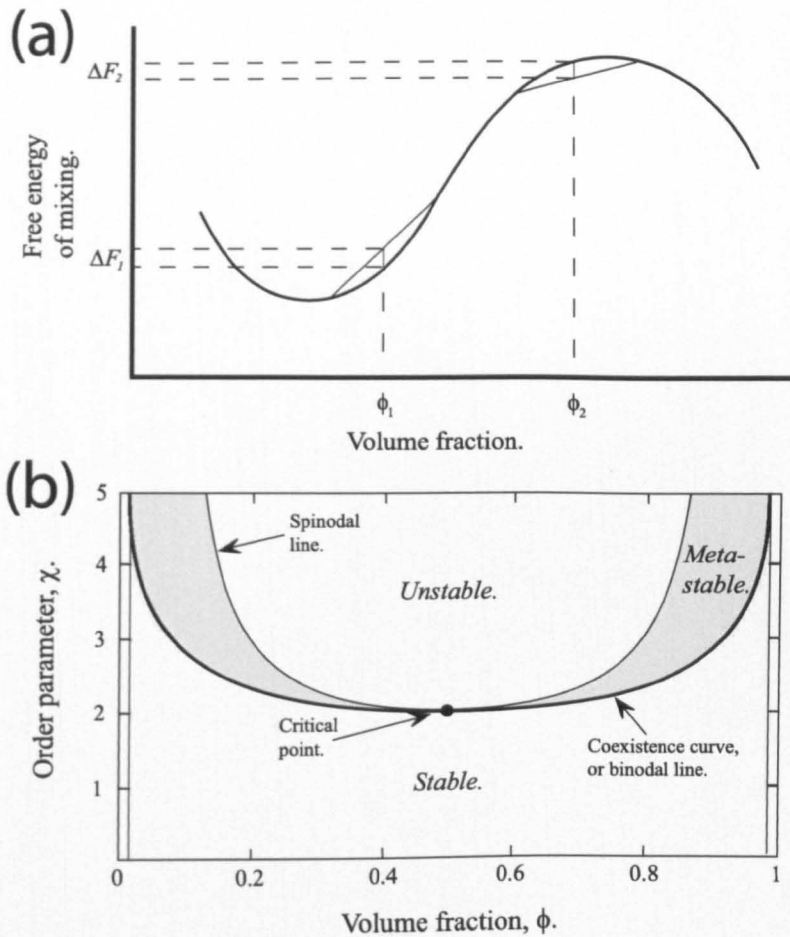
Figure 2.9: (a) Shows an enlargement of the central part of the free energy curve of figure 2.8 (b). Compositions ϕ_1 and ϕ_2 are shown in the meta-stable and unstable regions. (b) A typical phase diagram of interaction parameter against composition for the liquid-liquid system [40].

Now let us look at composition ϕ_2 in Figure 2.9 (a). Here the curvature of the free energy is negative. We can see that any small separation into phases with compositions extremely close to that of ϕ_2 will lower the free energy of the system. Therefore this composition is energetically unstable to *any* small

fluctuation in composition, irrespective of its size. Phase separation will ensue *spontaneously*. In this case phase separation occurs via a process known as *spinodal decomposition* [39].

The crossover between the metastable and unstable states occurs at the compositions where the curvature of the free energy vs volume fraction plot equals zero. The locus of compositions traced out by these points as the interaction parameter is changed forms the *spinodal line*. Figure 2.9 **(b)** shows a typical phase diagram of the composition with respect to the interaction parameter. The *spinodal* and *binodal* lines meet at the *critical point*.

2.6 Conclusions

In this chapter we have given a brief overview of nanoparticle science. The synthesis method [6] which was employed to produce the colloidal metal nanoparticles used in this work was detailed. A discussion of some of the intriguing physical properties which nanoparticles possess as a result of their small size was presented. In particular, attention was paid to the alteration of a particle's electronic energy level structure as a result of reduction in size to the nanoscopic range. Single electron charging, and the conditions under which it can occur in nanoparticle systems, were also detailed. Finally, brief discussions of intermolecular forces and phase transitions were given, with the later discussed using the example of de-mixing in a two component liquid-liquid system.

Chapter 3

Atomic force microscopy

This chapter will centre on a description of the main experimental technique employed in this study, namely atomic force microscopy (AFM) and some of its derivatives.

3.1 Introduction

Atomic force microscopy (AFM) is the major analysis technique employed in this study. It is a widely used, non destructive surface analysis technique that allows the collection of a range of surface information including topography, chemical specificity, and charge distribution. In the following chapter we will discuss both the underlying physical principles and the design and operation of AFM, with particular attention paid to tapping mode AFM and electrostatic force microscopy (EFM).

3.2 Scanning probe microscopy

AFM is one of the many different types of scanning probe microscope to have evolved over the past two and a half decades since the initial development of the scanning tunnelling microscope (STM) in 1982 by Binnig *et. al.* [42]. All scanning probe microscopy techniques are based on a similar design principle: a probe which measures some property of the surface is brought into close proximity to the surface and scanned across it in a raster pattern. The interaction of the probe with the surface is measured at each point and used to build up, pixel by pixel, a map of the scanned area of the surface.

The different types of scanning probe microscopy are based on the many different physical properties of the surface it is possible to measure. Examples include the tunnelling current between a tip and conducting surface (STM, scanning tunneling microscopy), atomic forces (AFM, atomic force microscopy), capacitance (SCM, scanning capacitance microscopy), and electric (EFM, electric force microscopy) and magnetic fields (MFM, magnetic force microscopy). Scanning probe techniques are therefore not limited to simply providing a topographic map of the surface, they can also map spatial differences on flat surfaces due to chemical heterogeneities, charged impurities, and magnetic domains.

Apart from the wealth of data available from this kind of microscopy one of the main advantages is the unprecedented level of imaging resolution which is possible. The limits of resolution placed on optical and electron microscopes by the diffraction limit are eliminated, allowing resolution down to atomic lengths scales in certain systems. However, even with the removal of the limiting effect of diffraction on the resolving power of the microscope, there are other factors which limit the resolution of scanning probe systems. The sensitivity of the

probe is one of the main factors affecting the resolution of the microscope. This can be split into two parts related to the actual physical property being measured and the design of the probe.

For example, STM measures the quantum mechanical tunnelling current between a probe and surface. The exponential dependence of the tunnelling current on the distance between the probe and the surface provides an extreme sensitivity to small changes in the probe-surface separation so that STM techniques can regularly produce atomic resolution.

The design of the probe, however, is also vital in order to achieve optimal resolution. An ideal probe will measure the physical property in question over an infinitesimally small area of the surface. Any real probe however, will measure an average value of the property in question over a finite region of the surface. For many types of scanning probe microscopy this equates to making the tip as sharp as possible, so that the area of the surface which significantly interacts with the tip is minimized. Standard atomic force microscopy probes have sub 10nm tip radii of curvature, with specialized ultra-sharp tips having values as low as <1nm.

3.3   Atomic force microscopy (AFM)

The physical properties generally used as the basis for AFM are the long range attractive van der Waals interactions between the probe and the surface, and the short range repulsive forces due to overlap of electronic orbital. As discussed in Chapter 2 dispersion van der Waals interactions are ubiquitous forces, present between the atoms of any materials. Because of this, AFM has no limitations on the electronic nature of samples that it can be used to study, this is in contrast to the other predominant scanning probe technique STM,

which requires that the sample to be studied is conducting.

The great versatility of AFM has led to it becoming one of the preeminent analysis techniques in modern surface science. In the following section we will discuss the important factors in the design and operation of the AFM along with the different modes of its operation and the data that can be collected.

3.3.1 The AFM probe

In its simplest form an AFM probe is a spring. The forces between the surface and the probe deform the spring, this deformation is measured, and the data used to build a map of the surface. The magnitude of forces between a surface and an AFM probe are extremely small, of the order 10^{-6}-10^{-11}N. The AFM probe must therefore be sensitive enough to show a measurable reaction to this magnitude of force. The design of the AFM probe also needs to be such that it minimises noise in the form of mechanical vibrations. These two factors require the spring system to be simultaneously as soft as possible, to achieve the maximum deflection for a given force, and to have as high a resonant frequency as possible to minimise the effect of vibrational noise. We can see how these two factors influence the design of AFM probes by studying the equation for the resonant frequency ω_0 of a spring system,

$$\omega_0 = \left(\frac{k}{m}\right)^{1/2} \tag{3.1}$$

where k is the spring constant of the system and m is its effective mass. Thus, to obtain a high sensitivity to small forces we require k to be as small as possible, and to minimise the effect of vibrational noise we require ω_0 to be as large as possible. From the above equation we can clearly see that this entails making the effective mass of the AFM probe as small as possible.

Most AFM probes are based on a cantilever design where at one end of the cantilever beam there is a sharp tip which interacts with the surface. The deflection of the cantilever beam caused by this interaction is then measured. The resolution power of this type of probe is linked to the sensitivity of the cantilever to interactions with the surface, and to the sharpness of the tip. The sharpness is quantified by the tip's radius of curvature. It is therefore not surprising, considering the need to minimise both the tip's radius of curvature and the systems effective mass, that microfabrication techniques are employed in probe manufacture. Figure 3.1 shows electron micrographs of a typical cantilever-tip system.
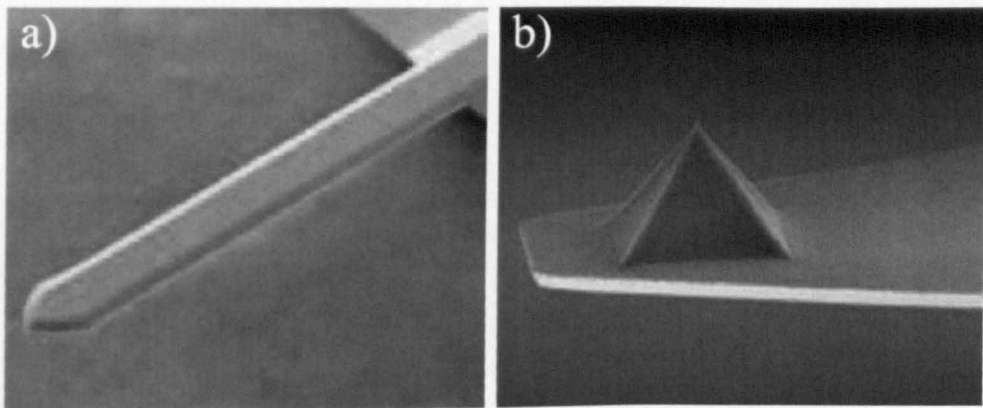

Figure 3.1: Electron micrographs of **(a)** a typical AFM cantilever and **(b)** AFM tip.

Typical silicon cantilever-tip assemblies such as that shown in Figure 3.1 can have resonant frequencies from a few tens up to several hundred kHz, force constants ranging from a few mN/m up to 50N/m, and tip radii of curvature less than 10nm.

3.3.2 Detection methods and feedback

Various different methods have been employed to detect the deflection of the cantilever in AFM systems. In the original work by Binnig *et. al.* [42], an STM was mounted at the rear of the cantilever and the change in tunnel current was used to measure the deflection of the cantilever. This particular arrangement has several distinct problems. The most common (and easily implemented) detection method in modern AFMs is *laser beam deflection.*

In this simple detection method the rear side of the cantilever is given a reflective coating and a laser beam is focused onto the rear of the cantilever. The reflected laser beam is then focussed onto a position sensitive detector. Any deflection of the cantilever causes the position of the reflected laser beam to shift on the detector and the changing signal recorded by the detector can be used to measure the cantilever's deflection. This method has several distinct advantages over other detection methods, foremost being its extreme simplicity. The negligible force exerted on the cantilever by the laser beam also means that the cantilever's motion will not be affected by the detection method (which would contaminate the AFM signal). Figure 3.2 shows the schematic for a typical AFM operating system.

The accurate positioning of the sample with respect to the tip is performed by the use of piezoelectric crystals. Typically, there are two sets of these crystals: one in the sample stage and one in the cantilever holder. The piezoelectric crystals in the cantilever holder are used to oscillate the cantilever in tapping mode operation. This will be covered in more detail shortly. The piezoelectric crystals in the sample stage are used to produce the scanning motion of the sample relative to the tip, and to change the tip-sample distance in response
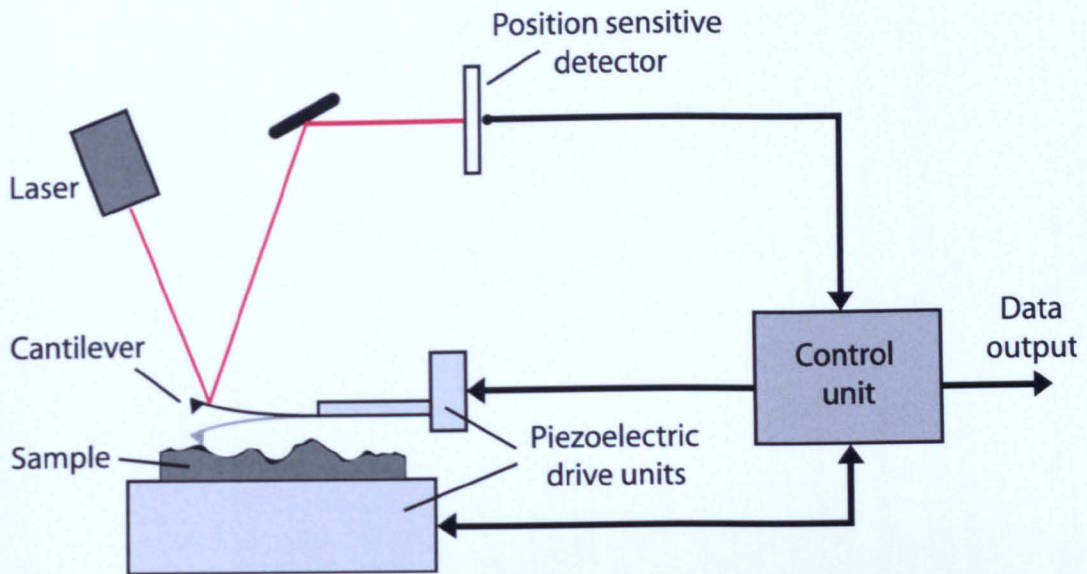
Figure 3.2: A schematic of a typical AFM operating system.

to changes in the cantilever's deflection.

Almost without exception, all scanning probe techniques use feedback to build up an image of the surface. In contact mode an AFM probe is brought into contact with the surface, causing a deflection in the cantilever. Before the scan commences a reference value for the deflection of the cantilever, the setpoint, is chosen. During scanning the surface structure of the sample causes the deflection of the cantilever to change. In response to this the piezoelectric crystals in the sample stage raise or lower the sample in an effort to return the cantilever's deflection to its set-point value. The amount that the piezoelectric crystal has to raise or lower the stage to accomplish this is used as a direct measurement of the surface topography.

3.3.3 Contact and non-contact mode AFM

As the names might suggest, contact and non-contact imaging are modes of AFM operation where the probe is respectively in, and out, of contact with

the sample surface. These two modes of operation utilise different regions of the probe-surface interaction to build up a topographic maps of the surface. In contact mode the short range repulsive forces which arise between the tip and surface when they are in contact are probed. Non-contact mode however, measures the long range Van der Waals interaction between the tip and the surface. Figure 3.3 shows a plot of the force-distance relationship for a typical probe-surface system, the regions used by contact, and non-contact modes are marked.
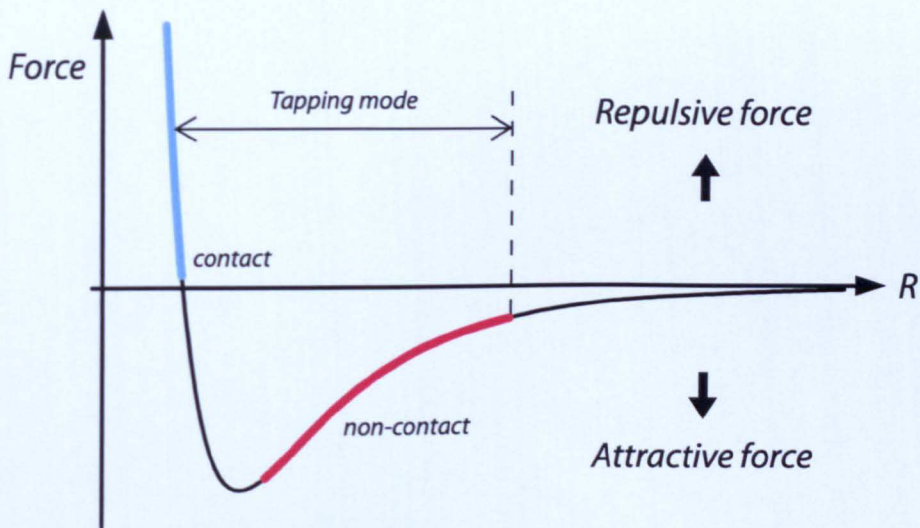
Figure 3.3: Graphical representation of a typical force distance relationship between an AFM probe and a surface. Marked are the regions utilised in contact (blue), non-contact (red), and tapping mode operation.

There are however, disadvantages to both of these modes of operation. In contact mode the large lateral forces exerted by the probe on the surface can cause damage to samples. Non-contact mode removes the risk of damaging the surface, but it does so at the expense of resolution. The relatively large distances between the tip and the surface greatly reduce the magnitude of forces which act on the cantilever and this in turn reduces the ability of the probe to resolve small surface features.

3.3.4 Tapping mode AFM

In a response to the shortfalls of both contact and non-contact mode AFM, development of the technique centered on increasing the sensitivity of non-contact mode in an attempt to increase its resolution. One of the most important developments in this endeavour was the use of an oscillating cantilever [43]. In a static cantilever AFM system the deflection of the cantilever due to the force of the surface is measured and used to build a map of the surface. By using an oscillating cantilever however, it is the force gradient experienced by the cantilever which is measured. In this method the cantilever is oscillated at its resonant frequency by a piezoelectric drive unit. When the cantilever experiences a force gradient due to the surface, the resonant frequency is shifted. The shift in a cantilever's resonant frequency due to a force gradient F' is approximately equal to [44],

$$\Delta\omega \approx -\frac{F'}{2k} \tag{3.2}$$

The minimum detectable frequency shift of an oscillating cantilever corresponds to a much smaller applied force than the minimum detectable cantilever deflection in the static cantilever case, thus increasing the vertical resolution of the probe. There are two different methods which are commonly used to measure the change in a cantilever's resonant frequency: amplitude detection and frequency detection. Amplitude detection measures changes in the amplitude of the cantilever's oscillation, and uses a feedback loop to adjust the probe surface separation to keep this amplitude at a fixed value. Frequency detection employs a phase-locked loop to measure the cantilever's frequency of oscillation and a similar feedback mechanism is used to maintain this frequency

at a set-point value.

Further improvements came with the development of a hybrid mode of AFM between that of contact and non-contact: tapping mode [45, 46]. Although this new method also employs an oscillating cantilever the cantilever is positioned closer to the surface than in standard non-contact mode, so that the tip of the probe just *taps* the surface at the "bottom end" of its oscillation. The tap on the surface reduces the cantilever's amplitude of oscillation from its free space value and induces a shift in the cantilever's frequency of oscillation. Once again a feedback loop is used to maintain the reduced amplitude of oscillation at a fixed value, and thus a topographic map of the surface is built up.

Due to the short contact times between the tip and the surface the destructive lateral forces present in contact mode, caused by the tip's motion relative to the surface, are eliminated. The excellent lateral resolution of contact mode however, is retained, with this resolution being determined by the tip's radius of curvature, and not by the distance between tip and surface as in non-contact mode. Tapping mode AFM also allows the collection of a different sort of data quite separate from the topology of the surface: phase data.

3.3.5 Phase imaging

Phase imaging measures the phase lag between the driving signal used to oscillate the cantilever and the recorded signal of the cantilever's oscillation. This phase lag is linked to the energy dissipation which occurs during the tapping of the tip on the surface. Phase imaging can highlight material differences between areas of a surface even when the whole surface appears topographically flat.

There is unfortunately no definitive theory linking the phase lag which is recorded in a certain image with that surface's material properties. The values that the phase lag adopts are dependent on a vast range of different effects including the degree of adhesion between the tip and the surface, the surface's viscoelastic properties. and the damping ratio (the ratio of the cantilever's set point amplitude to its free space amplitude). As such, it is difficult to use phase imaging to make any quantitative measurements of a surface. It is, however, an extremely useful tool for the resolution of changing material properties on a topographically flat surface.

3.3.6 Tip broadening of small objects

The limits of resolution with an AFM are quite different in the lateral and vertical directions. In the vertical direction the resolution is limited by the smallest increase/decrease in the strength of the surface interaction that the cantilever can detect. This will be linked to the sensitivity of the probe and the level of mechanical and thermal noise which is present in the system.

The lateral resolution however, is directly linked to the precision with which the sample can be positioned by the piezoelectric crystals, and thus, to the design of the AFM operating system. Take for example a sample stage that can achieve a maximum displacement of 50μm. If the sample stage use 16 bit electronics this gives us 65536 separate possible voltage values with which to control the position of the sample stage. With a 50μm maximum displacement of the sample stage this produces a minimum displacement of 50μm/65536, 0.76nm. The sample stage cannot shift the sample relative to the tip by amounts smaller than this. Therefore, structures smaller than this will remain unresolved. This problem can be easily circumvented by decreas-

ing the maximum displacement of the sample stage, or, of course, increasing the DAC resolution. There is, however, another limitation to lateral resolution determined by the design of the probe.

The fundamental limit of the lateral resolution is given by the radius of curvature of the tip. When lateral features are of the order of, or smaller, than the radius of curvature of the tip, the images are significantly broadened. Figure 3.4 shows an example of how the image of a small spherical particle on a surface is broadened by the AFM imaging process.
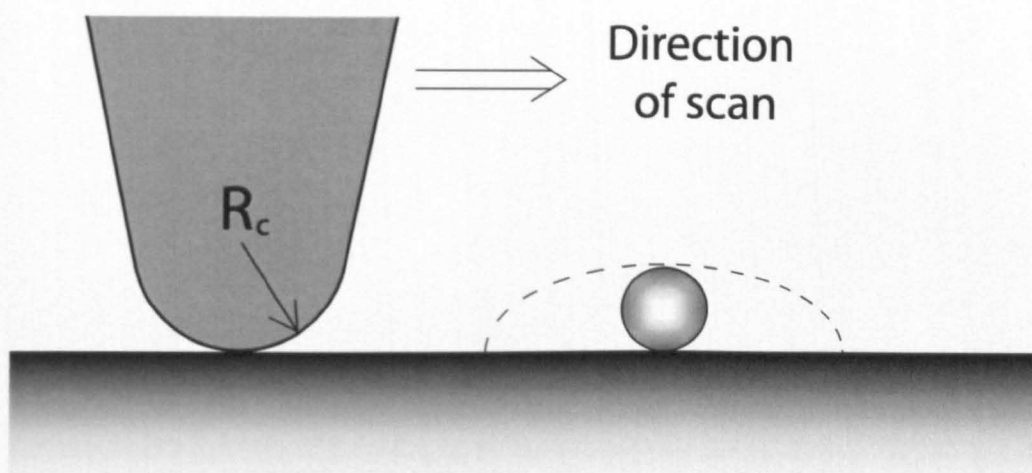
Figure 3.4: Tip broadening of small objects during AFM imaging.

The dotted line in the figure shows the broadened profile of the particle which is produced by the tip. This problem becomes even more severe for multiple, closely spaced surface features. For a single particle the image is simply broadened. If, instead, a particle is closely packed with other particles on a surface, its broadened profile will blend with that of its neighbours, if the particles are too closely spaced AFM will produce a flat, featureless image of the surface.

To combat this effect AFM probes are fabricated with as small a radius of

curvature as possible. Standard AFM probes regularly have $R_c \sim$ 10nm, while ultra-sharp tips can be purchased with R_c as low as 1nm. The drive for ever sharper tips has lead to the use of fabrication techniques such as ion beam milling, and the attachment of single walled carbon nanotubes to the apex of AFM probes [47].

3.3.7 Electrostatic force microscopy (EFM)

Electrostatic force microscopy (EFM) is a derivative of non-contact AFM, where the electrostatic interactions between charges on a surface and a metal coated tip are measured. Electrostatic force microscopy was first implemented by Martin *et. al.* [48]. Modern EFM techniques rely on a two pass scanning technique. In this method one line of an image is scanned in standard tapping mode and topographic data is collected. The tip is then raised a fixed distance from the surface and the same line is re-scanned whilst the tip is held at a constant voltage or connected to ground. During this second scan the previously collected topographic data is used to maintain the tip at a fixed distance from the surface.

By keeping the tip a fixed distance from the surface the effects of surface topographical features on the oscillation of the tip are removed. If a metal coated tip is used it is then the electrostatic interactions between this tip and charge distributions on the surface that are responsible for changes in the cantilever's oscillation. These interactions are now the basis for the EFM image of the surface which is produced. The two pass technique in essence separates the effects of topography based interactions between surface and tip and electrostatic interactions between surface charges and the tip.

Chapter 4

The morphology of

far-from-equilibrium

nanoparticle assemblies

This chapter describes the different patterns produced when colloidal gold nanoparticle solutions are spin-cast onto a range of substrates. Effects due to experimental variables such as the concentration of nanoparticle solution, surface chemistry of the substrate, and the physical properties of the solvent are investigated. Atomic force microscopy (AFM) and various image analysis techniques are employed to study the morphological changes induced in the nanoparticle assemblies. The formation of these patterns is discussed with relation to mechanisms such as spinodal dewetting, nucleation and growth of dewetting centers, and the Marangoni effect. A key conclusion is that no single mechanism underlies pattern formation in colloidal nanoparticle assemblies. Rather, a combination of processes are responsible, the dominant process depending on the particular properties of the system.

4.1 Introduction

The unique physical and electrical properties of colloidal nanoparticles have led to copious quantities of research into the mechanisms which underlie the formation of ordered nanoparticle arrays [4, 7–11, 15, 49–56]. Such arrays are vaunted as the basis for new electronic and optoelectronic devices. In order to produce this new wave of devices, an understanding of how to control not only the spacing of individual nanoparticles, but also the long range order in arrays of nanoparticles is essential.

Much previous work has centered on the production of ordered two-dimensional assemblies where the individual nanoparticles possesso a symmetrical distribution similar to that of individual atoms in a crystalline structure [49, 53, 55, 56]. Two-dimensional assemblies possessing long range structural order were formed by the drop deposition of toluene based solutions of colloidal dodecanethiol passivated gold nanoparticles [49], importantly in this case these ordered assemblies only formed when an excess of dodecanethiol was present in solution. Initially, the formation of these ordered assemblies was attributed to slower solvent evaporation rates linked to the presence of excess dodecanethiol [49]. The slower solvent evaporation rate was thought to provide more time for nanoparticles to order themselves at the solvent-substrate interface.

Later X-ray scattering experiments, however, showed that the ordered 2D arrays were instead formed at the solvent-vapour interface [53]. As solvent evaporation progresses the solvent-vapour interface is in motion and nanoparticles in solution effectively impinge on this moving interface. The excess dodecanethiol is thought to provide nucleation points for the growth of two-dimensional nanoparticle assemblies at the solvent-vapour interface. These

factors combine to collect nanoparticles at the solvent-vapour interface where they form an ordered monolayer. This layer is then deposited onto the substrate in the final stages of solvent evaporation. Using this method Bigioni *et. al.* [55] were able to fabricate ordered monolayers consisting of some 10^8 nanoparticles spanning several millimeters.

The conditions under which these assemblies form are essentially far-from-equilibrium. The relatively fast evaporation of the solvent is required in order for sufficient numbers of nanoparticles to impinge on the moving solvent-vapour interface so that formation of a complete monolayer can be initiated. However, although they are formed under far-from-equilibrium *conditions* the nanoparticle assemblies themselves are not far-from-equilibrium *structures*, the ordered close packed hexagonal array representing the thermodynamic ground state of the nanoparticle array.

Spin coating is a deposition technique that has been shown to produce colloidal nanoparticle assemblies that while being far-from-equilibrium also possess well defined correlation lengths [11]. In the drop deposition experiments discussed above far-from-equilibrium conditions provide an environment where nanoparticles can *self-assemble* into equilibrium structures [49, 53, 55]. During spin coating, however, the fast evaporation of solvent drives the solvent/nanoparticle system to *self-organise* into structures possessing well defined spatial correlations. The far-from-equilibrium structures which the solvent/nanoparticle system adopts are then frozen in place during the final stages of spin coating by the complete evaporation of solvent, effectively leaving a nanoparticle *fingerprint* of the pattern formation mechanism. In order to incorporate the wide range of different pattern morphologies produced by the spin coating process into device fabrication it is necessary that we have a more

in-depth understanding of the physical processes responsible for these patterns and how they can be affected and controlled by experimental parameters.

4.2 The spin coating process

Spin coating is widely used in many micro-fabrication processes, especially in the application of photo and electron resist layers prior to lithography. A quantity of solution is placed onto a clean substrate and then the system is spun at speeds anywhere between several hundred to several thousand rpm (revolutions per minute).
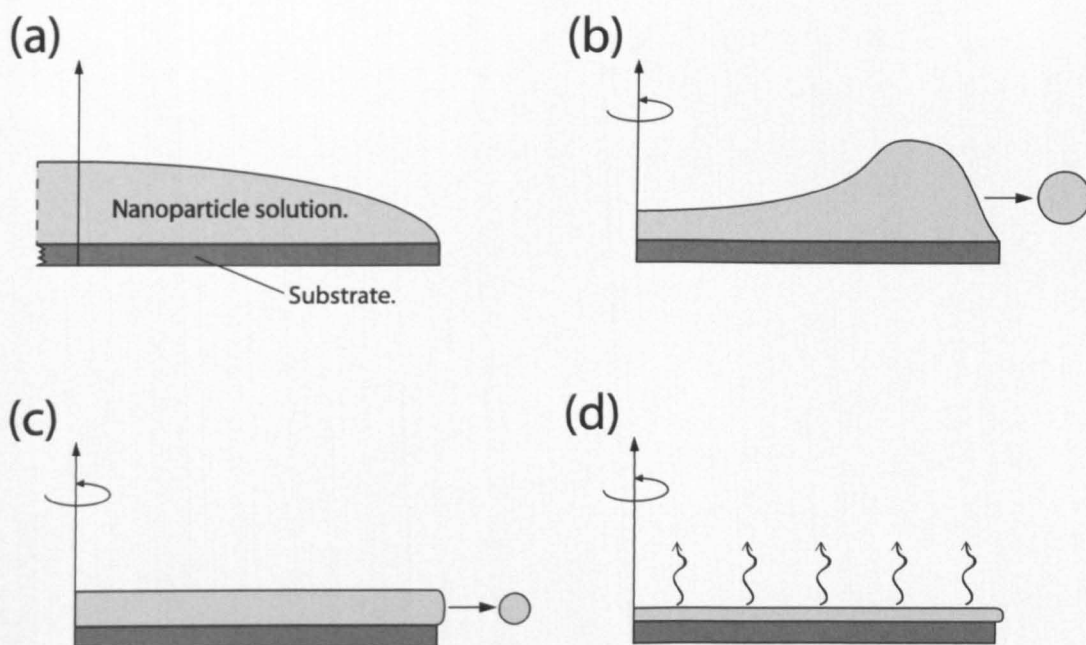

Figure 4.1: The different stages of the spin coating process. **(a)** A quantity of nanoparticle solution is placed on the stationary substrate. **(b)** In the *spin up* period, while the substrate is being accelerated to its final speed, large quantities of the solution are flung off by the high acceleration forces. **(c)** Initially after the spinning has reached a steady rate the thinning of the coating is dominated by viscous fluid flow towards the edge of the substrate. **(d)** As the coating thins further solvent evaporation becomes the dominate factor in the thinning of the fluid layer.

We refer to the spin coating process as *far-from-equilibrium* due to the

forced evaporation of the solvent that it induces. The spin coating process can effectively be split up into three stages, as shown in Figure 4.1.

The majority of the solution is thrown off the substrate due to the large acceleration forces in the initial stages of the spin coating process while the substrate is being accelerated up to the desired angular velocity. After the substrate and the fluid layer have reached a steady velocity and are co-rotating the thinning of the fluid layer is dominated by the viscous outward flow in the fluid layer. Once the viscous shear drag forces between the fluid layer and the air exactly match the acceleration due to the spinning process the fluid forms a flat layer on the substrate [57]. This layer thins evenly via a steady flow of liquid (radially outwards) and the subsequent ejection of droplets from the edge of the substrate.

As thinning of the fluid layer progresses the rate of thinning due to the outward flow of liquid decreases. This reduction of flow is due to a combination of factors: first a thinner liquid layer allows less flow, and, second, the viscosity of the liquid layer increases due to evaporation of the solvent.

As the spinning process proceeds there is a cross over in the dominant mechanism for film thinning. Thinning via outward flow of the liquid decreases and thinning becomes dominated by evaporation of the solvent from the fluid layer. There is no sharp transition between thinning via viscous flow and thinning via solvent evaporation both processes occur simultaneously. It is the viscous flow, however, which dominates at early times while evaporation of the solvent dominates at later stages.

The point at which evaporative thinning becomes dominant will depend on several factors. The most notable of these are the solvent volatility, the concentration of solute and therefore the viscosity of the solution, and the spin

speed. It is this final, evaporative thinning stage which is of importance to the structure of nanoparticle networks formed via the spin coating process. Studies have shown that, in the absence of solvent, colloidal nanoparticles are immobile on silicon oxide substrates, even up to quite elevated temperatures ($\sim$120°C), [58]. This immobility of nanoparticles in the absence of solvent means that any nanoparticle structures formed via the spin coating process are due either to the aggregation of nanoparticles in solution or they originate from dewetting patterns present in the final fluid layer just prior to complete solvent evaporation.

Examples of mechanisms which have been shown to produce spatially correlated patterns in thin fluid layers are phase separation processes such as spinodal dewetting and nucleation and growth, and hydrodynamic processes such as the Marangoni effect. In the following sections we consider each of these processes in turn and discuss their contributions to pattern formation in colloidal nanoparticle assemblies.

4.3 Thin film dewetting

In chapter two some of the details of phase transitions were introduced using a system composed of a binary mixture of liquids. As discussed there, a binary fluid system can undergo a phase transition from a mixed to an unmixed state in one of two ways, spinodal decomposition or nucleation and growth. A somewhat more relevant system to this study is that of the dewetting of a thin liquid film on a surface. The wetting transition (the change over from a stable film which wets the surface to an unstable film which dewets the surface) in this system has similar characteristics to the phase separation in the liquid-liquid system. Some of the concepts introduced for the liquid-liquid system

will help us to understand how patterns with a single predominant length scale may form via the dewetting of thin liquid films.

Early work on the rupture of thin films centered on the problem of the spontaneous breakdown of thin liquid films between bubbles, essentially a free liquid film without a substrate [59]. Later work discussed the spontaneous breakdown of thin liquid films on solid substrates [60],and we shall focus on the latter area in the following.

With respect to dewetting (the formation of holes in the film, and the subsequent beading up of the remaining liquid), a thin film may either be stable, metastable, or unstable. Which of these situations hold for a particular film is dependent on the variation of the effective interface potential with the thickness of the film.

The effective interface potential, $\phi(h)$, is defined as the free energy per unit area required to bring two interfaces from infinity to a separation of h. In the case of a thin liquid film on a solid substrate the interfaces are the solid/liquid and the liquid/air interfaces. With respect to the wetting transition from a film of uniform thickness to a de-wetted film it plays an analogous role to that of the free energy of mixing in the liquid-liquid system described in chapter two. Consider a film of liquid on a solid surface of initial thickness h. Figure 4.2 shows three possible forms for the effective interface potential of such a film, relating to the cases of stable, unstable, and metastable films.

For curve *1)* we see that the global minimum of the effective interface potential lies at a film thickness of infinity. Any decrease in the film thickness will lead to an increase in the effective interface potential, and will therefore require the input of energy. As such, decreasing the film thickness is energetically unfavourable. Such a film is *stable* for any initial value of its thickness,

h.

Curve *2)* represents an unstable film; the global minimum value of the interface potential lies at zero thickness. Such a system can therefore lower its energy by reducing the film thickness to zero, i.e dewetting the surface. Any initial thickness of film will dewet, and the film is thus unstable.
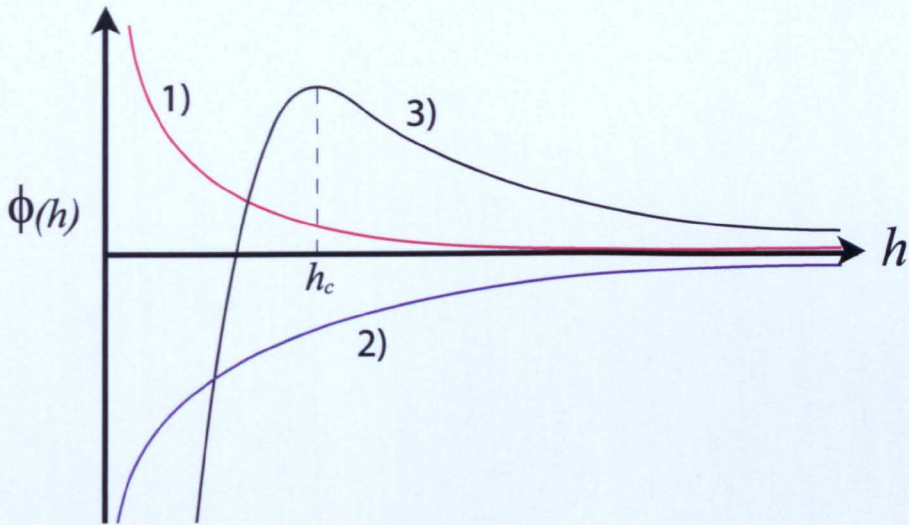

Figure 4.2: Examples of the variation of effective interface potential with film thickness for stable (curve *1*), unstable (curve *2*), and meta-stable (curve *3*) thin liquid films [61].

As with the phase separation in the liquid-liquid system, the wetting transition of a uniform film into wetted, and dewetted areas, can take place via one of two processes. First, dewetted areas may be nucleated. Nucleation of dewetted areas can be heterogeneous, caused by impurities/defects (e.g particles of dust on the surface), or homogeneous thermally-induced nucleation. Second, *spinodal dewetting* may occur, where small fluctuations in the film thickness spontaneously grow until the film ruptures.

The question of which process is responsible for the dewetting in a particular film depends on the curvature of the effective interface potential, $\phi(h)''$. Spinodal de-wetting will only occur at a film thickness where $\phi(h)'' < 0$. For

curve *2)* we can see that $\phi(h)'' < 0$ for any thickness of film, as such the film is unstable, small fluctuation in the film's thickness will grow and the film undergoes spinodal dewetting.

For curve *3)* however we see that for high values of the thickness $\phi(h)''$ is positive, indicating that any decrease in film thickness will cause an increase in $\phi(h)$, and therefore require energy, at these thicknesses the film is stable. However, if the thickness can be reduced sufficiently, via a nucleation event, $\phi(h)$ passes through a maximum at the critical film thickness (h_c) and $\phi(h)''$ becomes negative, this thinned section of the film now becomes unstable and will dewet. In this case the film is metastable, small fluctuations in the film's thickness do not spontaneously grow unless they are sufficient to reduce the film's thickness to, or below, the critical thickness. Dewetting progresses via nucleation, and then growth of dewetted areas.

In a real system matters are complicated by the fact that dewetting may occur via a combination of both *nucleation* and *spinodal dewetting*. In order to accurately distinguish between patterns caused via one process or the other we need to study the dynamics behind each of the processes.

4.3.1 Spinodal dewetting

The spontaneous rupture of thin liquid films via spinodal dewetting occurs for film thicknesses small enough that the effective range of intermolecular forces within the liquid becomes comparable to the thickness of the film [59]. In such a situation the attractive van der Waals dispersion forces will tend to drive molecules from thinner areas of the film towards thicker areas. To explain the origin of this driving force examine Figure 4.3.

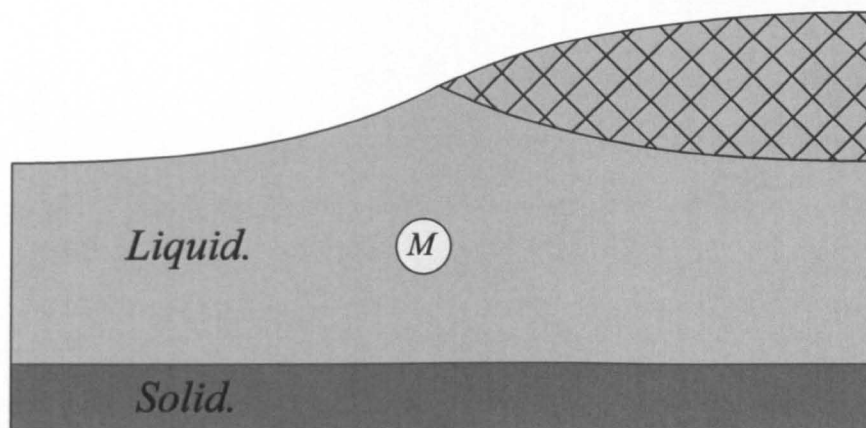From Figure 4.3 we can see that when the effective range of the intermole-

Figure 4.3: A small cross sectional area of a thin liquid film on a solid substrate, one half wavelength of a sinusoidal perturbation in the liquid/air interface of the film is shown. If the film thickness is of the same order as the effective range of the intermolecular forces then the molecule M will feel an overall attraction towards the right due to the extra interaction in that direction with the molecules in the cross hatched area of the film.

cular forces is comparable to the film thickness, then the presence of perturbations in the liquid/air interface of the film will promote intermolecular forces driving molecules from thinner to thicker areas of the film. These forces reinforce the perturbation in the film, and can cause it to grow until the film ruptures.

The factors that determine whether spontaneous dewetting of a thin film occurs are the strength and range of the interactions between liquid-liquid, liquid-substrate, and substrate-vapour molecules. It is the strength and range of these interactions that defines the form of the interfacial free energy curve with respect to film thickness, $\phi(h)$.

In most cases the strength of interaction between the substrate and vapour is negligible due to the low density of the vapour compared to either the substrate or the liquid. A simple rule of thumb for the two remaining interactions in this case is that if the substrate-liquid interactions are stronger than the liquid-liquid interactions the film will be stable, and for the reverse the film

will be unstable. The substrate-liquid interactions will tend to level out any perturbations in the film surface, and if they are stronger than the liquid-liquid interactions they can overcome the driving force for perturbation growth outlined in Figure 4.3.

Where do these random perturbations in the liquid/air interface of the film originate from? The action of the surface tension of a liquid will tend to keep the liquid/air interface as smooth as possible, thus keeping the surface free energy to a minimum. However, thermally induced roughness will always be present for the surface of any film at finite temperatures.

If the thermally roughened profile of the film surface is represented by the sum of a collection of Fourier waves [59], each individual wave may by counted as an independent degree of freedom of the system. As such the amplitude of each wave is fixed by the constraint that the increase of Gibbs surface free energy due to the extra surface area created by the presence of the wave (equal to the surface tension multiplied by the extra area) is equal to the equipartition energy, $1/2(k_B T)$.

The increase in the Gibbs surface free energy, due to the extra area of interface created by a perturbation, will act to decrease the perturbation, while the disproportionate molecular interactions will act to reinforce it. For films which undergo spinodal dewetting the increase of the surface free energy due to any perturbation is fully compensated for by the increase of the intermolecular interaction energy caused by that perturbation.

How then does this spontaneous breakdown of thin films when they reach a certain thickness promote the formation of patterns with a single predominant length scale? As discussed above it is the increase in intermolecular potential energy when a perturbation is introduced into to the film's surface

which compensates for the extra surface free energy related to the new area of surface created by the perturbation. In an unstable film there will be a range of wavelengths which grow spontaneously. There exists a cutoff wavelength below which perturbations will not grow spontaneously as the high free energy cost associated with their short wavelengths is not compensated for by the gain in intermolecular potential energy.

However, *not all perturbations in this range grow at the same rate*. One particular wavelength of perturbation will grow faster than all the others. This wavelength of perturbation will cause the film to dewet into a pattern dominated by that particular length scale. So why does one particular wavelength of surface perturbation grow faster than others? There is a large free energy cost associated with increasing the amplitude of very short wavelength surface perturbations, as these perturbations create large amounts of new surface area in the film. This retards the growth of extremely small wavelength perturbations. Conversely, long wavelength perturbations create smaller quantities of new film surface and so have a low associated free energy cost. The molecules of the liquid, however, have to flow over much larger distances in order to make the longer wavelength perturbations grow. The time taken for the liquid to flow over these larger distances means that longer wavelength perturbations will also grow slowly.

The consequence of these two opposing factors, one favouring the fast growth of short wavelength perturbations and one favouring the fast growth of long wavelength perturbations, is that there will be one particular wavelength for which the growth rate is a maximum [60]. Perturbations with this dominant wavelength, and hence dominant wave number k_d, will grow faster than all other perturbations. Thus it will be perturbations with this wavelength which

cause the film to rupture first, and the pattern of wetted and dewetted areas will adopt a characteristic length scale equal to this dominant wavelength.

Using a theoretical framework based on the Navier-Stokes equations for fluid flow, Ruckenstein *et. al.* [60] modelled the growth of surface perturbations in thin fluid films on solid substrates. Based on this model the wavelength of the dominant perturbation is given by,

$$\lambda_d = \sqrt{2} \left(\frac{8\pi^3 \sigma}{A} \right)^{\frac{1}{2}} h_0^2 \tag{4.1}$$

where σ is the surface tension of the liquid, h_0 the thickness of the film, and A is a combination of the Hamaker constants for the interactions between molecules of the liquid and between molecules of the liquid and molecules of the substrate.

Spinodal dewetting has been cited as the reason for patterns observed in a wide variety of dewetting thin film systems, ranging from the dewetting of thin metallic films heated by laser pulses [62], to the dewetting of polymer films [63]. In almost all cases the relevant factor behind the choice of spinodal dewetting as the process responsible for the observed pattern is the presence of a characteristic length scale.

However, as we shall see in the following section, the presence of a well defined characteristic length scale in a dewetting pattern does not automatically imply spinodal dewetting as the cause.

4.3.2 Nucleation and growth

Nucleation and growth is by no means a completely separate process to spinodal dewetting. The same thin film system may dewet via either process depending on the initial thickness of the film. As discussed in the previous

section, spinodal dewetting occurs when the increase in intermolecular interaction energy caused by a perturbation in the surface of a thin film offsets the free energy cost of the extra surface area created by that perturbation.

In an unstable film a range of perturbation wavelengths will spontaneously grow in amplitude and the film will dewet. However, for a metastable film there is a critical thickness for the film, above which the film is stable and below which it is unstable.

For a metastable film above its critical thickness a *nucleation event* needs to occur which locally lowers the film thickness below the critical thickness. Once the film thickness drops below the critical thickness that area of film becomes unstable and will dewet.

The driving force behind the dewetting is exactly the same as for spinodal dewetting. The difference between the two processes lies in how the dewetting starts. In spinodal dewetting the process begins spontaneously. Small thermal fluctuations in the film's surface spontaneously grow until the fastest growing perturbation ruptures the film. However, in a nucleation process there is an energy barrier which must first be surpassed before dewetting can take place. The "kick start" that nucleation requires may come from a variety of sources. Heterogeneous nucleation is nucleation caused by defects or impurities in the system, such as particles of dust on the surface or defects in the surface itself.

If the energy barrier for nucleation to occur is small enough, or the temperature high enough, random thermal fluctuations may be sufficient to initiate nucleation events. In this case the nucleation is homogeneous. The rate of nucleation events will depend on the size of the nucleation energy barrier with respect to the thermal energy.

Once a nucleation event has occurred, and a small area of the film has

dewetted, this area will then grow in size, and it will grow symmetrically in all directions. Figure 4.4 shows the initiation and subsequent growth of a nucleation event. The initial fluctuation in thickness is sufficient to locally lower the film thickness past the critical thickness, this destabilises the film and it locally dewets the surface. At the edges of the dewetted area the film must thin to expose the surface, accordingly this area of the film also becomes unstable and dewets driving the outward growth of the dewetted area.
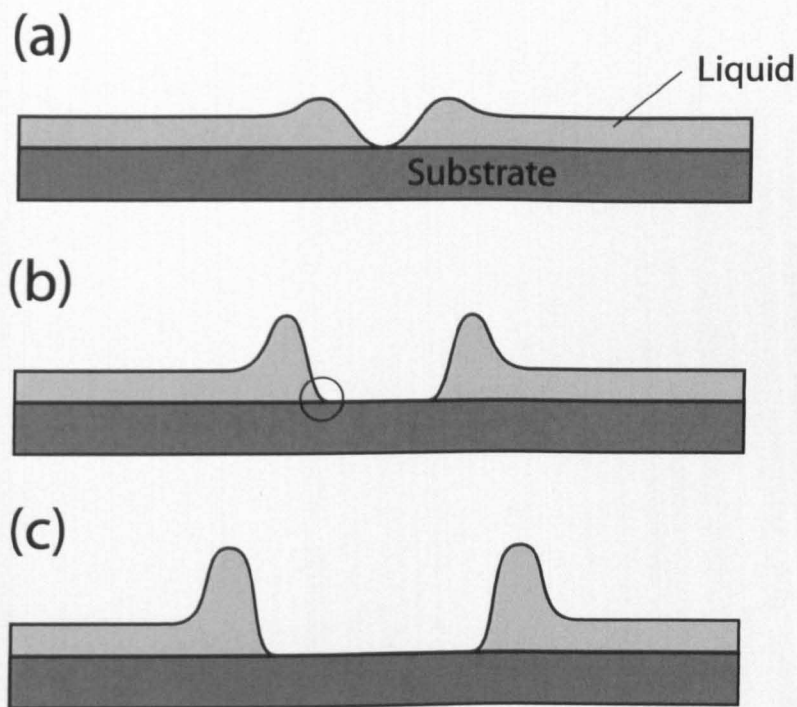

Figure 4.4: Evolution of a nucleated dewetting event in a thin film. **(a)** An initial fluctuation in the film's thickness is sufficient to overcome the barrier to dewetting and a small area dewets. **(b)** The contact region between the film and the dewetted area of substrate (area marked with circle) is itself unstable, and dewets forcing the isotropic outward growth of the dewetted area. **(c)** As dewetting continues fluid is forced outwards and accumulates into a ridge at the edge of the dewetted area.

Assuming the system is relatively homogeneous the dewetted area will grow outwards isotropically. As the film dewets outwards from the site of the nucleation event the fluid that had initially occupied this area is forced outwards.

This fluid may accumulate in a raised rim surrounding the dewetted area. The height and width of this rim are dependent on the viscosity of the fluid and therefore its ability to dissipate into the surrounding film. As such, spherical holes with raised rims are a signature motif of nucleated dewetting processes. Such structures have been observed in numerous systems [62, 64].

In real experimental situations it is very difficult to simply separate patterns into those caused by purely spinodal or purely nucleated processes. Many different factors will affect what process occurs, such as the evaporation rate of the film, or the presence of defects or surface agents. In addition, in many cases a film may be metastable but with an extremely small barrier for nucleation, making the change over between stable and meta-stable blurred rather than distinct. As such we must look to a combination of the two processes to explain many of the dewetting patterns that are observed experimentally.

4.4 The Marangoni effect

The Marangoni effect is a convection effect initiated by differences in interfacial tension. In the case of a thin liquid film, liquid will be induced to flow from areas of low interfacial energy toward areas of high interfacial tension in order to lower the interfacial energy. When a thin film consisting of volatile solvent is present on a surface, evaporation of said solvent produces a temperature gradient across the film. Any small fluctuations in the thickness of the film will therefore produce areas at the interface of the film which have different temperatures. These temperature differences across the film interface in turn correspond to differences in the interfacial tension, these variations in interfacial tension drive the convection process. The different physical parameters that control the Marangoni effect are coupled together in the dimensionless

variable M, know as the Marangoni number. The equation for the Marangoni number is given below in equation 4.2,

$$M = \frac{BhdT}{\rho\nu\kappa},\tag{4.2}$$

where h is the film thickness, dT the temperature difference across the film, ρ is the fluid density, ν is the fluid viscosity, and κ is the fluid's thermal diffusivity. The parameter B is given by,

$$B = -\frac{d\gamma}{dT},\tag{4.3}$$

where γ is the fluid's surface tension.

Colder regions of the film surface have a higher interfacial tension, as such fluid is driven from the colder regions towards hotter regions. The fluid cannot accumulate at the colder regions so it is forced downwards in the film and a convective flow is established. Figure 4.5 **(a)** shows a diagrammatic representation of this process.

These convective flows are *self-stabilising*: the flow increases the surface corrugation of the thin film which, in turn, increases the convective flow. The Marangoni effect has been shown to form a steady two-dimensional hexagonal pattern of convection cells, first observed by Bénard in the 19th century. The fluid flows up from the centers of the cells and then back down along the boundaries, see Figure 4.5 **(b)**.

Increasing the thickness of the fluid layer and the temperature gradient across it increases the level of convection. Similarly increasing the value of B increases convection. This in effect makes the interfacial tension more sensitive to changes in temperature.
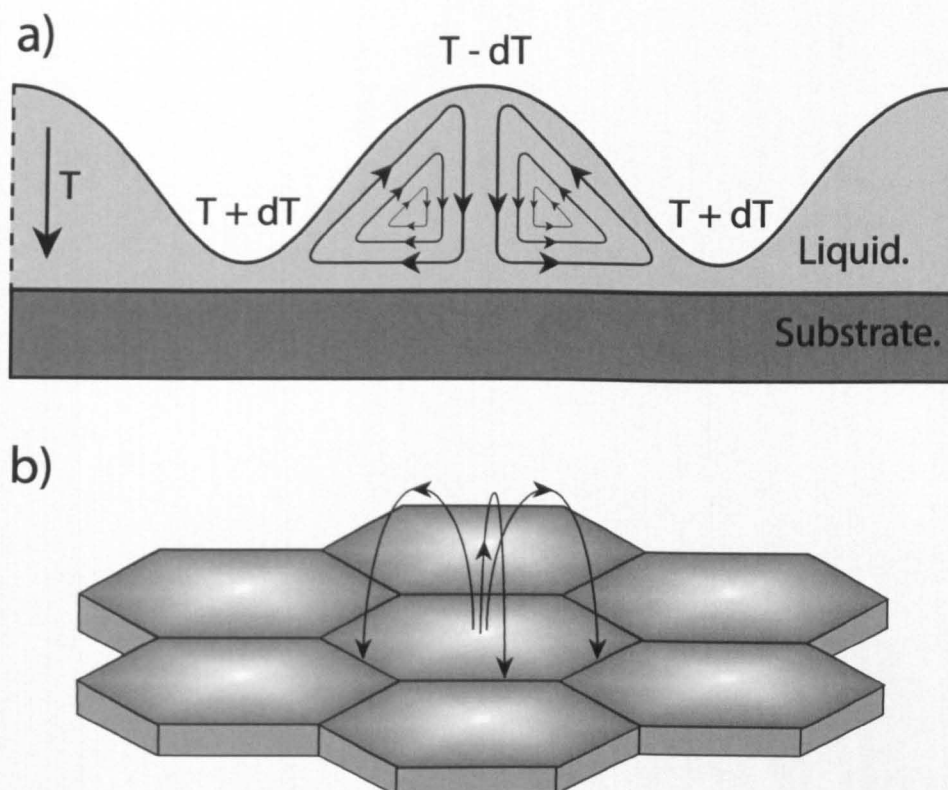
Figure 4.5: Marangoni convection in thin fluid films.

Convection is decreased by increases in the fluid's density and viscosity (both these factors affect the fluid's ability to flow). In addition increases in the thermal diffusivity of the fluid layer tend to retard the formation of convective flows. With a higher thermal diffusivity the temperature variations in the fluid layer tend to be dispersed by direct conduction of heat rather than convective flow.

There is a threshold value for the Marangoni number below which convective flows do not form. This threshold occurs at $M = 80$. As the value of M is increased further past a value of 80 the effects become more pronounced.

The patterns produced by the Marangoni effect possess a single characteristic length scale given by equation 4.4

$$\lambda = \frac{2\pi h \sqrt{8}}{\sqrt{M}}. \tag{4.4}$$

Combining equations 4.2 and 4.4 we can see that by increasing the density and viscosity we decrease the Marangoni number and therefore increase the characteristic length scale of any pattern of convection cells. The density and viscosity of nanoparticle solutions will depend on two main factors: the physical properties of the solvent and the concentration of nanoparticles present in the solvent.

In the previous sections we have discussed some of the possible mechanisms responsible for pattern formation in spin-cast nanoparticle assemblies. In sections 4.5 and 4.7 experimental data will be detailed displaying how changes in the nanoparticle concentration and the physical properties of the solvent affect the morphology of nanoparticle assemblies.

4.5   Nanoparticle concentration

The concentration of nanoparticles in solution prior to spin coating will have dual effects on the pattern forming process. The primary (trivial) effect we would expect to observe due to an increase in concentration is an increase in the nanoparticle coverage of the final pattern. However, the physical properties of the solution will also be altered by changes in nanoparticle concentration. These changes may have important influences on the stability of the film and thus on the pattern forming process.

One of the most important changes that will occur with an increase in nanoparticle concentration will be an alteration of the strength of the inter-particle interactions within the solution. Recent work by Sharma *et. al.* [65]

has shown that variations in density related to the film thickness can destabilise stable films and stabilise unstable films.

The Hamaker constants for interaction between liquid-liquid volumes and substrate-liquid volumes in a thin film depend on the density of the liquid and the substrate. These Hamaker constants are what defines the stability, or instability, of the film. If the Hamaker constant for the substrate-liquid interaction is less than that for the liquid-liquid interaction the film is unstable. If the reverse is true and the substrate-liquid interaction is stronger then the film will be stable. As the strength of both of these interactions is dependent on the density of the film we can expect changes in the film's stability with changes in its density.

Increasing nanoparticle concentration may also induce a wide range of possibly important changes to the properties of the nanoparticle solution. These could include alterations to the solution's surface tension, thermal diffusivity, viscosity, and rate of solvent evaporation. All of these factors may play pivotal roles in the pattern formation process.

To minimise the effect of extraneous variables, experiments were carried out in a systematic fashion, in order to limit any changes observed in network morphology to those caused by concentration variation. The substrates were 1cm^2 samples of Si(111) where, for each experimental run, the samples were taken from a single wafer. Samples were ultrasonically cleaned using a standard four solvent wash technique comprising rinses in ethyl lactate, acetone, methanol, and isopropyl alcohol.

Dodecane thiol-passivated gold nanoparticles in a toluene solution were produced using the synthesis method outlined by Brust *et. al.* [6]. Small angle X-ray scattering (SAXS) analysis was employed to measure the size and size

distribution of the nanoparticles. The nanoparticles were found to have 2nm core with an approximately 15% size distribution. For all experiments concerning concentration variation nanoparticles were used that had been produced in the same synthesis batch.

In order to obtain solutions of known concentration, quantities of nanoparticle solution were placed in cleaned glass vials and the toluene solvent allowed to evaporate. By measurement of the weight of the glass vial before and after this step the weight of nanoparticle precipitate was obtained. Fixed quantities of pure toluene were then used to redissolve the nanoparticle precipitate and create solutions of know concentration. Nanoparticle solutions with concentrations ranging between 0.10 ± 0.02 mg/mL, and 4.50 ± 0.02 mg/mL were created in this fashion.

These solutions were then spin-coated onto the clean substrates. Spinning was carried out at 4,000rpm for thirty seconds where the spin up period from stationary to 4,000rpm was 0.5 seconds. The same spinning parameters were used for all of the samples detailed in the following experiments. Samples were then imaged using a Digital Instruments MultiMode AFM. Each sample was imaged several times at different locations across its surface to ensure that a true representation of the nanoparticle network morphology on any given sample was obtained.

Figure 4.6 shows a selection of AFM images taken from samples with concentrations ranging between 0.10 mg/mL and 1.75mg/mL. These images were chosen for their representation of the general nature of the network on each sample. The general morphology of the networks showed surprisingly little change over the surface of a single sample, with extreme local variations only occurring in the vicinity of large particles of surface contamination.
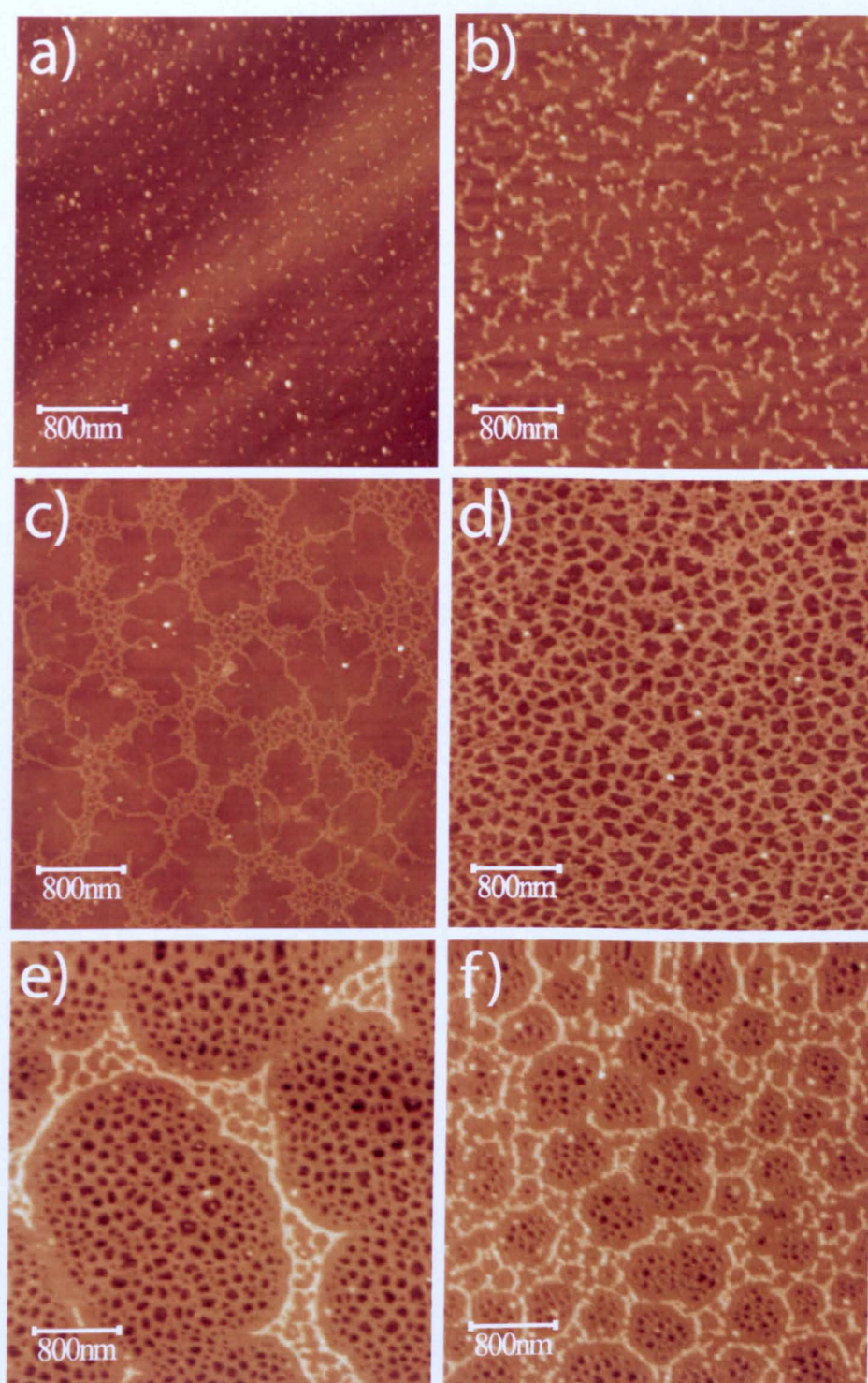
Figure 4.6: Representative AFM images of six different samples from the concentration variation experiments. All substrates are solvent washed Si(111). The concentrations are, (a) 0.10mg/mL, (b) 0.25mg/mL, (c) 0.75mg/mL, (d) 1.25mg/mL, (e) 1.75mg/mL, and (f) 2.25mg/mL. All images are $4\mu m \times 4\mu m$.

At the lowest concentrations studied, 0.10mg/mL, isolated islands of nanocrystals are formed. As the concentration is increased these island steadily become larger and more interconnected. Eventually as the concentration is increased yet further the isolated islands become completely interconnected network structures.

The network morphology seen in Figure 4.6 (**c**), is typical of the concentration range 0.50mg/mL to 1.50mg/mL, and has been observed many times in various spin coating experiments. This pattern morphology is of particular interest due to the dual lengths scales which are present within it. As can be seen from Figure 4.6 (**c**) the network is cellular in nature, with one large scale network and another smaller scale network present along the cell boundaries of the larger network. The presence of two distinct correlation lengths is highlighted by Figure 4.7. Figure 4.7 shows the 2D fourier transform and its radial average calculated for a AFM image of the 0.75mg/mL sample. The two distinct correlation lengths appear as peaks in the radially averaged Fourier transform and concentric rings in the 2D Fourier transform.

As the nanoparticle concentration is increased further still a second layer of nanoparticles begin to form, see Figure 4.6 (**e**) and (**f**). The formation of multiple layer networks will be discussed in more detail shortly. Initially we will focus our attention on single layer nanoparticles assemblies, and in particular morphologies similar to those shown in Figure 4.6 (**c**) and (**d**). The validity of each of the possible formation mechanisms which may be responsible for these patterns will be discussed in turn.
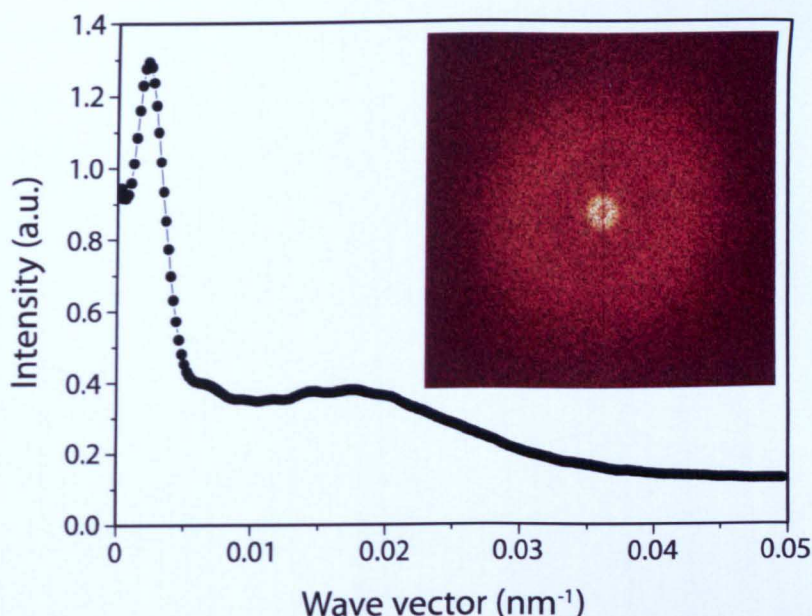
Figure 4.7: Two-dimensional Fourier transform and its radial average calculated for an AFM image of the 0.75mg/mL sample. The two distinct correlation lengths are highlighted by the peaks in the radially averaged Fourier transform. These peaks are associated with correlation lengths of ~60nm and ~450nm, corresponding to the small and large scale networks visible in Figure 4.6 **(c)**.

4.5.1 Marangoni effect

Previous studies have shown that the Marangoni number for nanoparticle solutions scales inversely with nanoparticle concentration [50]. Increasing nanoparticle concentration lowers the variation of surface tension with temperature, referring back to equation 4.2 we can see that this lowers the value of the Marangoni number. Also the thermal diffusivity of nanoparticle solutions was shown to increase with increasing nanoparticle concentration [50], again this has the effect of reducing the value of the Marangoni number.

From the results of [50] and equation 4.4 we would expect the correlation lengths of any patterns produce by the Marangoni effect to increase with increasing nanoparticle concentration. In opposition to this we see a reduction in the length scale of the patterns which are formed with increasing nanoparticle

concentration. This contradiction appears to rule out the Marangoni effect as the cause of the network morphologies we observe in Figure 4.6. We will however return to a discussion of the Marangoni effect later in this study.

With the rejection of the Marangoni effect as a possible cause for the patterns observes in Figure 4.6 we instead need to look towards alternative explanations, namely dewetting processes. There are, however, two distinct dewetting mechanisms that may be responsible. We need to observe each process in turn to determine its validity for being the formation mechanism responsible for the morphologies displayed in Figure 4.6.

4.5.2   Convective dewetting

As described in earlier sections the excess intermolecular interaction in a fluid film due to a perturbation in its surface can compensate for the free energy cost of creating the extra film surface area associated with that perturbation. This provides a driving force for the flow of liquid from thinner areas of the film towards thicker areas reinforcing the growth of that perturbation. Depending on the relative strength of the intermolecular interactions, the thin film can initialise dewetting in the film via either nucleation and growth, or spinodal dewetting. Importantly, this type of *convective* dewetting is driven by the flow of material. This is in contrast to *evaporative* dewetting, which will be discussed shortly, where dewetting of the surface is initiated by the evaporation of material from the film.

For the spin coating of nanoparticle solutions it is instructive to examine the two extreme situations of nanoparticle concentration. These equate to a film of pure toluene with zero nanoparticle concentration, figure 4.8 **(a)**, and a film of pure nanoparticles, figure 4.8 **(b)**.
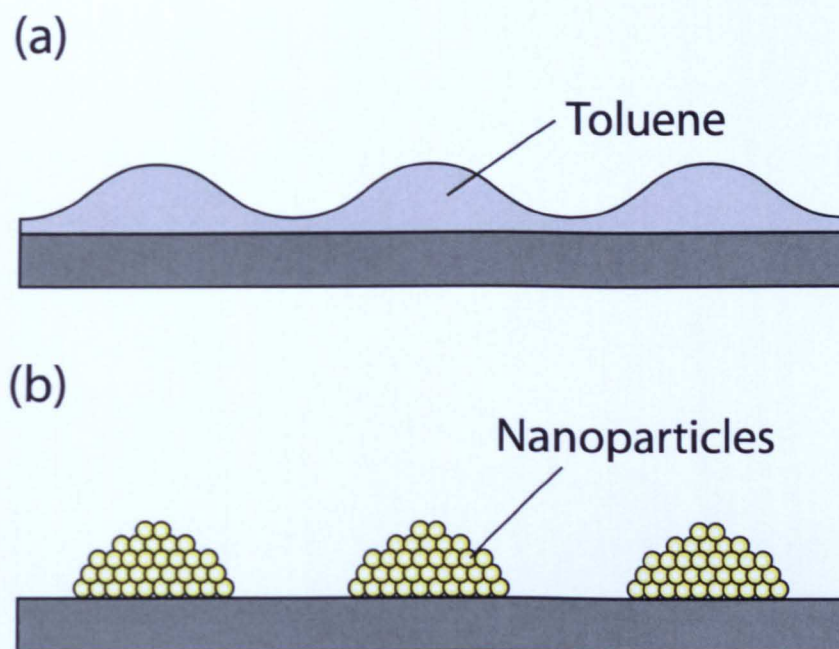
Figure 4.8: Dewetting of a thin liquid film by viscous flow in the extremes of nanoparticle concentration. **(a)** As nanoparticle concentration tends to zero we have a liquid film of pure toluene. **(b)** Moving towards complete evaporation of the solvent we are left with a pure nanoparticle film.

In the first case we have a film of pure toluene on the substrate. This is effectively the same as a nanoparticle solution with an extremely low concentration. If the toluene film were to dewet the substrate any nanoparticles present in the film would move with the solvent and we would expect them to be deposited in a pattern similar to the dewetting pattern of the toluene film. This mechanism can be easily discounted by a simple calculation of the Hamaker constant for a substrate interaction with air across a thin film. A positive value for this Hamaker constant implies that there is an attraction between the substrate and the air and the toluene film may become unstable at certain thicknesses. A negative value implies a repulsion and the film will be stable.

The Hamaker constant for the interaction between both silicon and silicon

dioxide with air across an intervening toluene medium were calculated by the Lifshitz theory using the method outlined in [37], and values for the refractive indices and dielectric constants obtained from [66]. The substrates used in these experiments were silicon with a ~ 2nm native oxide layer, therefore the true value of the Hamaker constant will lie somewhere between these two values. The values of the Hamaker constants for silicon and silicon dioxide respectively are -1.26eV and -0.04eV. The negative value of both these Hamaker constants suggests that toluene films will completely wet the substrates used in these experiments, forming stable thin films. This would appear to discount the convective dewetting of a primarily toluene based thin film as the mechanism behind the patterns observed in Figure 4.6.

This hypothesis is reinforced via direct optical microscopy observation measurements of the contact angle for toluene on native oxide covered silicon. For pure toluene drops the contact angle was so small as to be immeasurable within the experimental error, further evidence that toluene completely wets the substrates used in these experiments. These factors make it highly unlikely that the patterns we observe in Figure 4.6 arise from the convective dewetting of low nanoparticle concentration toluene films.

We do however need to consider the possibility of convective dewetting occurring in a high concentration nanoparticle toluene film. In this case instead of dewetting occurring by the flow of toluene from thin to thicker areas of the film dewetting would occur via the flow of nanoparticles. As an example let us consider the convective dewetting of a densely packed single layer of nanoparticles which completely cover the substrate surface. In order for this film to dewet and expose some areas of the substrate some of the nanoparticles must flow from the substrate onto the second layer of nanoparticles. As such

this type of dewetting would be signified by the formation of multiple layer nanoparticle clusters. An example of the structures which we would expect from this type of convective dewetting is given in Figure 4.8 **(b)**. This situation would occur at other extreme of nanoparticle concentration when, after almost total evaporation of the solvent, we are left with a dense film of nanoparticles on the surface. In the complete absence of solvent nanoparticles have been shown to be immobile on native oxide covered silicon substrates [58]. However, if just enough solvent remains to allow the movement of nanoparticles, but not to significantly dampen the strength of interactions between them, then the convective dewetting of a nanoparticle film suggests itself as a possible mechanism for the patterns observed in Figure 4.6.

The calculation of a Hamaker constant for this system is much more complicated than for the simple toluene film at low nanoparticle concentrations. The nanoparticle's dimensions, their packing, their thiol coating, and the remaining toluene in the system would all need to be accounted for in this calculation. Fortunately, we can discount this mechanism by a simple observation of the experimental data.

Convective dewetting of such a highly concentrated nanoparticle film is expected to produce multiple layer nanoparticle aggregates. Nanocrystal aggregates with multiple layers have been observed by Korgel *et. al.* [51] with the drop deposition of dodecanethiol passivated gold nanoparticles from solvents with high dielectric constants (chloroform-ethanol mixtures). The high dielectric constant of the solvent changes the balance of the van der Waals nanoparticle-nanoparticle and nanoparticle-substrate interactions promoting the convective dewetting of the nanoparticle film and the formation of multiple layer nanoparticle aggregates.

A similar effect is seen here when spin coating experiments are carried out with butanethiol passivated nanoparticles. Figure 4.9 shows an AFM image of a native oxide covered silicon sample that has been spin coated with butanethiol passivated nanoparticles from a toluene solution. Multiple layer aggregates are clearly displayed with the insert to Figure 4.9 showing a line section taken through one of the aggregates. The aggregate displays a maximum height of $\sim$ 16nm, equating to 4-5 layers of nanoparticles.
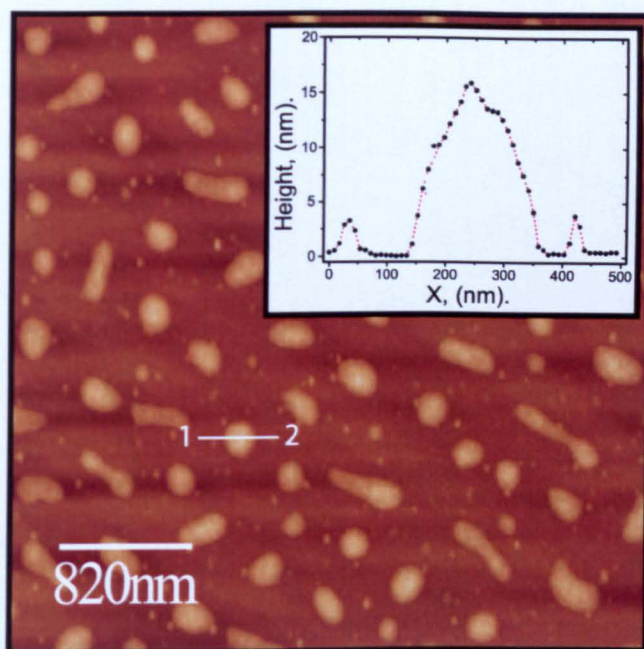
Figure 4.9: AFM image of butanethiol passivated nanoparticles, spin coated from a toluene solution onto native oxide covered silicon. The insert shows a line section taken along the line marked 1-2 in the image.

The presence of these multiple layer aggregates can be explained by the much smaller inter-particle distances between nanoparticles passivated by butanethiol as compared to dodecane thiol. The smaller interparticle distance leads to much stronger nanoparticle-nanoparticle interactions. The stronger nanoparticle-nanoparticle interactions destabilise the thin nanoparticle film promoting dewetting of the surface, and the consequent formation of multiple

87

layer nanoparticle clusters.

When spin coating solutions of dodecane thiol passivated nanoparticles however, as detailed in Figure 4.6, we observe nanoparticles forming in a second layer only when the concentration is increased to a point where there is no longer any space for them in the initial layer. This absence of multiple layer nanoparticle aggregates indicates that the convective dewetting of a concentrated nanoparticle film by the flow of nanoparticles is not the mechanism responsible for the networks observed in Figure 4.6.

Having provided evidence arguing against dewetting via convective flow in a liquid film, either of nanoparticles or of toluene, where then do we turn for an explanation of the networks seen in Figure 4.6?

4.5.3 Evaporative dewetting

Given the nature of the final stages of the spin-coating process-a fast, forced evaporation of solvent-it is then not surprising that solvent evaporation plays a major role in the pattern formation process. In the previous section the thinning and eventual dewetting of the nanoparticle solution film occurred via the flow of liquid within the film. However, in the case of spin coating it is the removal of solvent from the film via evaporation which initiates dewetting.

Along with the evaporation of solvent, the interparticle attractions present within a nanoparticle solution can also have important implications for pattern formation. The attractions between nanoparticles in a solution are not strong enough to promote aggregation of nanoparticles. This statement is borne out by the fact that such solutions are stable with nanoparticles remaining soluble over long periods of time. When such a solution is placed on a substrate, however, if there is a preferential attraction between the substrate and the

nanoparticles then surface mediated aggregation of the nanoparticles may occur. If the attraction between nanoparticle and substrate is strong enough a nanoparticle rich layer forms on the substrate whilst still under solution. For example Moriarty *et. al.* [11] noted that thiol passivated gold nanoparticles form two dimensional aggregates on a native-oxide covered silicon substrates. Tapping mode AFM images taken under a toluene solution in [11] show the formation of these aggregates.

The aggregation of nanoparticles under their mutual attractions within a solvent-nanoparticle layer and the dewetting of the substrate via solvent evaporation were combined in a seminal work by Rabani *et. al.* [52]. In this study, and in a later modifications by Martin *et. al.* [1], Monte Carlo simulations of the drying of two-dimensional nanoparticle-solvent films were performed. In the simulations a two-dimensional lattice was created, where each site is occupied by either solvent, vapour, or nanoparticle. In each step of the simulation the solvent/vapour sites are examined in turn and an attempt is made to convert them to vapour/solvent. The conversion is performed with an acceptance probability given by,

$$p_{acc} = min\left[1, exp\left(\frac{-\Delta H}{k_B T}\right)\right],\qquad(4.5)$$

where ΔH is the energy change associated with such a conversion. This energy change is calculated from the total energy of the system:

$$H = -\varepsilon_l \sum_{<ij>} l_i l_j - \varepsilon_n \sum_{<ij>} n_i n_j - \varepsilon_{nl} \sum_{<ij>} n_i l_j - \mu_l \sum_i l_i,\qquad(4.6)$$

where ε_l, ε_n, and ε_{nl} represent the interaction strengths between two liquid lattice sites, two nanoparticle lattice sites, and a liquid and nanoparticle lattice

site respectively, and μ is the chemical potential.

In between the attempts to convert the solvent/vapour sites, the nanoparticles perform a random walk on the lattice. Each step of the random walk is again performed dependent on a probability linked to the energy change induced by such a movement. The nanoparticles are also constrained by only being allowed to move into wet areas of the substrate. This constraint mirrors the immobility of nanoparticles on silicon substrates in the absence of solvent [58]. The mobility of the nanoparticles on the substrate is varied in the simulations by changing the number of attempts made to move each nanoparticle in between each solvent/vapour evaporation/condensation step.

These simulations have displayed an ability to reproduce a wide range of patterns observed in experiments concerning the drying of nanoparticle solutions, not least the spin coating experiments detailed here. Figure 4.10 shows two tapping mode AFM images of spin cast nanoparticle networks along with selected outputs of this type of simulation.

The two simulation outputs seen in Figure 4.10 (c) and (d) represent evaporative dewetting in the spinodal and nucleated regimes respectively. Which regime occurs in a simulation is dependent on the value of the chemical potential. The chemical potential defines the equilibrium state of the solvent on the surface. The spinodal type patterns observed in the spin coating experiments are well modelled by the simulations. As such, we will concentrate our attention on the cellular patterns.

The cellular type patterns produced by the simulation, Figure 4.10 (d), are produced in the nucleated dewetting regime. In the nucleated regime dewetted areas appear randomly spaced in the lattice and grow outwards. Even though these nucleation event are initially randomly spaced it has been shown that
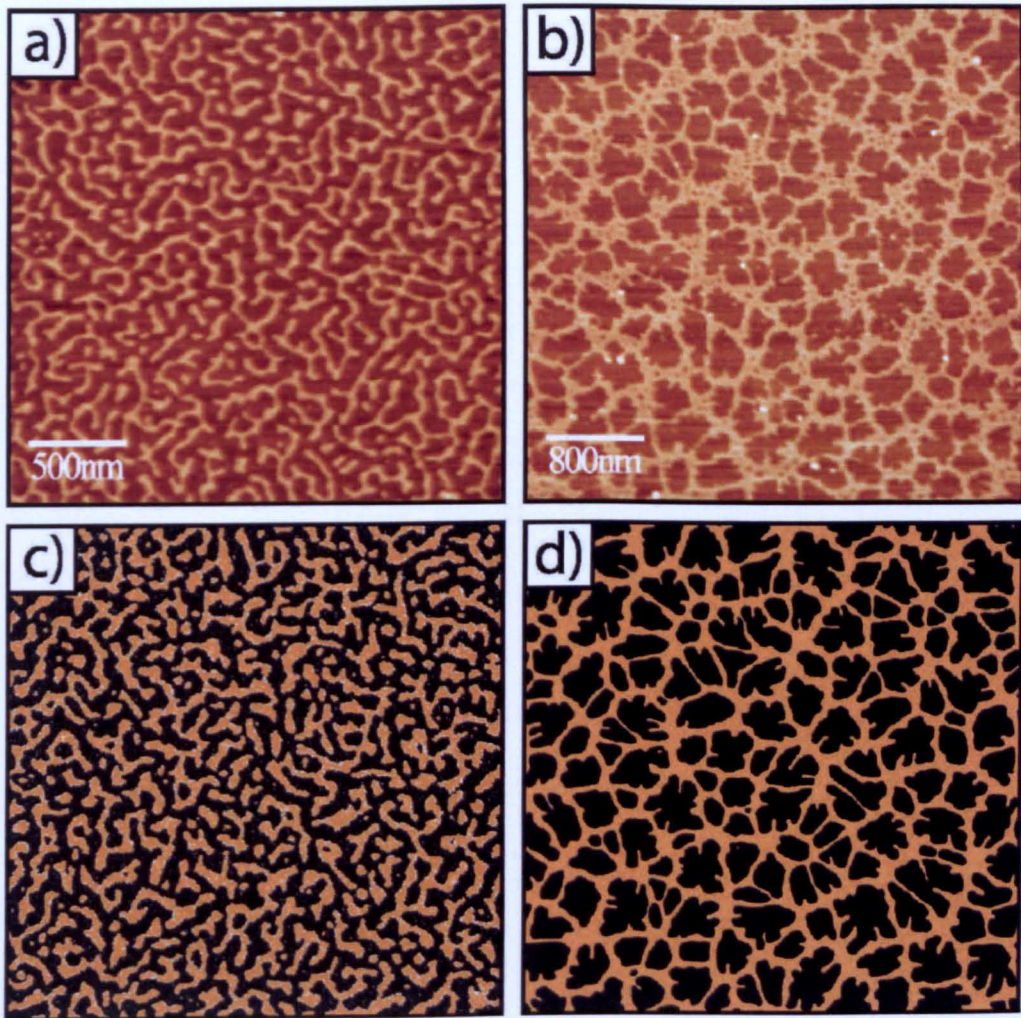
Figure 4.10: Comparison between experimentally obtained nanoparticle networks and the results of simulations. **(a)** and **(b)** Tapping mode AFM images of spin cast nanoparticle networks, image sizes are $2.5\mu m \times 2.5\mu m$ and $4\mu m \times 4\mu m$ respectively. **(c)** and **(d)** Results of simulation for different parameter sets, (*images reproduced courtesy of Christopher P. Martin, the University of Nottingham*).

networks with a single dominant length scale can be produced by this sort of nucleated evaporative dewetting [1,52].

As the dewetted areas grow they drag nanoparticles with them. Depending on the concentration and the mobility of the nanoparticles, closely spaced dewetting areas can coalesce. This coalescence washes out smaller length scales from the dewetting patterns, leaving a pattern with a single dominant correlation length. The magnitude of this correlation length is controlled by the rate of nucleation events, which in turn is defined by a combination of the value of the chemical potential, and the concentration of nanoparticles. Areas of the lattice with a higher concentration of nanoparticles have a lower frequency of nucleation events. As the dewetting areas grow outwards, dragging nanoparticles with them, the concentration of nanoparticles in the remaining wet areas of the film increases. This in turn slows the frequency of nucleation events until we end up with a cellular network that has solid blocks of nanoparticle present at the nodes of the network, as seen in Figure 4.10 **(d)**.

This is the first major discrepancy between the results of the simulation and the experimental data we observe. The simulation reproduces the large scale network, but not the smaller scale network present at the nodes of the larger network as seen in the experimental images of Figure 4.6. This discrepancy arises because of the necessary digital nature of the simulations, and the fixed value used for the chemical potential. In the simulations only a single layer, consisting of either solvent or nanoparticles, is modelled, and the value of the chemical potential for the solvent remains fixed throughout the simulation. However, in a real spin coating experiment, the solvent evaporates in an analogue fashion, with a gradual thinning of the solvent film. Extensions to these simulations are currently underway at the University of Nottingham

to extend the simulations to three-dimensions. These extensions will hopefully more faithfully represent the changing solvent evaporation rate with film thickness and also incorporate any effects due to hydrodynamic flow.

The conversion of a solvent cell to a vapour cell in the simulation is equivalent to all the solvent in a small area of the film evaporating to expose the substrate. In reality the likelihood of this happening will depend on the thickness of the solvent film. Thus as the spin coating process proceeds the gradual thinning of the solvent film by evaporation will increase the probability of a *nucleation event occurring*.

This explains the formation of the second smaller scale network at the nodes of the larger network. The initial evaporative dewetting, and growth of the dewetted areas, forms the large scale network. This forces the nanoparticles into highly concentrated regions at the cell edges of the large scale network. This increase in concentration temporarily slows solvent evaporation in these areas and thus lowers the frequency of nucleation events. However, as the spinning process continues the forced evaporation of the solvent thins the solvent layer increasing the probability of nucleation events. The areas at the edges of the cells in the large scale network then undergo a nucleated evaporative dewetting process similar to the one which formed the initial network, only on a much smaller scale.

4.5.4 Multiple layer networks

From Figure 4.6 we see that at concentrations between 1.25mg/mL and 1.50mg/mL a transition occurs from single layer networks to the formation of dual layer networks. The nanoparticles form networks in this second layer that are almost identical in morphology to those formed in the initial layer. They

consist of networks with two characteristic correlation lengths, the smaller scale network present at the cell edges of the larger network. Figure 4.11 **(a)** shows an example of a network with two distinct correlation lengths present in the second nanoparticle layer, this image was taken on the 2.00mg/mL sample. To highlight the two length scales present in the second nanoparticle layer the image has been converted to a binary image where only the structure present in the second nanoparticle layer is visible **(b)**. The two-dimensional Fourier transform and its radial average have been calculated for this binary image **(c)**. As with the Fourier transform of the dual length scale networks in the first nanoparticle layer (Figure 4.7), the presence of two distinct correlation lengths is displayed by the presence of two peaks in the radially averaged Fourier transform.

These second layer networks follow a similar evolutionary pattern with increasing nanoparticle concentration to the networks present in the initial nanoparticle layer. The larger scale network shrinks in size until a point is reached where the level of nanoparticle coverage in the second level forces nanoparticles up into a third layer. This evolution of the second layer networks with increasing nanoparticle concentration is highlighted by Figure 4.12. This shows typical AFM images of the 1.75mg/mL sample **(a)**, the 2.00mg/mL sample **(b)**, and the 2.25mg/mL sample **(c)**. All of these images show dual length scale networks present in the second nanoparticle layer, and the shrinkage of the larger of these networks is clearly displayed as the nanoparticle concentration is increased. This layer-by-layer growth process was observed for up to four layers of nanoparticles, equating to initial nanoparticle solution concentration of 4.50mg/mL.

At the centres of cells in the larger scale network of the second layer we
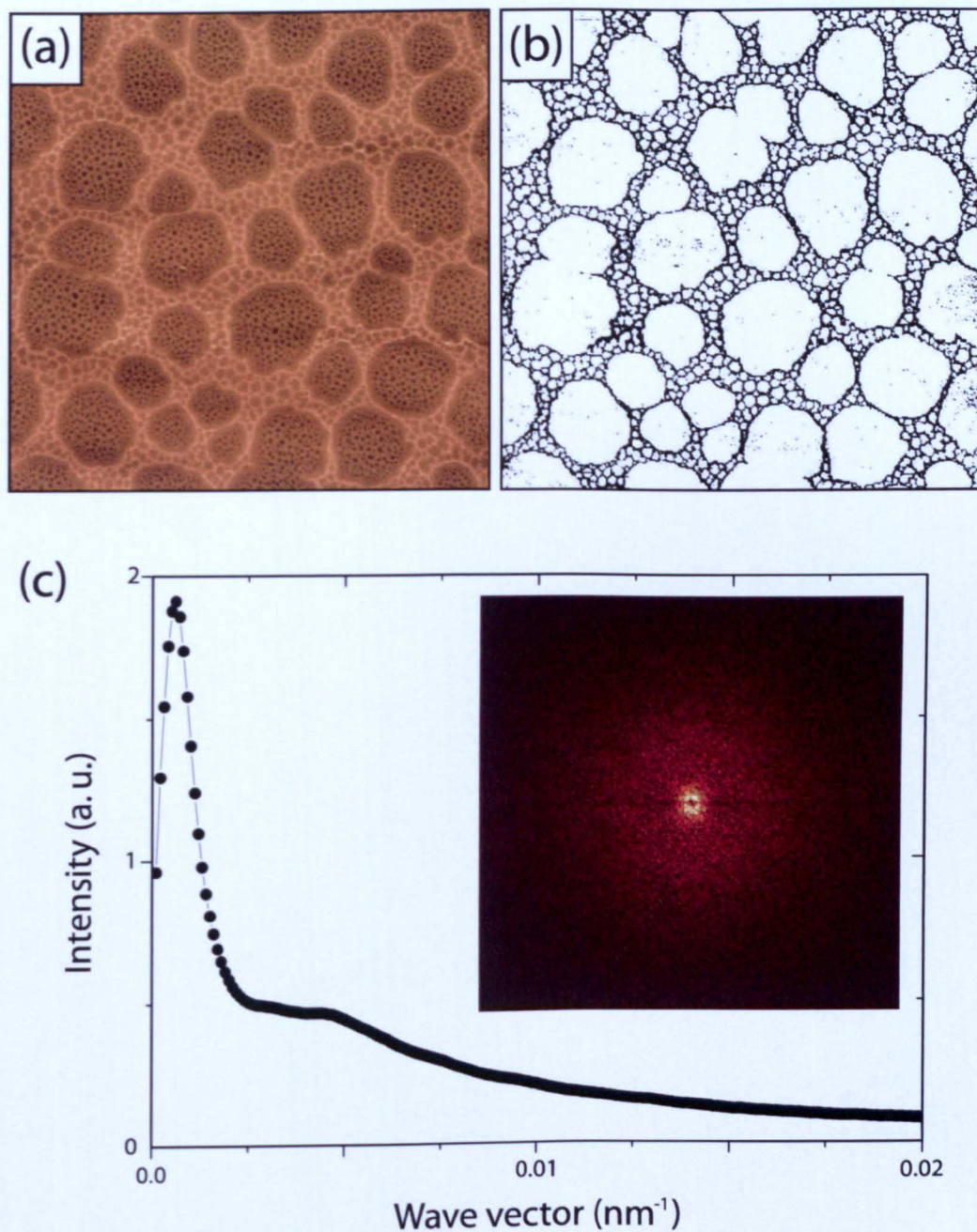
Figure 4.11: **(a)** Tapping mode AFM image of the 2.00mg/mL sample, image size $10\mu m \times 10\mu m$. **(b)** Binarised version of the image displayed in **(a)**, the threshold value for the binarisation was chosen so that only structure present in the second nanoparticle layer remains. **(c)** Radially averaged two-dimensional Fourier transform for the binary image displayed in **(b)**, the insert shows the full two-dimensional Fourier transform.
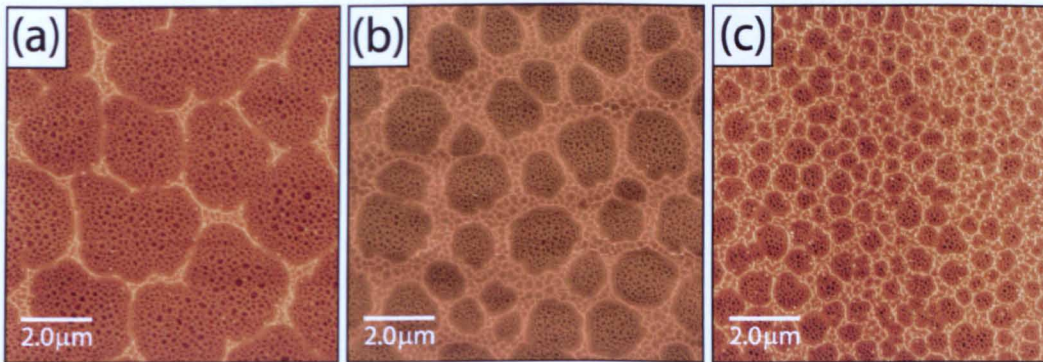
Figure 4.12: The evolution of network structures in the second layer of nanoparticles is shown for increasing nanoparticle concentration. The images are representative AFM scans of the 1.75mg/mL sample **(a)**, the 2.00mg/mL sample **(b)**, and the 2.25mg/mL sample **(c)**, all images are $10\mu m \times 10\mu m$.

have a small scale network present in the first layer of nanoparticles (see Figure 4.12 **(a)**). The striking similarities observed between the morphology of the network forming in the second layer of nanoparticles, and those that formed in the first layer for lower concentrations suggests that a similar formation mechanism is responsible.

As discussed earlier, when nanoparticle solutions are placed on native-oxide covered silicon substrates, two-dimensional aggregates form on the substrate while still under solution due to the attractions between substrate and nanoparticles. The degree of coverage of the substrate under solution will depend on the concentration of nanoparticles in the solution. Thus, as the concentration of the initial nanoparticle solution is increased we reach a point where the entire substrate is covered in dense nanoparticle film before the spin coating process is initiated. We can then think of the multiple layer network formation as an evaporative dewetting process exactly the same as that which formed the networks at lower concentrations. However, in this case, as opposed to dewetting all the way to the substrate, dewetting occurs initially down to the dense nanoparticle layer near the substrate.
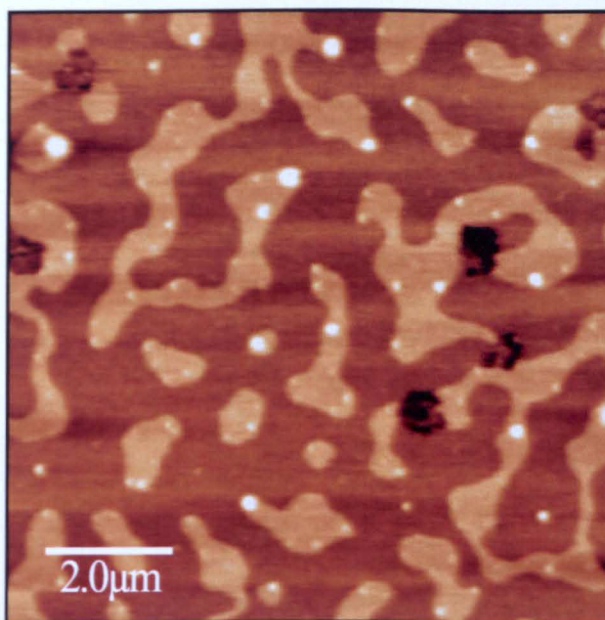
Figure 4.13: Tapping mode AFM image of a nanoparticle film spin cast from an extremely concentrated nanoparticle solution, ~20mg/mL. Image size is 10μm × 10μm, the structures in the top layer of the film are all a single nanoparticle in height.

The high density of nanoparticles in the lowest layer slows evaporation of the solvent, temporarily stabilising the film with respect to evaporative dewetting. The dual length scale network in the second layer of nanoparticles forms in the same way as such networks formed in the initial layer. Then, as the spin coating process reaches its final stages, the remaining solvent in the dense first layer evaporates and the small network in the exposed areas of first layer of nanoparticles forms. As the initial concentration of nanoparticles is increased the thickness of the layer of nanoparticles present on the surface before evaporative dewetting occurs increases until a point is reached where network formation begins in the third layer. This process simple repeats itself layer-by-layer for increasing concentration.

As more and more layers of nanoparticles are deposited the nature of the network forming in the topmost layer of nanoparticles will change. The pres-

ence of many layers will shield the nanoparticles in the top layer from their interactions with the substrate. This shielding may give nanoparticles a different level of mobility when moving on a film of other nanoparticles as compared to the silicon substrate. The effect that this has on the morphology of the topmost layer of nanoparticles can be seen in Figure 4.13, which shows a tapping mode AFM image of a nanoparticle film spin cast from an extremely concentrated nanoparticle solution ($\sim$ 20mg/mL).

4.6 Surface chemistry

Having discussed the effects of increasing the nanoparticle concentration in solution prior to spin coating we know turn our attention to effects on the network morphology caused by alterations in the chemical nature of the substrate. Changing the chemical nature of the substrate will have a direct influence on the strength of interactions between the substrate and nanoparticles. It may also affect the nanoparticle mobility and rate of solvent evaporation through changes in the surface roughness.

Figure 4.14 shows the results of a set of experiments that were almost identical to those displayed in Figure 4.6. The same nanoparticle solutions, substrate, and spin parameters were used; the only difference was that the native-oxide coated silicon samples were exposed to an oxygen plasma for five minutes before the spin coating was carried out. Contact angle measurements carried out on plasma and non-plasma cleaned bare silicon samples display a significant change in the nature of thee substrate induced by the oxygen plasma cleaning. Citing the change in the native oxide silicon substrate as a *chemical* one is slightly misleading. Exposure to the oxygen plasma does not change the chemical structure of the SiO_2 surface layer. However, the plasma
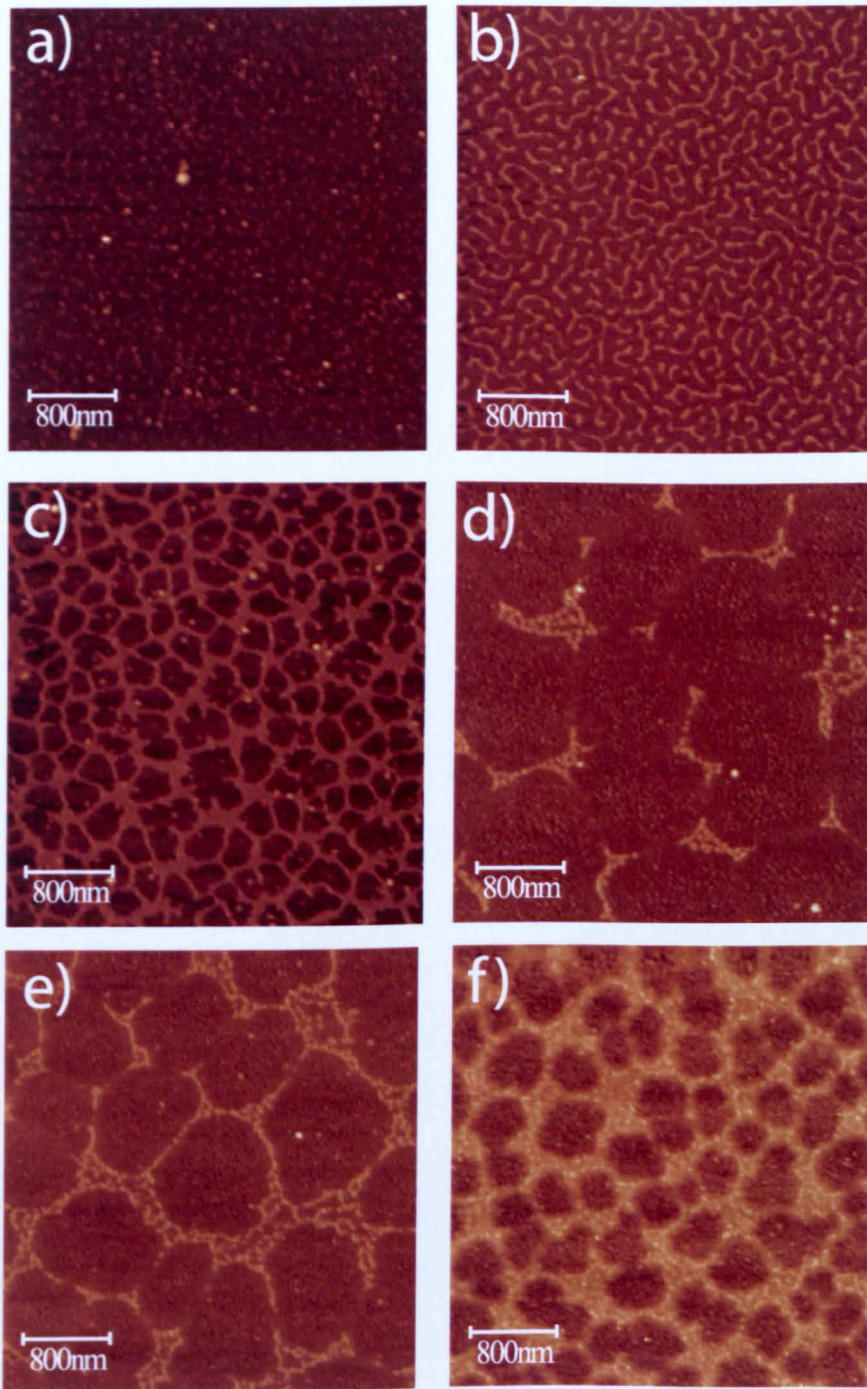
Figure 4.14: Representative AFM images of six different samples from the concentration variation experiments. All substrates are solvent washed Si(111) and exposed to an oxygen plasma at 250°C for 5 minutes. The concentrations are, **a)** 0.10mg/mL, **b)** 0.25mg/mL, **c)** 1.00mg/mL, **d)** 1.75mg/mL, **e)** 2.00mg/mL, and **f)** 2.25mg/mL. All the images are $4\mu m \times 4\mu m$.

does completely remove any organic contaminants from the substrate.

The solvent wash cleaning methods employed in the previous concentration experiments easily remove any large pieces of contaminant from the surface. However, molecularly thin layers of the solvents used in the cleaning steps may well remain on the surface, along with other contaminants that are insoluble in these particular solvents. Exposure to the highly reactive oxygen ions has the advantages of completely removing any organic material from the surface without leaving behind any contamination associated with the cleaning process.

A notable difference between the networks on plasma and non-plasma cleaned substrates is the lack of dual scale networks for concentrations which produce sub-monolayer nanoparticle films, compare Figure 4.6 **(c)** and Figure 4.14 **(c)**. The absence of dual scale networks for sub monolayer nanoparticle networks on plasma cleaned substrates has been observed on numerous other samples, Figure 4.15 gives three examples.
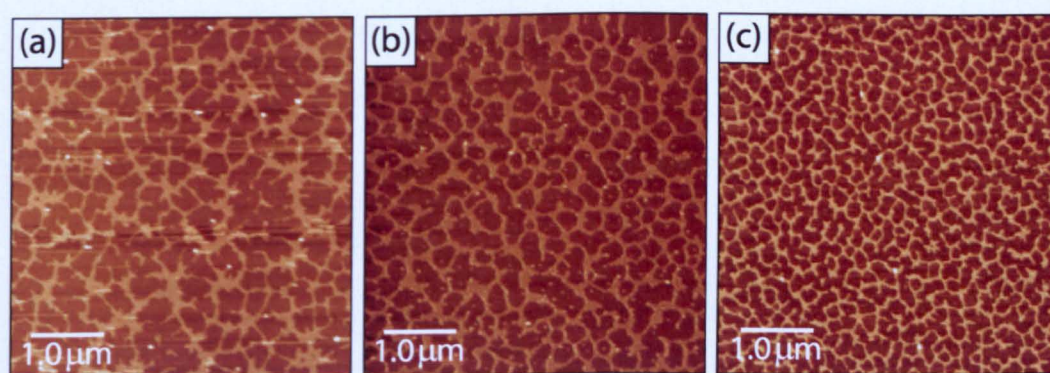

Figure 4.15: Three examples of sub-monolayer nanoparticle networks spin-cast onto plasma cleaned substrates, all the images are 5μm $\times$ 5μm.

We have explained the formation of the dual scale networks seen in Figure 4.6 **(c)** in terms of two stages in a nucleated evaporative dewetting of the surface. These processes occur over different length scales due to the increasing

likelihood of an evaporative nucleation event occurring as the spin coating process reaches its final stages.

The absence of dual scale networks on the plasma-cleaned substrates suggests another possible factor in their formation. We tentatively suggest that increased levels of contaminants present on the non-plasma cleaned substrates *may* act as nucleation points for the evaporative dewetting process. The larger scale network of the structures seen in Figure 4.6 (c) may be the result of contaminant initiated nucleation while the smaller scale network is initiated by random, thermally induced nucleation in the thinner solvent film present at later stages of spin coating.

As we would expect, the evolution of a second layer of nanoparticles with increasing concentration proceeds in the same manner as on the non-plasma cleaned substrates. Any effect on nanoparticle pattern formation caused by altering the nature of the substrate has little effect on the motion of nanoparticles in any other layer than the first. The evolution of the second, third, and fourth layers of nanoparticles, up to solution concentrations of 4.50mg/mL, remains unaltered by the substrate plasma treatment.

More radical changes in the nature of the substrate were achieved by preparing spin cast nanoparticle networks on hydrogen terminated silicon and graphite surfaces. For a more detailed description of the hydrogen termination process and the nature of the resulting surface see Chapter 5. From Figure 4.16 we can see similar structures to those observed on native-oxide covered silicon on both of these substrates. Once again we only observe structures and aggregates that are a single nanoparticle in height, suggesting that, as with native oxide coated silicon, evaporative dewetting is the predominant mechanism behind the formation of these structures.
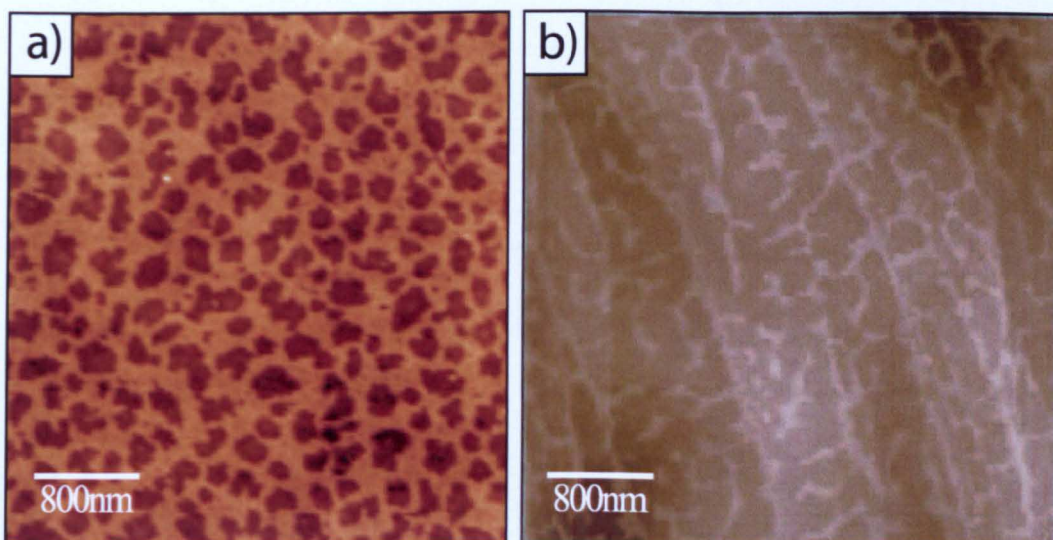
Figure 4.16: Tapping mode AFM images of spin cast nanoparticle networks on various substrates. **a)** Dodecane thiol passivated gold nanocrystal spin cast from a toluene solution onto hydrogen terminated silicon, image size $4\mu m \times 4\mu m$. **b)** Dodecane thiol passivated gold nanocrystal spin cast from a toluene solution onto a cleaved graphite surface, image size $4\mu m \times 4\mu m$.

An interesting phenoemenon is observed on the graphite substrate where the nanoparticles display a preference for aggregation at surface step edges. This aggregation of nanoparticles may well be a results of the evaporative dewetting process. As evaporative dewetting progresses the nanoparticles are dragged across the surface by the retreating solvent-substrate-air contact line. However, when this contact line reaches a step edge the nanoparticles become pinned at the step producing the elongated patterns of densely packed nanoparticles observed along step edges in figure 4.16. The use of surface features, including lithographically defined patterns, to guide the deposition of nanoparticles via evaporative dewetting will be examined in greater detail in Chapter 5.

4.7 Solvent effects

Having observed the effects of both nanoparticle concentration, and the nature of the substrate, we now turn our attention to the influence that the solvent has over network morphology. The choice of solvent will play an integral role in the pattern formation process. Most of the patterns we have observed thus far in spin coating experiments have been attributed to an evaporative dewetting mechanism.

The particular solvent properties which will have the largest effect on an evaporative dewetting process are the solvent's volatility and its dielectric constant. The volatility of the solvent will affect the rate of evaporative dewetting, and thus the length of time that any structures formed by such a process have to evolve before complete removal of the solvent stops nanoparticle motion. The solvent's dielectric constant will effect the level of interparticle interactions: solvents with higher dielectric constants will screen out the van der Waals interactions between particles.

Toluene-based dodecanethiol-passivated gold nanoparticles solutions, similar in nature to those used for the previous experiments, were allowed to dry under vacuum. Upon complete evaporation of the toluene, quantities of various organic solvents were added to the nanoparticle precipitate. The new solutions underwent a brief ultrasonic agitation, to ensure complete dissolution of the nanoparticle precipitate. Quantities of these new solutions were then spin cast onto solvent washed, native oxide coated silicon samples, using spin parameters identical to those detailed previously.

The various organic solvents used fell into three distinct groups: simple alkane chains, ranging in length from hexane to dodecane; aromatic ring based molecules (benzene, and 1,3,5-trimethylbenzene); and chlorinated compounds,

dichloromethane, and trichloromethane. A solution was also made up by re-dissolving some nanoparticle precipitate back into toluene, to check that the evaporation and re-dissolution had not adversely affected the nanoparticle integrity. The physical properties of these solvents which are relevant to the following discussion are listed in Table 4.1.

Solvent	ρ (kg/m^3)	ν (kg/m·s)	κ (J/m^3·K)	ε_r	p_v (kPa)
Hexane	660.6	300	7.76×10^{-5}	1.89	20.2
Nonane	719.2	665	7.96×10^{-5}	1.97	0.57
Dodecane	749.5	1383	7.86×10^{-5}	2.01	0.016
Benzene	876.5	604	9.26×10^{-5}	2.28	12.7
Toluene	866.8	560	8.85×10^{-5}	2.38	3.79
1,3,5-Trimethylbenzene	861.5	501	8.93×10^{-5}	2.28	0.33
Dichloromethane	1326.6	413	8.85×10^{-5}	8.89	58.2
Trichloromethane	1478.8	537	8.27×10^{-5}	4.81	26.2

Table 4.1: Physical properties of solvents, density (ρ), viscosity (ν), thermal diffusivity (κ), relative dielectric constant (ε), and vapour pressure at 25°C (p_v). All values were obtained from the CRC handbook of chemistry and physics [66]

Certain samples produced in this set of experiments displayed some unusual and previously unobserved pattern morphologies. Figure 4.17 shows AFM images of the samples spun from hexane, benzene, toluene, and 1,3,5-trimethylbenzene solutions. On the hexane, benzene, and toluene samples large scale patterns are evident which display a surprisingly high level of ordering, these patterns can be clearly seen on the toluene sample (Figure 4.17 (c)) as areas of low nanoparticle density. These patterns are distinct from the

cellular networks with two well defined correlation lengths observed in Figure 4.6 **(c)** and **(d)**. Indeed, if we study a magnification of Figure 4.17 **(c)** (Figure 4.18) we can clearly see that a two-scale cellular network is still present on the toluene sample as well as this new larger scale structure.
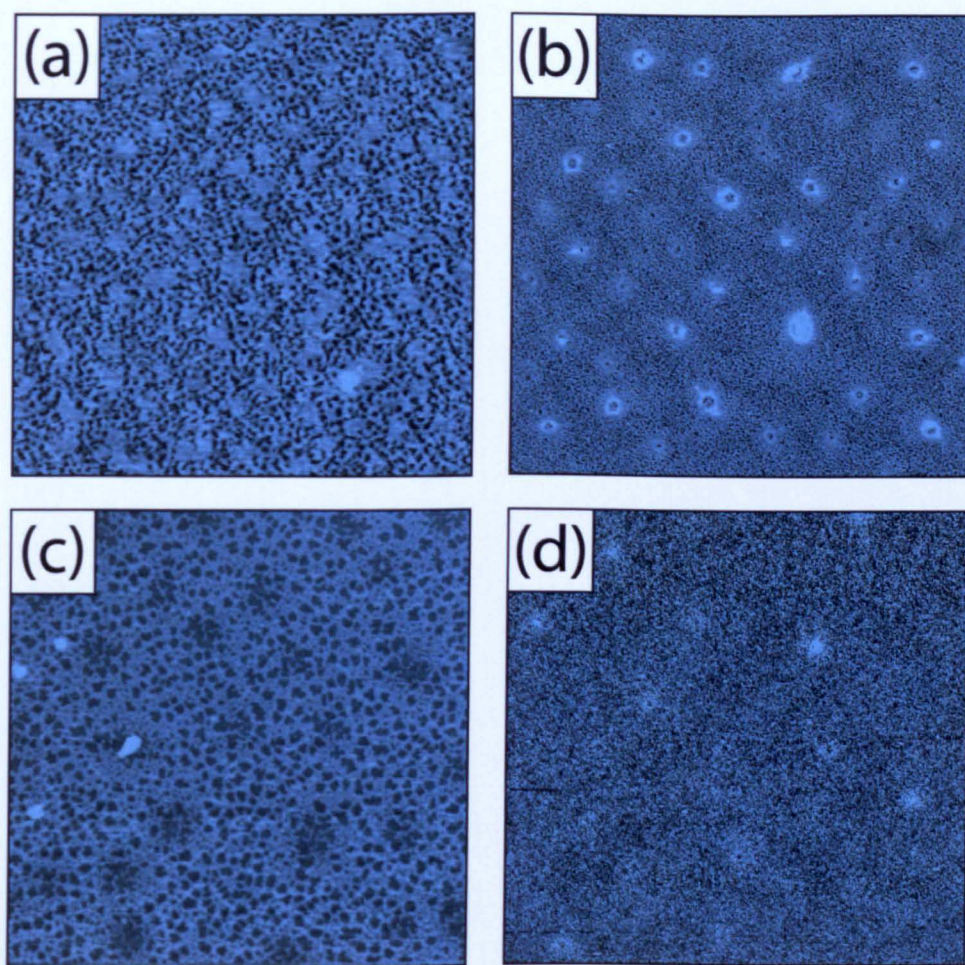

Figure 4.17: Tapping mode AFM images of spin cast nanoparticle assemblies from **(a)** hexane (2μm × 2μm), **(b)** benzene (5μm × 5μm), **(c)** toluene (5μm × 5μm) and **(d)** 1,3,5-trimethylbenzene (15μm × 15μm) solutions on native-oxide covered silicon.

In order to ascertain the correlation lengths of these new patterns the radially averaged two-dimensional Fourier transform was calculated for AFM images of the hexane, benzene, toluene, and 1,3,5-trimethylbenzene samples, Figure 4.19. At first glance there appears to be no large scale structure on
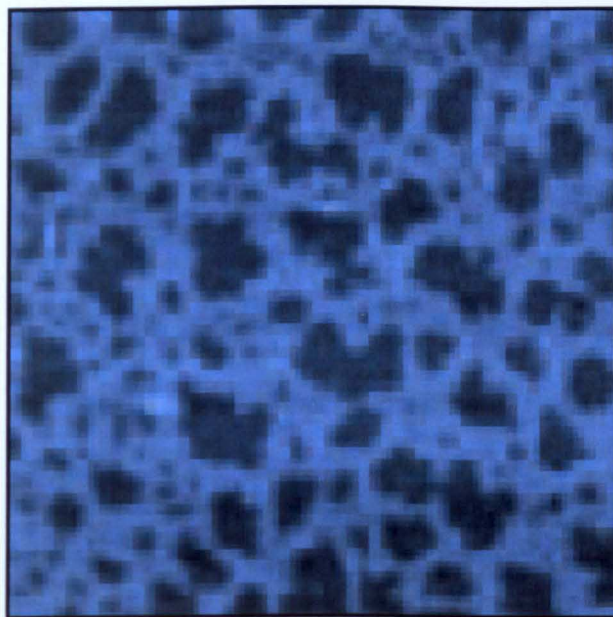
Figure 4.18: Magnification of a $1\mu m \times 1\mu m$ area of Figure 4.17 **(c)**.

the 1,3,5-trimethylbenzene sample, however, the presence of a peak in the radially averaged Fourier transform belies the presence of an ordered pattern. Similar peaks are also present in the radially averaged Fourier transforms for the hexane, benzene, and toluene samples. Figure 4.19 shows the first peak in each of the radially averaged Fourier transforms, corresponding to the largest scale ordered pattern present in the images.

The correlation lengths of the large scale structures seen in Figure 4.17 display a relationship with the vapour pressure of the solvent. Solvents with higher vapour pressures (more volatile solvents) produce patterns with smaller correlation lengths. This relationship supports the Marangoni effect as a possible mechanism for these patterns. By combining the relationships for the Marangoni number (equation 4.2) and the correlation length of patterns produced by the Marangoni effect (equation 4.4), we obtain an equation for the correlation length of a pattern formed by the Marangoni effect such that,
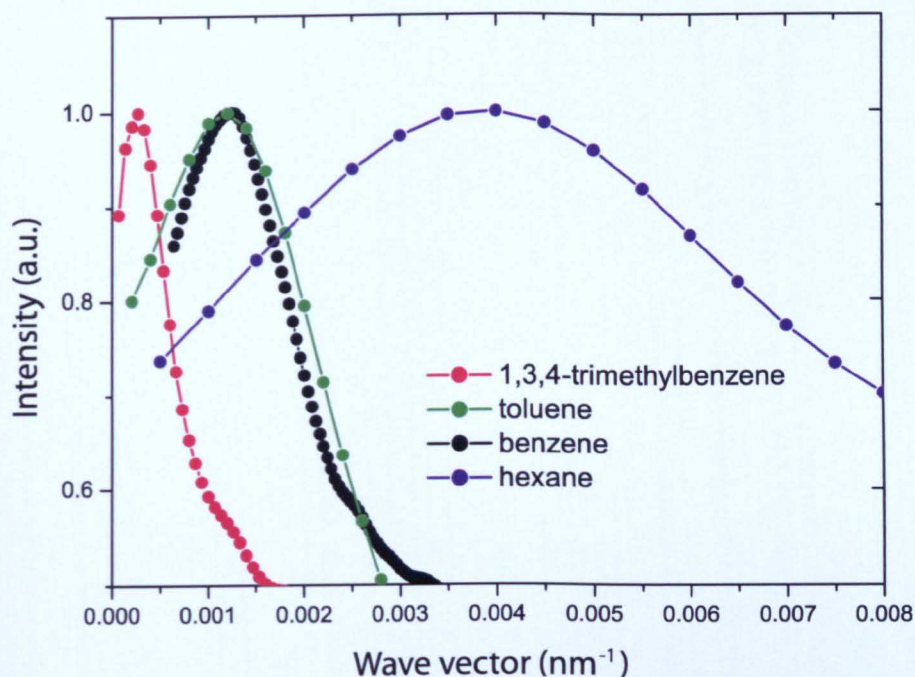
Figure 4.19: Radially averaged two-dimensional Fourier transforms for AFM images of the hexane, benzene, toluene, and 1,3,5-trimethylbenzene samples. The presence of ordered structures on each sample is highlighted by peaks in the radially averaged Fourier transform.

$$\lambda = \frac{2\pi\sqrt{8}(\rho\nu\kappa)^{1/2}h^{-3/2}}{B^{1/2}dT^{1/2}}. \tag{4.7}$$

Data concerning B, the rate of change of surface tension with temperature, is unavailable for the solvents used in these experiments, so we make the assumption that this is a constant for these solvents. As we could not measure the variation in film thickness, h, we assume that this is also constant. We then plot the experimentally measured pattern correlation lengths λ, (obtained from the peak values of the radially averaged Fourier transforms, Figure 4.19) against,

$$\frac{(\rho\nu\kappa)^{1/2}}{dT^{1/2}}. \tag{4.8}$$

A linear dependence, with an intercept at zero, is expected if the patterns are produced by the Marangoni effect. dT represents the temperature difference across the liquid film. The temperature difference across an evaporating solvent film will depend on the rate of solvent evaporation. We therefore assume that the value of dT scales linearly with the solvent vapour pressure, taken at 25°C. Based on these assumptions, Figure 4.20 shows a plot of the experimentally measured length scale against $(\rho\nu\kappa/dT)^{1/2}$ for the different nanoparticle solutions. The error in the values for the experimental correlation lengths were calculated by taking the width of the peaks in the two-dimensional Fourier transform at 95% of the peak value. All physical values were obtained from the CRC handbook of chemistry and physics [66] (see Table 4.1).
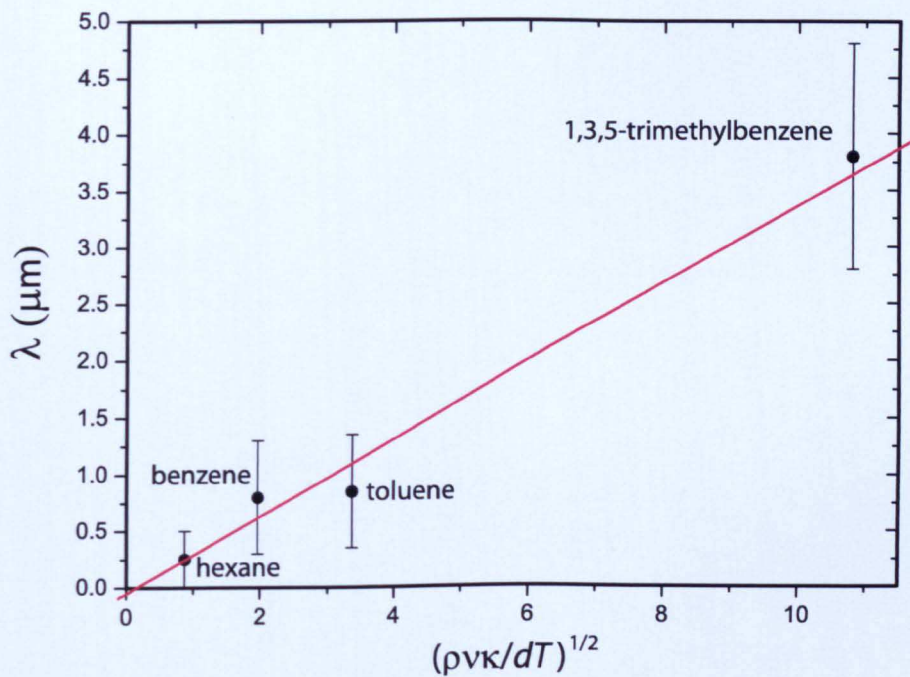
Figure 4.20: Experimentally measured pattern correlation length (λ) plotted against $(\rho\nu\kappa/dT)^{1/2}$ for hexane, benzene, toluene, and 1,3,5-trimethylbenzene nanoparticle solutions.

The data plotted in Figure 4.20 show a good agreement, within the exper-

imental error, with the linear relationship and zero value intercept expected for patterns produced via the Marangoni effect. This provides strong evidence (within, of course, our assumptions) backing the Marangoni effect as the mechanism responsible for the large scale patterns seen in Figure 4.17.

The results for networks spun from nonane and dodecane solutions displayed no such large scale patterns. The lack of such structures is easily explained for dodecane solutions. The vapour pressure at 25°C for dodecane is only 0.016kPa, twenty times lower than that of 1,3,5-trimethylbenzene at the same temperature. This significantly lower vapour pressure implies a far slower evaporation rate, signifying a lower value of dT, and thus, by equation 4.2, a lower value of the Marangoni number. This may well put the value of the Marangoni number for dodecane below the critical value of 80 required for the Marangoni effect to take place.

However, the values of vapour pressure, viscosity, density, and thermal diffusivity obtained for nonane suggest that, if the Marangoni effect is taking place, then a pattern should form with a length scale somewhere between those observed for toluene and 1,3,5-trimethylbenzene. And yet no structures are observed over this length scale in networks spun from nonane solutions, the only observed structure being an extremely small scale (<100nm) spinodal pattern. This absence is, as yet, unexplained.

These results serve to highlight the complexity of the pattern formation process. A hierarchy of patterns can be observed within a single nanoparticle film. There is strong evidence supporting an evaporative dewetting process rather than the Marangoni effect as the basis for the formation of single, and dual length scale cellular networks (figure 4.6). Whilst the Marangoni effect does appear to be responsible for the formation of larger ordered patterns

(figure 4.17). The presence of multiple pattern formation mechanisms acting within the same system means that care must be taken with the assignment of a particular mechanism to a particular structural motif. However, by careful examination of the response of a pattern's wavelength to specific variations in the experimental parameters it is possible to assign, with a reasonable degree of surety, the formation of a particular pattern to a particular process.

The dichloromethane and trichloromethane solutions provided yet another previously unobserved structural morphology, that of *isolated* nucleation events. Figure 4.21 **(a)** shows a typical AFM image of a nanoparticle network spun from a dicholromethane solution.

Figure 4.21: **(a)** Tapping mode AFM image of a typical nanoparticle network spun from a dichloromethane solution, image size 20μm $\times$ 20μm. **(b)** 3-D representation of the partial merging of two nucleation sites, image size 1.35μm $\times$ 1.35μm.

Nanoparticle networks spun from dichloromethane solutions, and to a much lesser extent the trichloromethane solutions, are ridden with circular dewetting sites. The circular character, combined with the presence of a ring of compact, high nanoparticle density network at the edges of these dewetting sites, see Figure 4.21 **(b)**, is a strong indication of a nucleation and growth mechanism.

The fact the areas of high nanoparticle density at the edges of the dewetted areas are only a single nanoparticle layer in height once again indicates an evaporative dewetting process, rather than dewetting via fluid flow. The absence of these structures from any of the networks spun from the other solvents is a reflection of the higher volatility of dichloromethane and trichloromethane. The vapour pressures of dichloromethane and trichloromethane are significantly higher than the next most volatile solvent used in these experiments, hexane. Dichloromethane's vapour pressure at 25°C is nearly four times that of hexane. The greatly increased solvent evaporation rate has two effects on the nucleated dewetting sites. Firstly, once nucleated, the dewetted areas grow at a much faster rate. This effect is demonstrated by a much larger maximum size for dewetted areas for dichloromethane as compared to the less volatile trichloromethane, or toluene, see Figure 4.6 (c). Secondly, the higher evaporation rates engender a complete evaporation of the solvent over much shorter time scales. This, in effect, freezes in the isolated nucleation sites before they have time to significantly coalesce and collide to form networks structures similar to those displayed for toluene solutions.

These results show a striking similarity to structures observed in spin coating experiments carried out by Thiele *et. al.* [64]. In these experiments the rate of evaporation of an aqueous film was controlled by varying the humidity of the atmosphere under which spin coating was performed. For high humidity, and therefore low evaporation rate, polygonal networks similar to those we observe for toluene solutions were obtained. At low humidity, *i.e.* fast evaporation, well separated nucleated dewetting patterns almost identical to those seen in figure 4.21 (a) were obtained.

A combination of the faster growth of dewetted areas and the quicker total

evaporation of the solvent is also responsible for the formation of the densely packed regions of nanoparticles at the edges of the dewetted areas. The fast outward growth of the dewetted regions quickly accumulates nanoparticles at their edges. The sudden complete evaporation of solvent then leaves no time for the accumulated nanoparticles to diffuse away from the edges of the dewetted areas, leaving a densely packed two-dimensional rim of nanoparticles, Figure 4.21 **(b)**.

Given more time to evolve we would expect the nucleated dewetting areas seen in Figure 4.21 **(a)** to form network patterns similar to those seen for toluene solutions. The much faster complete evaporation of the solvent for dichloromethane solutions means we are effectively freezing the evaporative dewetting process at an early stage.

4.8 Conclusions

In this chapter we have discussed many of the factors which control pattern formation in spin cast nanoparticle films. The spin coating of colloidal gold nanoparticles from toluene based solutions has been shown to produce a wide range of structures for different nanoparticle concentrations: from spinodal patterns to cellular networks.

Of particular interest was the formation of network structures with two distinct length scales. These structures were explained in terms of two distinct regimes in an evaporative dewetting process. With increasing nanoparticle concentration, multiple layer films of nanoparticles form in a sequential manner, each layer displaying structural morphology similar to previous layers. Again this can be attributed to evaporative dewetting processes occurring in the topmost nanoparticle/solvent layer.

The physical properties of the solvent used to create nanoparticle solutions, and its influences on nanoparticle network morphology, were studied. The use of various organic solvents for spin coating experiments provides evidence that the Marangoni effect plays an important role in pattern formation. Different stages of network formation have been observed via the control of solvent volatility. Increasing solvent evaporation rates allows the effective freezing of the network structure at earlier stages of the evaporative dewetting process.

The number of different structural motifs seen in spin cast nanoparticle networks is a testament to the complexity of the system, in terms of pattern formation. Indeed, there are several such structural motifs not covered in this work which regularly occur in spin cast nanoparticle assemblies, examples include viscous 'fingers' and dendritic branches. As we have seen, there are a plethora of different experimental variables that need to be taken into consideration for a complete understanding of the patterns which are formed. This understanding is made even more difficult by the fact that a combination of processes, rather than a single process, may be responsible for many of the patterns. Both evaporative dewetting and the Marangoni effect play crucial roles in pattern selection. Both of these mechanisms are directly influenced by variables such as the nanoparticle concentration, the substrate chemistry, the cleanliness of the substrate, and the nature of the solvent.

Chapter 5

Directing nanoparticle

self-organisation

A scanning probe-directed surface modification technique has been used to control the morphology of spin-cast nanoparticle networks. Hydrogen terminated silicon surfaces are selectively oxidised using an electrically biased AFM tip in humid conditions. Patterning of the surface with features $\sim$ 50nm in size is achieved. Nanoparticle networks on solid areas of the modified surface ($>$ $1\mu m^2$) are shown to adopt significantly altered morphologies to those on unmodified surface areas. These morphological differences are attributed to the differing physical properties of the modified surface. Monte Carlo simulations [1] substantiate these claims. The presence of solid patterns with sharp, well defined, boundaries and single lines of modified surface are shown to instigate dewetting of the nanoparticle solution film during spin coating. This effect is used to direct the morphology of nanoparticle assemblies over areas up to $10\mu m$ $\times$ $10\mu m$ in size.

5.1 Introduction

Surface modification is a commonplace technique employed in the study of wetting/dewetting characteristics of thin liquid films. By imprinting a chemical or topological structure onto a surface the behaviour of thin liquid films on that surface can be radically altered. This not only provides invaluable insights into the physics responsible for pattern evolution in such systems, but enables systematic control over the length scales and morphologies of the patterns.

There are many different surface modification techniques that have been employed to pattern surfaces as the basis for such dewetting studies. Higgins *et. al.* [67] showed that the spinodal dewetting of a thin polymer film could be made anisotropic by the use of a simple patterning technique which involved rubbing the surface prior to deposition of the polymer film. This technique produced well defined polymer lines on the surface after dewetting. Other studies have used surface patterns of self-assembled mono-layers (SAMs) that have been deposited using photolithography [68] or micro-contact printing [69].

Surface modification essentially produces patterns on the surface which consist of areas of differing topographic or chemical nature compared to the rest of the surface. As discussed in Chapter Four the stability of a thin liquid film on a surface is dependent on the thickness of the film and the functional form of the effective interface potential, $\phi(h)$. Topographic variations in the surface engender regions of varying film thickness which, in turn, may cause changes in the film's stability in these different areas. Chemical differences in the film may have the same effect by altering the form of the film's effective interface potential. Many studies have shown that liquid films selectively wet/dewet areas of a surface as a result of chemical patterning. Chemical patterning induces a preferential wetting of certain areas of the surface and this technique

115

has been used to form linear, square or hexagonal surface structures in polymer films [69, 70].

Theoretical studies of the wetting/dewetting behaviour of liquid films on topographically and chemically-patterned surfaces [71–73] have shown that a rapid rupture of a thin film can be brought about by differences in the chemical nature of the substrate. On a chemically homogeneous substrate, rupture of a covering film is induced by the amplification of thermally induced fluctuations in the surface of the film. Such *spinodal* dewetting only occurs when the excess intermolecular interaction energy per area of the film shows a positive curvature with respect to the film thickness. In this case fluid flows from thinner to thicker regions of the film eventually causing rupture. Rupture of a film, however, can be initiated on a chemically heterogeneous substrate even when the covering film is spinodally stable on *all* areas of the surface. The contrast in wettability between the chemically heterogeneous areas of the substrate creates a flow from less wettable regions towards more wettable regions. This flow can induce rupture of the film along the boundaries between these regions. This boundary induced rupture of the film induces characteristic castle-moat morphologies around heterogeneous patches on the substrate.

The majority of studies of the effects of surface modification on the dewetting of thin liquid films have concerned dewetting via the flow of liquid. No previous studies have considered the effect of surface structure on an *evaporative* dewetting process such as that detailed in Chapter Four. In the following sections the theory and experimental details of the scanning probe-induced patterning of hydrogen terminated silicon surfaces will be discussed, I shall also detail the effects of surface inhomogeneity on the morphology of spin-cast nanoparticle networks.

5.2 AFM induced oxidation of hydrogen terminated silicon

The power and versatility of scanning probe imaging techniques has made them amongst the most important analysis tools available to the modern surface scientist. Along with their unparalleled ability to study surfaces over microscopic and nanoscopic dimensions, scanning probe techniques are also capable of surface modification over similar length scales. Scanning probe techniques can be used to modify surfaces by various different methods. Two notable examples are the exploitation of the physical force exerted by the probe to scribe patterns into the surface [74], and "dip-pen" lithography, where the probe is coated with a reservoir of molecules which are subsequently deposited on the surface during scanning [75].

One of the most prevalent scanning probe surface modification techniques uses an electrically biased probe to induced the oxidation of hydrogen terminated silicon surfaces [76]. This particular scanning probe modification technique has been the subject of a large number of studies, primarily due to the immense technological importance of the silicon surface. Pure (*i.e.* atomically clean, as prepared under ultra high vacuum conditions) silicon surfaces are extremely reactive due to dangling bonds present on the silicon surface atoms. Under ambient conditions this high reactivity results in the formation of a *native* oxide layer on the silicon surface.

In many cases, hydrogen passivation of the silicon surface is more desirable than an oxide layer. Such a hydrogen passivation (also know as hydrogen termination) can, for example, be obtained by the deposition of molecular hydrogen onto a clean silicon surface under UHV conditions. It is possible,

however, to obtain atomically flat hydrogen passivated surfaces via a much simpler wet chemical process [77,78]. This process involves the removal of the silicon's native oxide layer by dissolution in an aqueous solution of ammonium fluoride (NH_4F). In addition to removing the oxide layer this solution also provides the hydrogen passivation of the surface.

Left under ambient conditions the hydrogen passivated surface will re-oxidise. Figures 5.1 **(a)** through **(f)** show a step-by-step example of this oxidation process. The oxidation is self limiting, in that once an initial layer of oxide has formed, for more oxide to grow oxygen ions must diffuse from the surface across the already present oxide layer. This diffusion barrier limits the growth of oxide under ambient conditions to ~ 0.7nm.

When an electrically biased AFM probe is brought into close proximity to the surface, the strong electric field present at the probe's apex provides a driving force for diffusion of oxygen ions across the growing oxide layer. This driving force can promote growth of oxide layers up to 8nm in thickness [76, 79]. There are many factors which will affect both the thickness of the oxide layer and the lateral dimensions of the features produced by this method. These factors include the quality of the initial silicon surface passivation; the magnitude of the electrical bias between tip and surface; the speed at which the probe scans across the surface; and the quantity of water adsorbed on the surface (essentially the humidity of the atmosphere in which the process is carried out).

The original process pioneered by Dagata *et. al.* [76] used an STM probe, but the method was later expanded to conductive AFM probes in a non-contact process. Adsorbed water on the substrate forms a *water bridge* between the AFM probe and the surface [80]. It is the water contained within this bridge
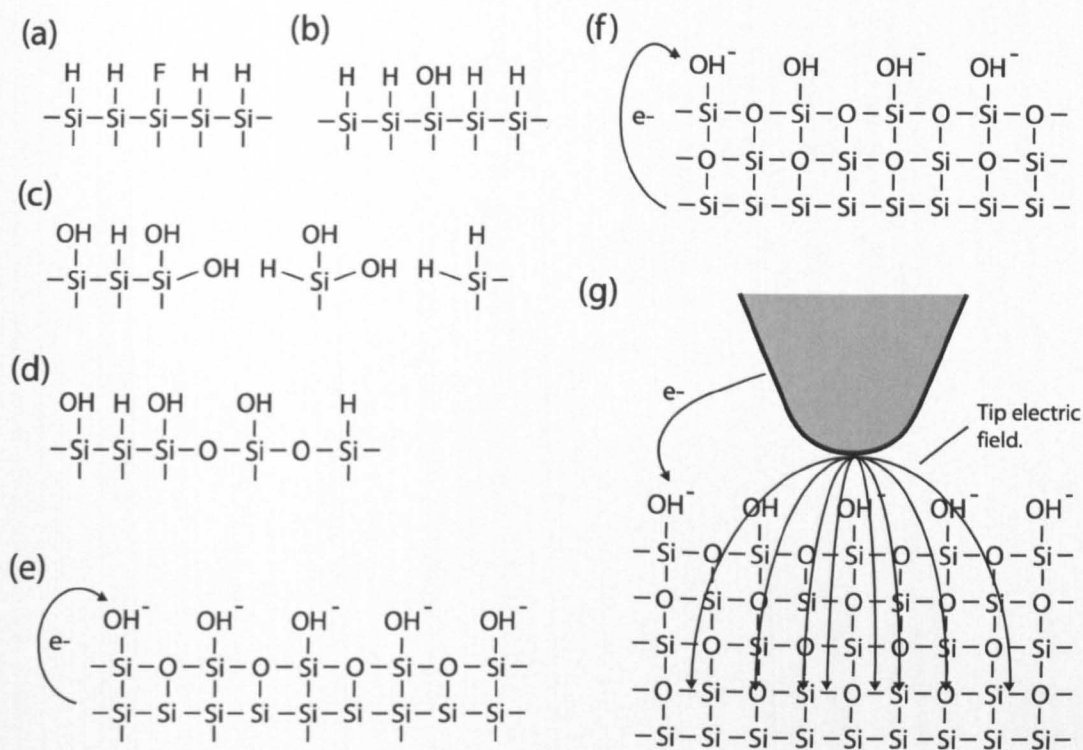
Figure 5.1: **(a)** After hydrogen passivation the silicon surface is primarily saturated with Si-H bonds with a few Si-F defects. **(b)** F atoms at the surface are quickly replaced by OH$^-$ ions from water present in the atmosphere. The replacement of H also occurs but at a slower rate. **(c)** The high electronegativity of the OH$^-$ group causes polarisation of the Si-OH$^-$ bond; this polarisation in turn induces a polarisation of Si-Si bonds in the initial Si surface layer allowing water to attack this bond. **(d)** An initial layer of oxide forms on the surface. **(e)** and **(f)** Electrons from the Si conduction band can tunnel through the oxide layer into adsorbed species on the surface resulting in ionic oxygen species. In addition, a charge double layer exists at the interface between the Si and the SiO$_x$ due to differences in electronegativity, this double layer produces an electric field which promotes diffusion of oxygen ions across the growing film. Oxide layers of 0.7nm in thickness can grow by this process before the increasing diffusion/tunnel barrier presented by this oxide layer curtails any further growth. **(g)** When an electrically-biased AFM probe is brought close to the surface two factors contribute to increased oxidation; electrons no longer have to tunnel through the oxide layer to create oxygen ions on the surface, they can come directly from the tip; the enhanced field at the probe's apex promotes diffusion of the oxygen ions through the growing oxide layer. (After Ref. [79].)

119

between the tip and the surface which provides the oxygen ions (OH^- and O^-) required for the oxidation process. The presence of the water bridge also sets the resolution limits for structures fabricated by this process. The extremely high dielectric constant of the water bridge compared to the surrounding air, 81 compared to 1, makes the water bridge act as an effective "lens" for the electric field of the tip. The field, and therefore the oxidation process, is thus confined to an area of the same diameter as the neck of the water bridge connecting the tip and the surface [80]. Some control over the size of the water bridge can be gained by changing the tip-surface distance and structures with dimensions as small as 10nm have been achieved using this method.

5.3 Experimental details

The substrates used in these experiments were $1cm^2$ Si(111) samples with a ~2nm native oxide surface layer. These samples were ultrasonically washed in standard solvents and then exposed to an oxygen plasma at 250^oC for 5 minutes to ensure complete removal of any organic surface contamination. These samples were then immersed in a 4:1 solution of sulphuric acid and hydrogen peroxide (H_2SO_4 and H_2O_2) for 10 minutes at 100^oC. This solution promotes the growth of a smooth surface layer of oxide essential to produce a defect-free hydrogen passivated surface. This step was followed by a 30 second immersion in a 10% aqueous hydro fluoric acid (HF) solution and a subsequent 30 second immersion in a 40 % aqueous ammonium fluoride (NH_4F) solution. Between each individual step the samples were washed with ultra-pure water and blow dried with nitrogen. Figure 5.2 shows a typical example of a hydrogen passivated surface obtained via this method where the RMS roughness of the surface is 0.20nm $\pm$ 0.05nm.
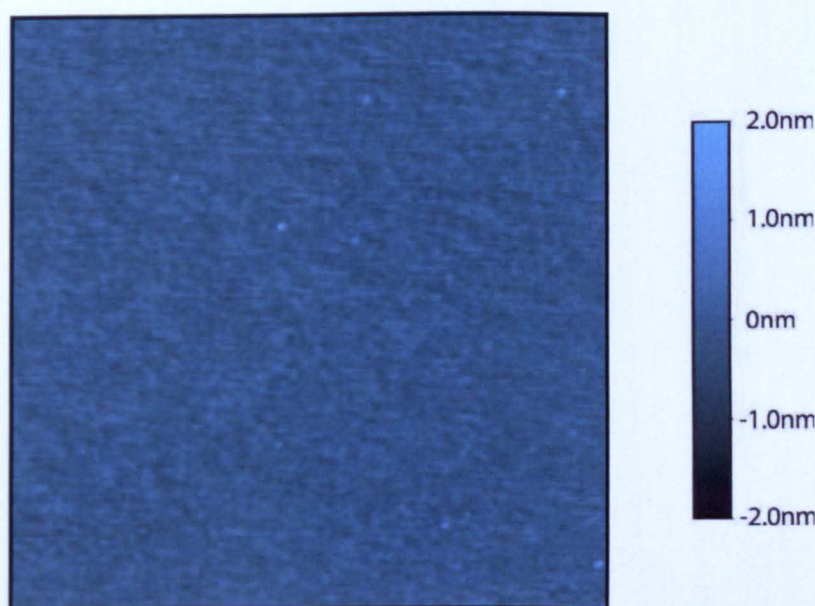
Figure 5.2: Tapping mode AFM image of a typical hydrogen passivated surface obtained by wet chemical methods, image size is 2μm $\times$ 2μm.

Following hydrogen passivation, gold contact pads were deposited on the surface. These pads act as markers allowing relocation of oxide patterns for AFM imaging after nanoparticle deposition. The samples were then mounted on glass slides ready to be placed into the AFM. All imaging and scanning probe lithography was carried out using an Asylum Research MFP-3D atomic force microscope. The AFM apparatus is contained within a sealed acoustic cabinet to which humidity control equipment was added. This allowed stable control of the relative humidity inside the cabinet over the range 40%-80%. AFM cantilevers with a PtIr coating were used for all the lithography performed in this study. The electrically-contacted sample was connected to ground while the tip was biased at voltages in the range 0V-10V. The dedicated lithographic software for the MFP-3D system allows any pattern of lines to be drawn by the tip, providing the lithographic process with a high level of versatility.

121

After the AFM lithographic steps, the samples were immediately removed to a clean room were quantities of toluene-based dodecane thiol passivated gold nanoparticle solutions were spin cast onto the sample surfaces. The samples were then once more placed in the AFM apparatus and the marker pads used to relocate the oxide patterns.

5.4   Results and discussion

Figure 5.3 (a) shows an example of the level of detail possible with the AFM lithographic technique. The grid displayed in Figure 5.3 (a) is $1\mu m^2$ in size and comprises oxide lines which are $\sim$2nm in height and $\sim$50nm wide.
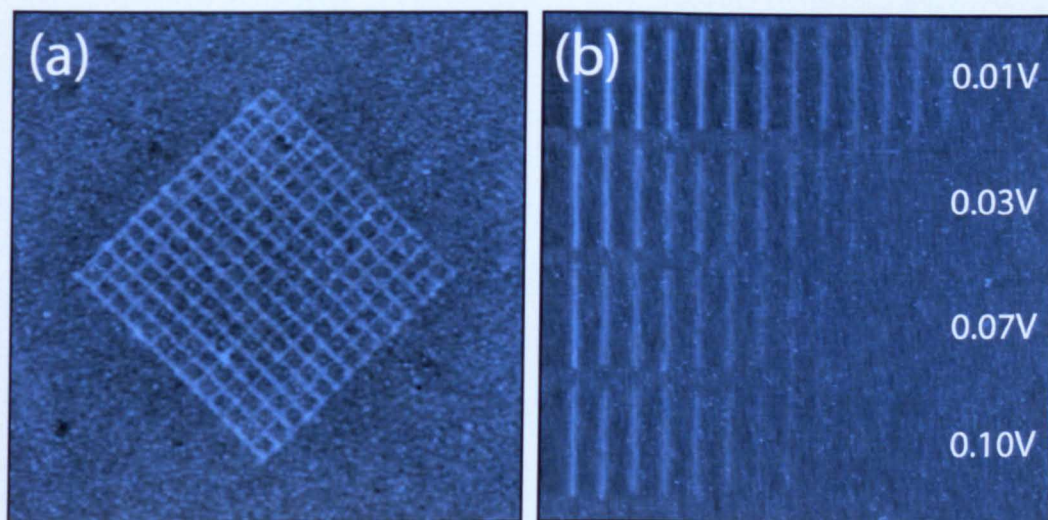
Figure 5.3: **(a)** Oxide grid pattern on a hydrogen passivated silicon surface. **(b)** The effect of the set point and tip bias on the width and height of the oxide lines. Each set of oxide lines was written at a different set point value (0.01V, 0.03V, 0.07V, and 0.10V). Within each set of the lines the tip bias voltage is varied between 10V and 3V in 0.5V steps from left to right. Scan speed and relative humidity were kept constant at $0.5\mu m$ s^{-1} and 70% respectively.

Control over both the width and the height of the oxide lines was obtained by variation of the AFM parameters used during the lithographic process, most notably the set point, scan speed, and tip bias voltage. With slow scan

speeds the tip spends longer over each part of the line being drawn, thus the width and the thickness of the oxide layer are increased. Higher tip bias voltages have much the same effect, promoting growth of thicker and wider oxide lines. Increasing the set point reduces both the thickness and the width of oxide lines. Examples of these effects can be seen in Figure 5.3 **(b)**. Control over the width and thickness of the oxide layer obtained by these methods is qualitative at best. The oxidation process is strongly dependent on the quality of the hydrogen passivated surface, which showed distinct variations from sample to sample.

Solid blocks of oxidised surface were fabricated by scanning the AFM probe in a tightly spaced raster pattern during lithography. Following this, nanoparticle solutions were spin cast onto the surface and the samples subsequently re-imaged. The result of one such experiment is shown in Figure 5.4 **(a)**. From Figure 5.4 **(a)** we can clearly see that the nanoparticle network adopts different morphologies on and off the oxidised area. Off the oxidised area the nanoparticle network is a small scale "spinodal-like" pattern, while on the oxidised area the network is larger in scale and cellular in nature. It is also interesting to note that the nanoparticle network is *continuous* across the boundary of the oxide pattern.

One possibility which has been suggested [81] is that the difference in morphology of nanoparticle networks on and off the oxide pattern is linked to the thermal properties of the respective surfaces. The thermal conductivities of Si and SiO$_2$ are 0.015 W·mK^{-1}, and 1.4W·mK^{-1} respectively [66]. Therefore, the SiO$_2$ surface conducts much more heat away from the nanoparticle solution during the spin coating process slowing down the evaporation of solvent. A similar effect may also arise from changes in the surface roughness. For the
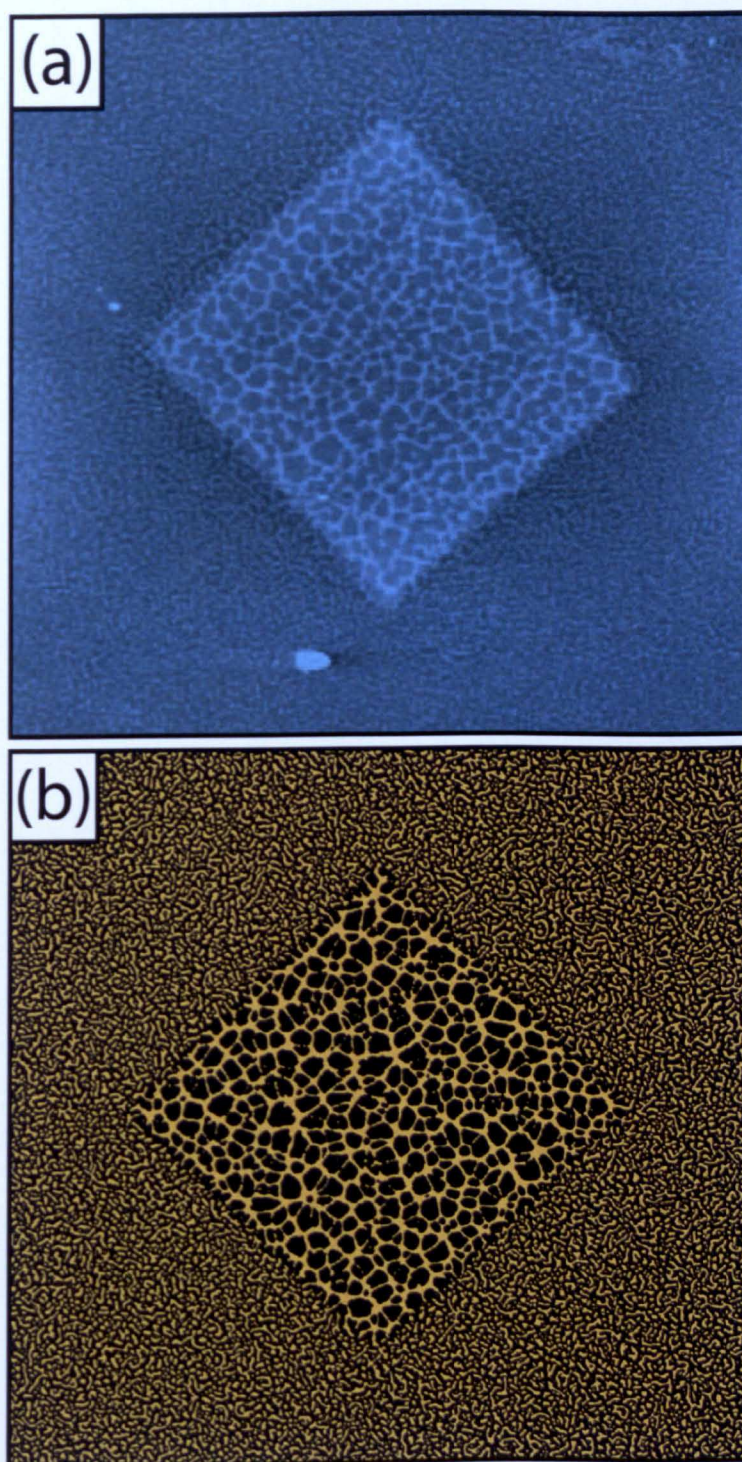
123

Figure 5.4: **(a)** Tapping mode AFM image of a nanoparticle network spin cast on top of a solid square oxide pattern, the oxide square is $\sim 4\mu m \times 4\mu m$. **(b)** Results of Monte carlo simulation for the evaporative dewetting of nanoparticle solution on a patterned substrate

124

oxide pattern displayed in Figure 5.4 (a) the RMS roughness on the pattern is 1.135nm, while on the hydrogen passivated surface the RMS roughness is 0.227nm. A similar trend was displayed for all of the oxide patterns which were produced. The increased surface roughness acts to slow the evaporation of solvent. Given these two contributing factors it seems likely that it is a slower solvent evaporation rate which is responsible for the differences in morphology.

To test this hypothesis, Monte Carlo simulations of the evaporative dewetting of a nanoparticle solution on a patterned surface were carried out [82]. These simulations were based on the metropolis algorithm method devised by Rabani *et. al.* [1,52]. To account for the patterned areas of the substrate two extra terms were added to the Hamiltonian used in the simulation. The original Hamiltonian used by Rabani *et. al.* for a homogeneous surface is given by,

$$H = -\varepsilon_l \sum_{<ij>} l_i l_j - \varepsilon_n \sum_{<ij>} n_i n_j - \varepsilon_{nl} \sum_{<ij>} n_i l_j - \mu_l \sum_i l_i, \qquad (5.1)$$

where ε_l, ε_n, and ε_{nl} represent the interaction strengths between two liquid lattice sites, two nanoparticle lattice sites, and a liquid and nanoparticle lattice site respectively, and μ is the chemical potential. To this Hamiltonian two terms were added which model the interaction with the surface for liquid and nanoparticle lattice sites:

$$-\varepsilon_{sl}(i) \sum_i l_i - \varepsilon_{sn}(i) \sum_i n_i, \qquad (5.2)$$

where ε_{sl} and ε_{sn} are the interaction strengths between a liquid lattice site and the surface and a nanoparticle lattice site and the surface. In order to model the square oxide pattern seen in Figure 5.4 (a) a simulation was performed on

a surface with a $4\mu m^2$ central square on which the values of ε_{sl} and ε_{sn} were twice as large as for the rest of the surface. The boundaries of the oxide pattern shown in Figure 5.4 **(a)** are not absolutely sharp: they have a finite width. In order to represent this in the simulated surface the values of ε_{sl} and ε_{sn} change smoothly between their *"on square"* and *"off square"* values over a distance of 100nm at the square's boundaries. The result of this simulation is shown in Figure 5.4 **(b)**. The similarities between this result and the experimental image displayed in Figure 5.4 **(a)** are striking. The factor of two difference between the surface interaction energies on and off patterned areas in the simulation is perhaps not as large as might initially be expected given the factor of 100 difference between the thermal conductivities of Si and SiO_2. The thermal conductivity values, however, are those for bulk materials. The oxide pattern in Figure 5.4 **(a)** is ∼2nm thick, as such we would expect a value for the thermal conductivity of the oxide pattern to be somewhere between that of bulk Si and bulk SiO_2.

By taking line sections through the nanoparticle network we see that the network both on and off the oxide pattern is only ever one nanoparticle layer in height. As discussed in Chapter 4 this suggests that dewetting occurs via an evaporative route rather than by fluid flow. This hypothesis is backed up by the ability of an evaporative dewetting simulation to accurately reproduce experimentally observed patterns.

As mentioned previously, the nanoparticle network appears continuous across the boundary of the oxide pattern in Figure 5.4 **(a)**, indicating that dewetting does not preferentially occur at the boundary. Preferential dewetting at the boundary of oxide patterns was however observed in similar experiments and some of these results are displayed in Figure 5.6. For both of

the oxide patterns displayed in Figure 5.5 it is obvious that dewetting has occurred preferentially at the edges of the patterned areas, indicated by the nanoparticle free area around the perimeter of the oxide patterns. That all of the nanoparticle structures seen in Figure 5.5 are still only a single nanoparticle in height suggests that this preferential dewetting at the pattern boundary arises from solvent evaporation.
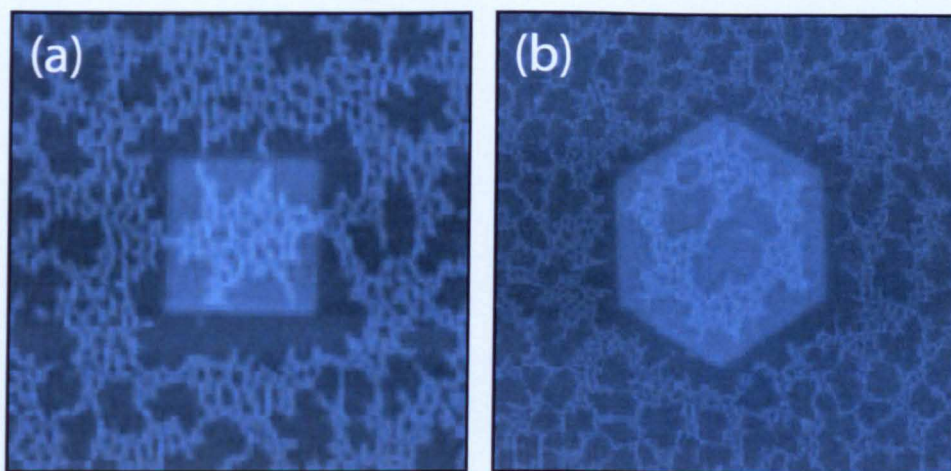

Figure 5.5: Tapping mode images showing nanoparticle networks which have been spin cast on top of oxide patterns. Preferential dewetting of the solvent has occurred at the oxide pattern boundary in both images, indicated by the nanoparticle free areas around the pattern perimeter. Image sizes are **(a)** 3μm × 3μm and **(b)** 4μm × 4μm .

The presence of preferential dewetting occurring at the oxide pattern boundary is directly linked to the *sharpness of the boundary*. This sharpness shows a good deal of variation from sample to sample due to variations in the quality of the surface termination. The sharpness of the boundary can be quantified by direct measurement of the width of the boundary region between the hydrogen passivated surface and the oxide pattern.

Figure 5.6 **(a)** and **(b)** show magnifications of small sections of the oxide pattern boundary from Figure 5.4 **(a)** and Figure 5.5 **(b)** respectively. Below these images are line sections taken through the oxide pattern boundary. The

red line on each image shows the position of these line sections within the images. The extent of the boundary region on each line section is marked by the *i)* and *ii)* tags. The position of these tags was calculated by measuring the average height of the substrate and oxide pattern over an entire line section. The width of the boundary was then taken as the lateral distance over which the height of the line section changed between these two values. From multiple line sections taken over different sections of the boundary of the oxide pattern displayed in Figure 5.4 **(a)** the boundary width is 170nm ± 20nm, while, for the oxide pattern displayed in Figure 5.5 **(b)**, the width is 60nm ± 20nm.
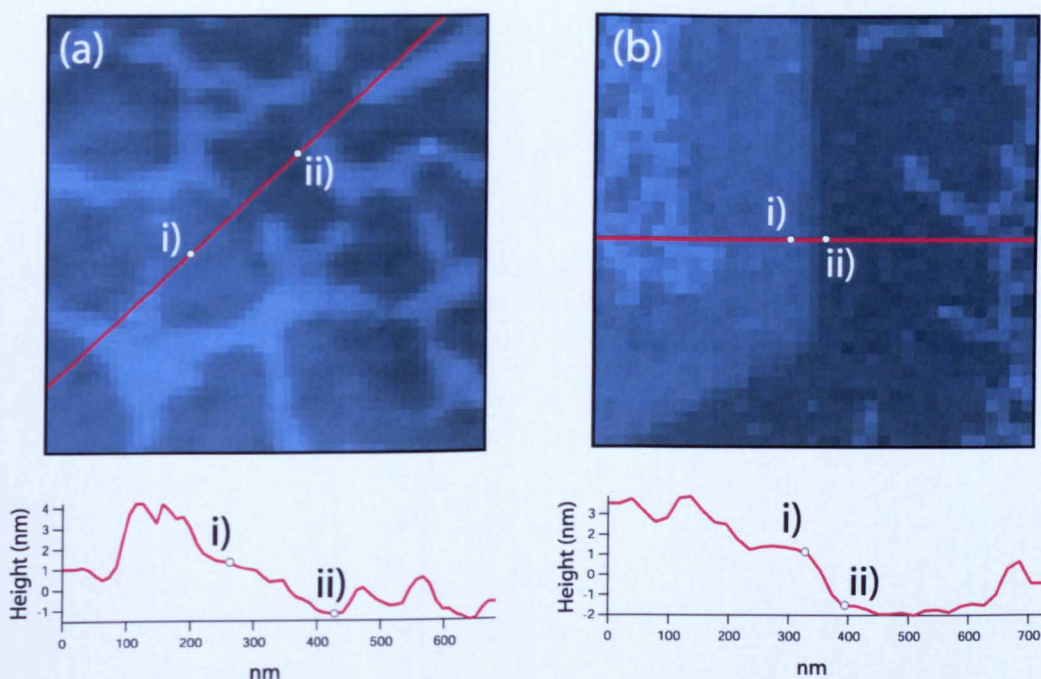
Figure 5.6: **(a)** Magnification of the boundary region of the oxide pattern displayed in Figure 5.4. **(b)** Magnification of the boundary regions of the oxide pattern displayed in Figure 5.5 **(b)**. Underneath each image line sections, taken along the red lines marked on the images, are shown.

This relationship between boundary width and preferential edge dewetting is reproduced for all of the solid oxide patterns studied. Preferential dewetting of the nanoparticle solution at pattern boundaries only occurs on oxide

patterns with edge widths <100nm. Karagupta and Sharma [71–73] predicted that preferential dewetting may occur at the boundaries of chemically heterogeneous surface structures. The difference in wettability between the different surface regions induces a flow of liquid from the less wettable area towards the more wettable areas. In the oxide patterns studied here there is, however, not only a change in the surface chemistry on and off the pattern, but also a topographic change because the oxide patterns are ∼2.5nm higher than the surrounding surface. During the spin-coating process, on patterns with sharp boundaries the steep increase in height of the surface induces a large curvature of the covering nanoparticle/solvent film at the pattern boundary. This curvature may increase the solvent evaporation at these points instigating the preferential *evaporative* dewetting at these points. These dewetted areas then grow outwards forming the nanoparticle free regions at the pattern perimeter.
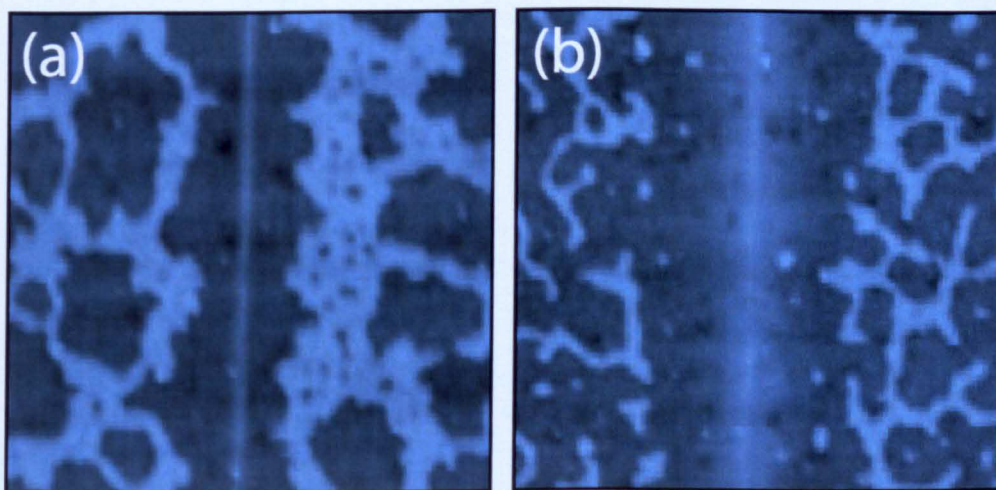
Figure 5.7: The preferential dewetting of nanoparticle solution from oxide lines. (a) Oxide line drawn with tip bias of 10V, set point 0.03V, scan speed 500nm s^{-1}, and humidity 70%. (b) Oxide line drawn with tip bias of 10V, set point 0.01V, scan speed 250nm s^{-1}, and humidity 70%. Images are both 1.5μm × 1.5μm.

This preferential dewetting at sharp interfaces between patterned and non-patterned areas provides a method by which control over the morphology of

129

spin cast nanoparticle networks can be obtained. The AFM lithography technique is used to pattern individual oxide lines that are as sharp as possible. The sharp change in the surface topography induces dewetting of the nanoparticle solution along these lines of oxide. This method can be used to control the dewetting of the nanoparticle film during spin coating, and thus control the overall morphology of the final nanoparticle network. Examples of this technique are shown in Figure 5.7 where the two oxide lines shown in Figure 5.7 (a) and (b) have been lithographically patterned with different set point and scan speed values. By decreasing the set point and the scan speed value during lithography the oxide line in Figure 5.7 (b) has been made significantly thinner in comparison to the one shown in Figure 5.7 (a). Preferential dewetting along the oxide lines is observed in both cases. Even though the oxide line in Figure 5.7 (b) is ~500nm wide the sharp apex at the center of the line is still enough to induce preferential dewetting of the nanoparticle solution during spin coating.

The ability to form sharp oxide lines to instigate the controlled dewetting of the nanoparticle solution during the spin coating process opens up the ability to exert a high degree of control over the morphology of the nanoparticle networks. By careful selection of oxide patterns nanoparticles may be *corralled* into predefined patterns which possess fixed correlation lengths. Examples of this technique are displayed in Figure 5.8, where hexagonal and square arrays of open oxide circles were lithographically patterned onto the surface prior to nanoparticle deposition. Dewetting of the nanoparticle solution is preferentially instigated along the rims of the oxide circles. This preferential dewetting forces the nanoparticle network into a morphology with the same symmetry and characteristic length scale as the original oxide pattern.
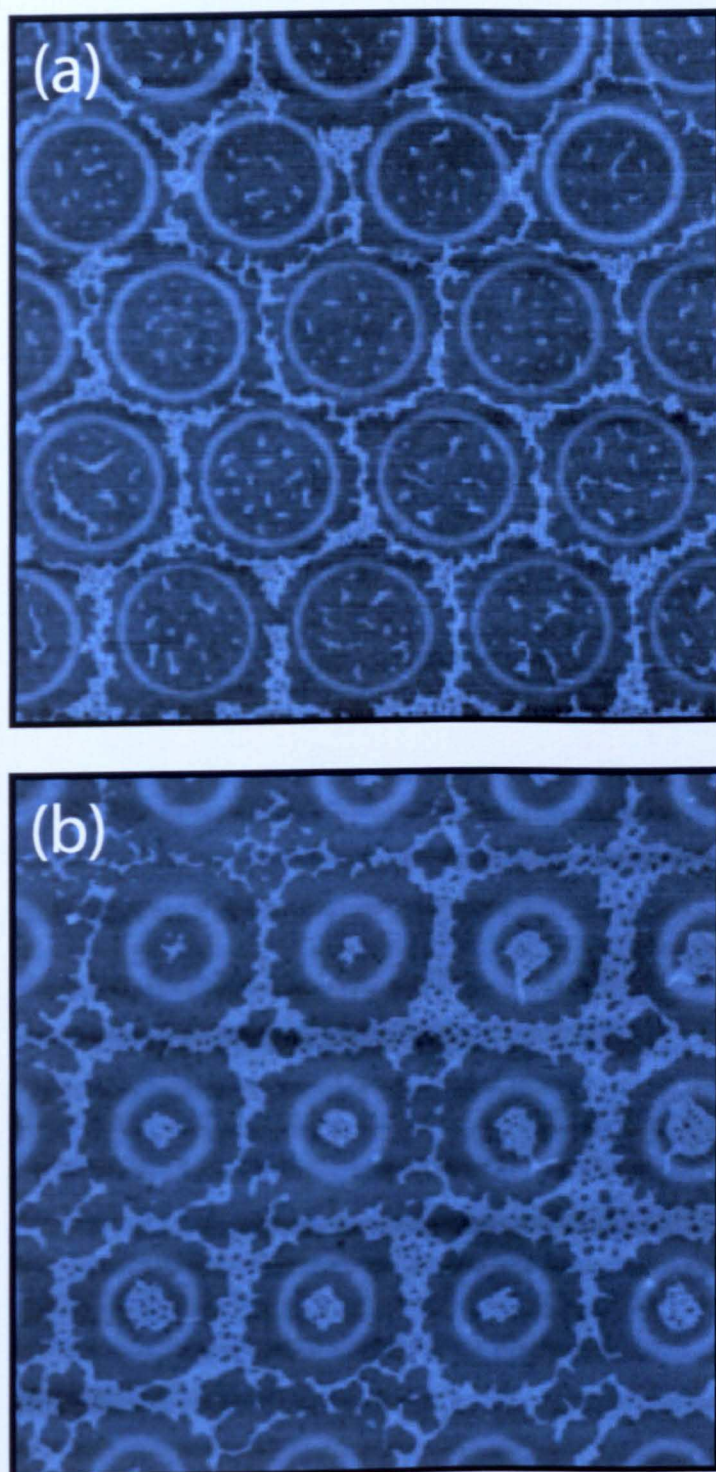
Figure 5.8: Tapping mode AFM images of spin cast nanoparticle networks were the overall morphology of the network has been controlled by the lithographic patterning of oxide lines prior to nanoparticle deposition, the images are both $8\mu m^2$.

5.5 Conclusions

Scanning probe lithography and surface modification offer one of the most intriguing routes towards the manufacture of surface structures designed over the nanometric and micrometric size ranges. The unprecedented control and accuracy that such techniques provide open a vast array of possibilities, both for the direct manipulation of surface material and for the subsequent control over surface coatings such as thin liquid films.

We have employed wet chemical methods to hydrogen passivate silicon surfaces which were then selectively oxidised using an electrically biased AFM probe. Using this method the fabrication of oxide lines ~50nm wide and ~2-3nm high was possible. Control over the oxide line height and thickness was obtained via the parameters used during lithography: most notable the tip bias voltage, the scan speed, and the set point value. Scanning the AFM probe in tightly spaced raster patterns during the lithographic process produces surface patterns consisting of solid blocks of oxide. Colloidal nanoparticle solutions were spin cast on top of these oxide patterns in order to observe how their presence affects nanoparticle network morphology.

The morphology of the nanoparticle networks displayed distinct differences on the patterned oxide areas compared to the rest of the surface. Networks on the patterned areas were larger in scale, and in some cases of different morphological types, *i.e* cellular vs spinodal. These differences are attributed to the different thermal and physical properties of the surface areas. The thermal conductivity of SiO_2 is two orders of magnitude greater than that of Si, this slows the evaporation of solvent on the oxide patterns during spin coating. The RMS roughness of the lithographically patterned oxide areas is also significantly higher than for the rest of the hydrogen passivated surface. The

increased roughness also acts to slow the evaporation of solvent. This slower evaporation of solvent is responsible for the different nanoparticle network morphologies observed on the patterned surfaces.

Monte Carlo simulations were used to test this hypothesis [82]. The patterned nature of the surfaces detailed in the experiments was represented in these simulations by the introduction of surface interaction terms to the simulation Hamiltonian. The surface interaction terms varied for different areas of the surface in order to represent the experimental oxide patterns. Excellent agreement between the experimental images and the simulation results were obtained.

A preferential dewetting effect was observed after the spin casting of nanoparticle solutions onto some patterned surfaces. This preferential dewetting of the nanoparticle solution from the boundaries of some oxide patterns produced a nanoparticle free region in the final nanoparticle network located at the pattern perimeter. The fact that thus effect was present for some oxide patterns and not others is linked to the sharpness of the oxide pattern boundary. The boundary of solid oxide patterns was shown to display a great deal of variation depending on the passivated surface and on the tip used for the lithographic steps. The preferential dewetting was only observed on oxide patterns with the sharpest boundaries. The mechanism responsible for this preferential dewetting is still not clear, with both chemical and topological differences between the oxide patterns and the rest of the surface being possible causes. This preferential dewetting of nanoparticle solutions from sharp oxide boundaries during spin coating was utilised for the direct control of nanoparticle network morphology. Oxide line patterns consisting of open circles were used to force the formation of nanoparticle arrays possessing both predefined

length scales and symmetries.

Chapter 6

Coerced coarsening in nanoparticle networks

We present experimental results which show the coarsening of nanoparticle networks induced by the interaction with an AFM probe. Sub-monolayer assemblies of thiol passivated gold nanoparticles spin cast onto silicon substrates from an alkane solvent are shown to coarsen under repetitive scanning by an atomic force microscope probe. This mechanical coarsening process displays dynamics and scaling behaviour which are distinct from that of coarsening in thermally driven systems.

6.1 Introduction

Coarsening, the evolution of a far-from-equilibrium system towards its ground state, is a ubiquitous phenomenon which influences the structure and behaviour of countless systems in nature [83–85]. Such far-from-equilibrium structures are, for example, formed during phase separation. In Chapter 2 we used as an example the mixing/demixing of a binary liquid. Following a quench of

the system from a point where the mixed state is stable, to a point where the unmixed state is stable the system phase separates by either nucleation and growth or spinodal decomposition, depending on the relative volume fractions of the liquid components and the depth of the quench. Once phase separation has occurred the structures which are formed continue to grow in size (coarsen) over time. The driving force behind this growth stems from the free energy cost associated with the presence of interfaces between the two phases, coarsening occurs as the system strives to minimise this interfacial area.

Despite distinct differences in the physicochemical properties of the many systems in which this type of structural evolution is observed, the coarsening process exhibits a fundamental, unifying feature: the morphology at a given point in time can be characterised by a single length scale, $L(t)$, which evolves according to a power law,

$$L(t) \propto t^{\gamma}. \tag{6.1}$$

The evolution of the system therefore occurs via a set of self-similar morphologies, which, while being associated with different correlation lengths, are statistically identical under an appropriate scaling. This self-similar evolution is the basis for the *dynamic scaling hypothesis* which suggests that in the late stages of phase separation the only important length scale of the system is the average domain size. An important implication of this hypothesis is that any statistical characterisation of the structure taken at time t can be expressed in the form of a universal function of a single reduced variable. For example the two point correlation function, $G(r,t)$, may be expressed in term of the reduced length scale x, such that,

$$G(r, t) = G(x) \quad where \quad x = \frac{r}{L(t)}. \tag{6.2}$$

Therefore, to predict the coarsened structure at any point in its evolution we need only have knowledge of the scaled pattern which it adopts and the value of the growth exponent γ. Both the form of the scaled pattern and the value adopted by the growth exponent are related to the physical process by which the system approaches equilibrium. For the coarsening of two-dimensional non-equilibrium structures, such as the spin cast nanoparticle networks studied here, two primary types of mechanism are observed: Ostwald ripening and dynamic cluster diffusion. Although giving rise to significantly different dynamics and, thus, morphologies, both of these processes have been studied and cited as the mechanism responsible for thermally activated coarsening in two-dimensional systems.

As we have seen in Chapter 4, and numerous other studies, self-organisation in colloidal nanoparticle systems gives rise to a panoply of intricate patterns spanning labyrinthine structures [9, 52], cellular networks [1, 11, 52], wormlike aggregates [9, 11, 52], and large domains of perfectly ordered arrays [53, 55]. Observation of the dynamics of coarsening in such systems has previously been limited to "quench-and-observe" techniques [52]. In that work the coarsening of PbSe nanoparticle clusters on graphite under an octane solvent was studied. Coarsening was allowed to proceed for a fixed length of time before exposure to the atmosphere promoted rapid solvent evaporation, effectively fixing the nanoparticle clusters in place to allow imaging.

The current study incorporates, to my knowledge, not only the first real time study of the coarsening dynamics of nanoparticle assemblies but also the first instance of mechanically-activated coarsening. In the standard well stud-

ied case of thermally activated coarsening, the reduction in interface length, and thus free energy, is brought about by the random thermal motion of particles. In the current study this activation comes from the mechanical interaction between the AFM tip and the nanoparticle assembly. In this novel, scanning probe coerced approach to equilibrium many of the signatures of conventional, thermal coarsening are reproduced. As such we will now present a more detailed discussion of Ostwald ripening and dynamic cluster diffusion-coalescence before going on to detail the results of the coerced coarsening experiments, and how they are linked to these coarsening mechanisms.

6.2 Ostwald ripening

Introduced qualitatively by Ostwald at the beginning of the 20th century [86], Ostwald ripening was later given a more complete mathematical treatment by Lifshitz and Slyosov [87]. The basis for this coarsening mechanism is that clusters remain immobile, surrounded by a gas of monomers. Growth occurs by evaporation and condensation of monomers to and from clusters. Larger cluster grow at the expense of smaller clusters thereby reducing the interfacial free energy associated with the system. The basis for this biased exchange of monomers from smaller to larger clusters is the size dependent nature of the chemical potential. In three-dimensions the Gibbs-Thomson equation relates the chemical potential of the background gas of monomers μ_{eq}, to the chemical potential μ_R of a cluster of radius R such that,

$$\frac{\mu_R}{\mu_{eq}} = exp\left(\frac{R_c}{R}\right) \quad where \quad R_c = \frac{2\sigma V_{mono}}{k_b T} \tag{6.3}$$

Combining these two equations gives

$$\mu_R = \mu_{eq} \left(1 + \frac{2\sigma V_{mono}}{R k_b T} \right) , \tag{6.4}$$

where R_c is the critical cluster radius, σ is the surface tension, and V_{mono} is the volume occupied by a single monomer. These equations are directly transferable into two-dimensions. The chemical potential of the background gas of monomers is defined by the critical cluster radius (R_c). Clusters with radii greater than this critical value have a lower chemical potential than the background so there is a net flow into the cluster, therefore they grow, clusters smaller than the critical radius have a higher chemical potential than the background and thus they shrink. The value of the growth scaling exponent γ depends on the rate limiting step of the Ostwald ripening process. If the rate limiting step is the evaporation/condensation of monomers to and from clusters then $\gamma = 1/2$, if however the rate limiting step is the diffusion of monomers across the surface then $\gamma = 1/3$.

It is not only the value of γ, but also the functional form of the scale invariant cluster size distribution $F(R/R_c)$ vs R/R_c, that depends on the rate limiting step of the Ostwald process. If the evaporation-condensation of the monomers to and from the clusters is the limiting step then the scale invariant size distribution may be modelled by the following equation (Figure 6.1),

$$F(R_s) = \begin{cases} \frac{R_s}{2} \left(\frac{2}{2-R_s} \right)^4 exp \left(\frac{-2R_s}{2-R_s} \right) & if \quad R_s < 2 \\ \\ 0 & if \quad R_s > 2 \end{cases} , \tag{6.5}$$

where $R_s = R/R_c$. If however the rate limiting step is the diffusion of monomers across the surface then the scale invariant cluster size distribution is given by (Figure 6.1),

$$F(R_s) = \begin{cases} \dfrac{CR_s^2 exp\left(\frac{-1}{\frac{3}{2}-R_s}\right)}{\left(\frac{3}{2}-R_s\right)^{28/9}(3+R_s)^{17/9}} & if \quad R_s < \frac{3}{2} \\ \\ 0 & if \quad R_s > \frac{3}{2}, \end{cases} \tag{6.6}$$

where C is a constant of normalisation.

6.3 Dynamic coalescence

The Ostwald ripening process is dependent on the assumption that clusters are immobile and that they can only grow or shrink via the exchange of monomers with an encompassing monomer gas. If, however, we incorporate the possibility of diffusion and irreversible coalescence of clusters upon their collision, then changes in the value of γ and, more significantly, drastic changes in the functional form of the scale invariant cluster size distribution are observed.

Diffusion and coalescence of clusters can be modelled using the set of Smoluchowski equations [88, 89],

$$\frac{dn_k}{dt} = \frac{1}{2}\sum_{i+j=k} K_{ij}n_i n_j - nk\sum_{j=1}^{\infty} K_{jk}n_j, \tag{6.7}$$

where n_j is the number of clusters of size j, and t corresponds to time. K_{ij} is a kernel which describes the rate at which two clusters of size i and j meet to form a single cluster of size $i + j$. For Brownian motion of clusters in two-dimensions the kernel is given by $K_{ij} = 2\pi(D_i + D_j)$, where D_i and D_j are the diffusion coefficients for clusters of size i and size j [89]. Equation 6.7 essentially models the rate of change of clusters of size k. The first term of equation 6.7 models the formation of clusters of size k by the coalescence of cluster of size i and size j (where $i+j = k$). The second term models the

removal of clusters of size k by their coalescence with clusters of all other sizes.

In order to find a solution to the Smoluchowski equations the cluster diffusion coefficient is required. By assuming that the diffusion coefficient for a cluster scales with the clusters size N such that,

$$D_N \propto N^{-\alpha}, \tag{6.8}$$

then the mean cluster radius $\overline{R}$ is shown to scale with time as

$$\overline{R} \propto t^\gamma \quad where \quad \gamma = \frac{1}{d(\alpha + 1)} \tag{6.9}$$

Here d is the dimensionality of the system [90]. One can also show that the scale invariant size invariant size distribution is given by,

$$F(R_s) = \frac{dW(WR_s)^{d(\alpha+1-1/d)}}{\Gamma(\alpha+1)} exp(-1WR_s)^d$$

$$\tag{6.10}$$

$$where \quad W = \Gamma(\alpha + 1 + 1/d)/\Gamma(\alpha + 1) \quad and \quad R_s = R/\overline{R}.$$

Thus, the value of a single parameter, α, controls every aspect of coarsening via cluster diffusion-coalescence mechanisms. The value that α adopts depends on the mechanism by which cluster diffusion takes place and there are three distinct mechanisms that have been suggested, periphery diffusion [91], terrace diffusion [92, 93], and evaporation-condensation diffusion [94].

For periphery diffusion, where a cluster's center of mass moves by rearrangement of monomers at the edges of the cluster, $\alpha = 3/2$, giving a growth exponent of $\gamma = 1/5$. For terrace diffusion, motion of a cluster's center of mass occurs due to the *correlated* evaporation and condensation of monomers from

the cluster's edge with $\alpha = 1$ and $\gamma = 1/4$. For evaporation-condensation diffusion, where a cluster's center of mass moves by the *uncorrelated* evaporation and condensation of monomers from the cluster's edge, $\alpha = 1/2$ and $\gamma = 1/3$.

It is important to note that the same value of growth exponent ($\gamma = 1/3$) is expected for certain instances of both Ostwald ripening dominated coarsening and diffusion-coalescence coarsening. The functional form of the scale invariant size distribution, however, shows a far stronger dependence on the coarsening mechanism. A simple examination of growth exponents for a system undergoing coarsening is therefore often not sufficient to unambiguously identify the responsible mechanism, the value of γ needs to be corroborated by observation of the functional form of the normalised cluster size distribution.

Figure 6.1 shows the functional forms of the scale invariant island size distribution functions for Ostwald ripening in both the diffusion and detachment limited cases, and for diffusion-coalescence coarsening derived from the Smoluchowski equation. The differences in functional form of the distributions between Ostwald ripening and coalescence coarsening are very distinct. Ostwald ripening processes display a sharp cut-off at high values of normalised size and a long tail towards lower values, while for diffusion coalescence the reverse is true, with a long tail toward higher values of the normalised size.

6.4 Coerced coarsening

6.4.1 Experimental details

The nanoparticles used in this study were gold particles with a ~2nm core and a passivating layer of octane-thiol capping ligands, synthesised via the method outlined by Brust *et. al.* [6]. The initial solutions from the syn-
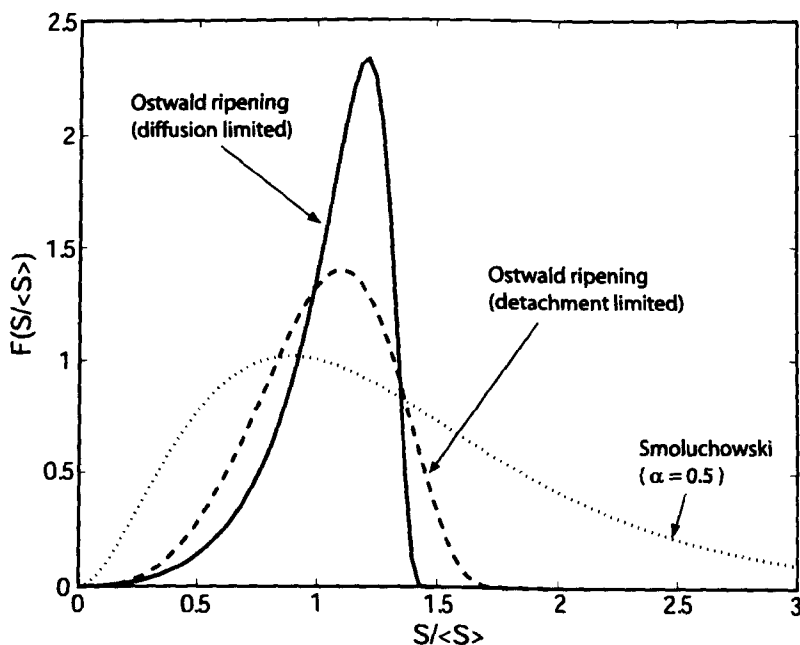
Figure 6.1: Theoretical normalised size distributions $F(S/\langle S\rangle)$ *vs* $S/\langle S\rangle$, shown for Ostwald ripening (diffusion and detachment limited) and cluster diffusion-coalescence derived from Smoluchowski equation with $\alpha = 0.5$.

thesis procedure consisting of nanoparticles in a toluene solvent were allowed to dry under vacuum until complete removal of the toluene solvent had occurred. The dry nanoparticle precipitate was subsequently redissolved into a nonane solvent. Previous studies within this group have shown no significant nanoparticle degradation caused by multiple drying and redissolving steps of this kind. After a brief ultrasonic agitation, to ensure complete dissolution of the nanoparticle precipitate, $\sim 25\mu L$ of solution was spin cast onto 1cm^2 Si(111) samples which had been ultrasonically cleaned in standard solvent washes.

The concentration of the nanoparticle solution was chosen qualitatively to produce various levels of sub-monolayer nanoparticle coverage. Samples were then immediately transferred to the AFM apparatus inside an enclosed acoustic cabinet. After a brief period to allow for thermal stabilisation of the sample and AFM, scanning of the sample was performed using an Asylum

research MFP3D atomic force microscope. The majority of the coarsening experiments were performed with AC240 AFM cantilevers (resonant frequency $\sim$70kHz and spring constant $\sim$2Nm^{-1}) except one experimental run performed using an appreciably stiffer AC160 cantilever (resonant frequency $\sim$300kHz and spring constant $\sim$42Nm^{-1}). Sample areas of 2 μm^2 were imaged repeatedly until image degradation, probably due to tip damage, stopped each individual experimental run.

6.4.2 Results

The concentration of nanoparticle solution used in the spin coating process during sample fabrication controlled the fractional area coverage of the nanoparticle assemblies formed. This fractional area coverage subsequently determined the morphology that the nanoparticle assemblies adopted during the mechanically induced coarsening. Fractional area coverages of $\sim$ 0.3-0.35 produced assemblies of isolated nanoparticle clusters, whereas coverages of $\sim$ 0.55 produced interconnected labyrinthine structures. The coarsening of these two morphologies displayed markedly different dynamics.

6.4.3 Interconnected structures

Figure 6.2 shows tapping mode AFM images taken at evenly spaced points throughout an experimental run. The raw experimental images were taken over a 2μm^2 area, however to remove the adverse effect of residual drift during the imaging process this was reduced to 1μm^2 for the analysis steps to ensure that exactly the same area of network was studied. The coverage of nanoparticles remains constant at $\sim$0.55ML throughout the experimental run, *i.e.* the quantity of nanoparticles is conserved throughout the coarsening process.
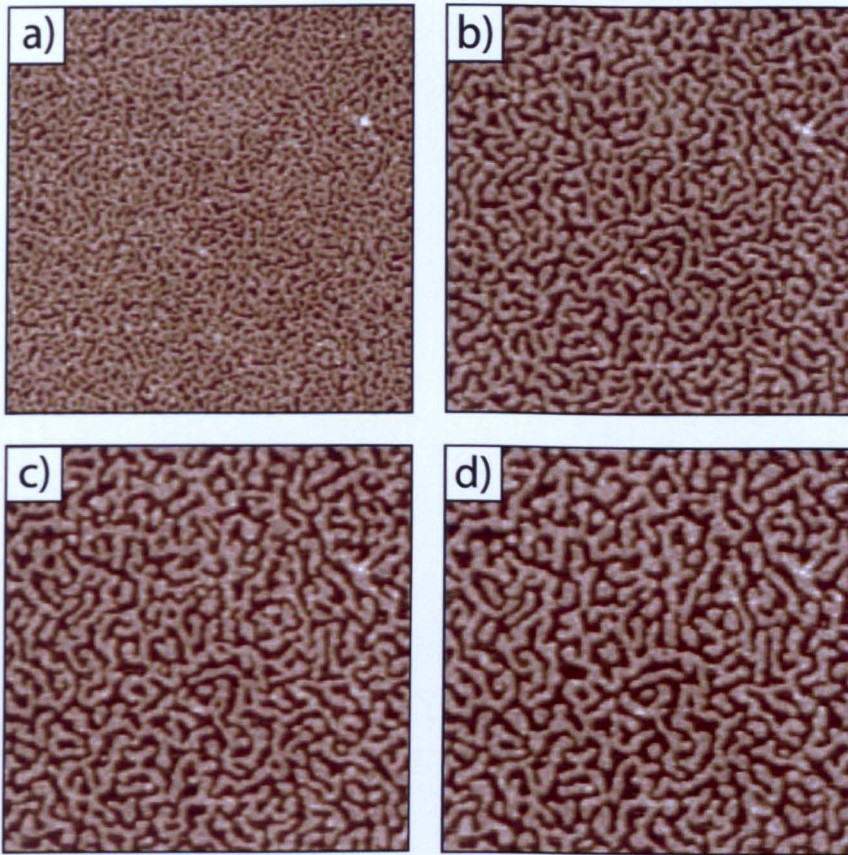
Figure 6.2: Coerced coarsening evolution of an interconnected nanoparticle assembly. All images are 1μm $\times$ 1μm. Images are taken from evenly spaced points throughout the experimental run, (a) 1st scan, (b) 15th scan, (c) 30th scan, and (d) 45th scan. The fractional area coverage of nanoparticles remains constant at approximately 0.55ML throughout the experimental run.

From a cursory visual analysis of these images the morphology of the network appears to be coarsening in a self-similar fashion, suggesting that the dynamic scaling hypothesis holds. It has been shown in previous studies that for dynamic scaling to hold the evolution of the structure factor (*i.e.* the radially averaged fourier transform) of the system, $S(t)$, following an initial transient period, should be of the form [83, 95, 96]

$$S(k, t) = k_{max}(t)^{-2} F(k/k_{max}(t)), \tag{6.11}$$

where k_{max} is the peak position of the structure factor and $F(k/k_{max}(t))$ is a time independent master function. To test the validity of the dynamic scaling hypothesis for this data we calculated the radially averaged fourier transform for each image of the experimental run. Upon normalisation the radially averaged fourier transforms collapse onto a single master curve, Figure 6.3.
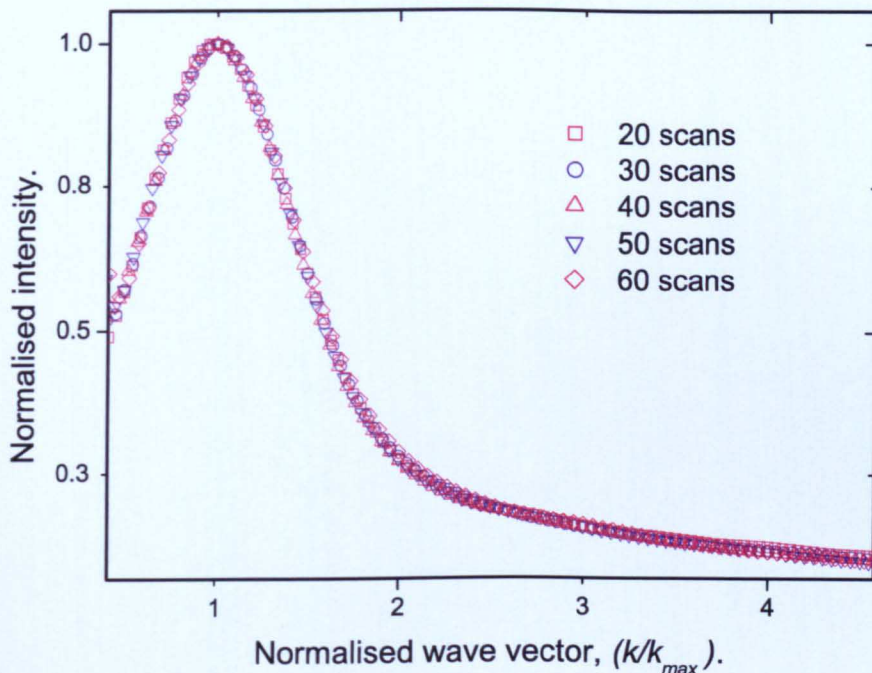
Figure 6.3: Normalised radially averaged 2D-FFT plotted for a range of images throughout the experimental run depicted in Figure 6.2.

The almost perfect collapse of the radially averaged Fourier transform onto a single master curve for the majority of the experimental run displays the remarkably extent to which dynamic scaling holds for the coerced coarsening of nanoparticle assemblies with interconnected morphologies.

That the system evolution which we observe in Figure 6.2 is not simply due to a natural - *i.e.* solely thermally activated - coarsening is clear from Figure 6.4. This Figure shows the boundary between a continuously scanned surface region and the surrounding region which has been scanned only once to obtain

this image. The boundary is seamless, and the morphology of the unscanned region remains the same as the morphology we observed in the first scan of the experimental run, Figure 6.2 **(a)**.
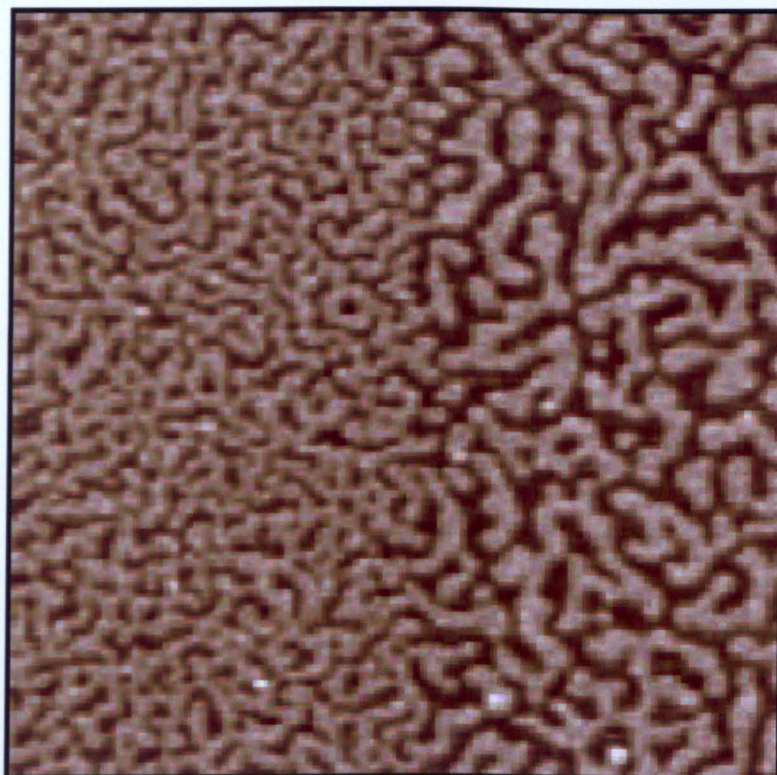
Figure 6.4: $1\mu m^2$ tapping mode AFM image of the edge of the continuously scanned region. Image was collected after the termination of the experimental run detailed in Figure 6.2.

The probe-induced dynamics we observe here are noteworthy from a number of perspectives. Although scanning-probe-induced sample modification is now commonplace, the coarsening effect illustrated in Figure 6.2 is significantly more subtle than the processes commonly used to restructure surfaces at the sub-micron and nanometre levels. That the evolution of such a system, driven mechanically towards equilibrium, retains such a degree of self similarity throughout that evolution implies that a morphology with a given length scale may be produced by simply stopping the imaging process at an appropriate

point. In addition, the quality of imaging remains high despite the significant level of probe-induced material transport, with only infrequent streaking in the images betraying the presence of material transfer.

The fact that coarsening is solely due to the scanning process allows us to calculate a value of the growth exponent for this coerced coarsening process by making an analogy between the time a system has been allowed to evolve (in a standard coarsening process) and the number of scans performed in our coerced coarsening experiment. As a measure of the characteristic length scale we use the peak value of the radially averaged fourier transform. Figure 6.5 displays the peak value of the radially averaged Fourier transform plotted against scan number on a log-log scale.
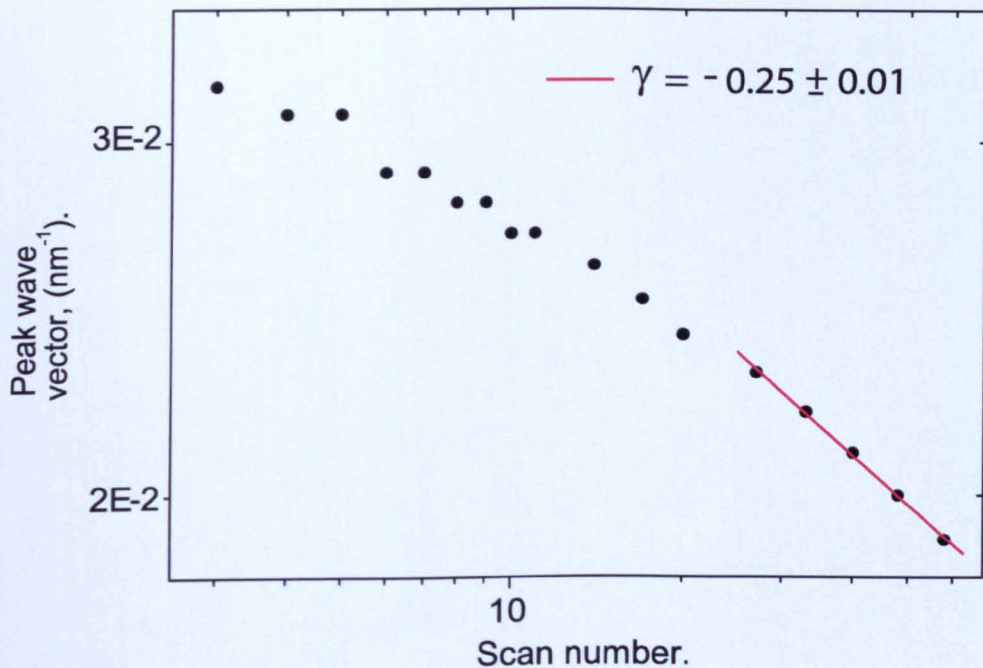
Figure 6.5: The peak of the radially averaged Fourier transform plotted against scan number, for the experimental run detailed in Figure 6.2.

The value for the coarsening exponent γ asymptotically approaches a value of 0.25 ± 0.01 for the morphological evolution displayed in Figure 6.2. A value

of $\gamma = 1/4$ is intriguing when considered in the context of the substantial literature on scaling exponents in coarsening systems. Rabani *et. al.* [52] have shown that the coarsening of PbSe nanoparticle cluster assemblies follows a $t^{1/4}$ dependence consistent with a cluster diffusion process. Well before this, Huse [97] discussed a correction to the value of $\gamma = 1/3$ for Ostwald ripening processes. In interconnected structures excess mass transport along domain boundaries lowers the value of the scaling exponent. Although this correction is theoretically a temporary one with γ returning to a value of $1/3$ after long times, the transient regime of lower γ was shown by simulation to persist for extensive periods of time [97].

In an attempt to clarify the exact mechanism for the structural evolution seen in Figure 6.2, simulations were carried out at the University of Nottingham by C. P. Martin using the metropolis algorithm put forward by Rabani *et. al.* [52] (modified to include next nearest neighbour interactions [1]) to investigate the coarsening dynamics of a 'spinodal' nanoparticle assembly. These simulations predict a scaling exponent of $\gamma = 1/4$ in excellent agreement with the experimental data up to very long total simulation times (2×10^5 Monte Carlo steps). In the simulations, nanoparticles are seen to move along the domain boundaries of interconnected structures during coarsening, diffusing from areas of high, towards areas of low, interface curvature.

Significantly, by driving the evolution of an interconnected nanoparticle assembly with a substantially stiffer AFM cantilever substantially more rapid coarsening occurs. A scaling exponent of $\gamma = 1/4$ nevertheless is still obtained. To draw another analogy between natural (thermal) coarsening and coerced coarsening, using a stiffer cantilever to drive the coarsening can be considered analogous to performing a natural coarsening experiment at a higher tempera-

ture. The independence of the scaling exponent on the cantilever stiffness coupled with the excellent agreement between experimental results and simulation infers that coerced coarsening of these interconnected structures is occurring due to the transport of nanoparticles, largely along domain boundaries.

6.4.4   Isolated islands

As the form of the cluster size distribution can be more sensitive to the coarsening mechanism than the power law exponent alone, deeper physical insight can be obtained from a consideration of the evolution of samples comprising an ensemble of isolated nanoparticle islands. Figure 6.6 shows four images taken at evenly spaced points in the coerced coarsening of a nanoparticle assembly with an areal coverage of 0.35ML.

Once again we use the peak value of the radially averaged Fourier transform as a measure of the characteristic length scale of the nanoparticle structures. Figure 6.7 **(a)** shows a logarithmic plot of the peak of the radially averaged Fourier transform against scan number for the morphological evolution depicted in Figure 6.6.

In Figure 6.7 **(a)** we see that the value of γ exhibits an abrupt change from a value of ~ 0.1 for the initial scans to, at approximately scan number 20, a value of 0.49 ± 0.02. This transient behaviour betrays an important contribution to the probe induced coarsening mechanism. In Figure 6.7 **(b)** we have plotted similar data for a sample having an initial morphology which mirrors that of Figure 6.6 almost exactly. In this sample we see there is no transition in the scaling exponent, it remains at a low value (~ 0.1) for the entire experimental run. This apparent inconsistency in the experimental data can be explained by reference to the inserts of Figure 6.7. In each case, the
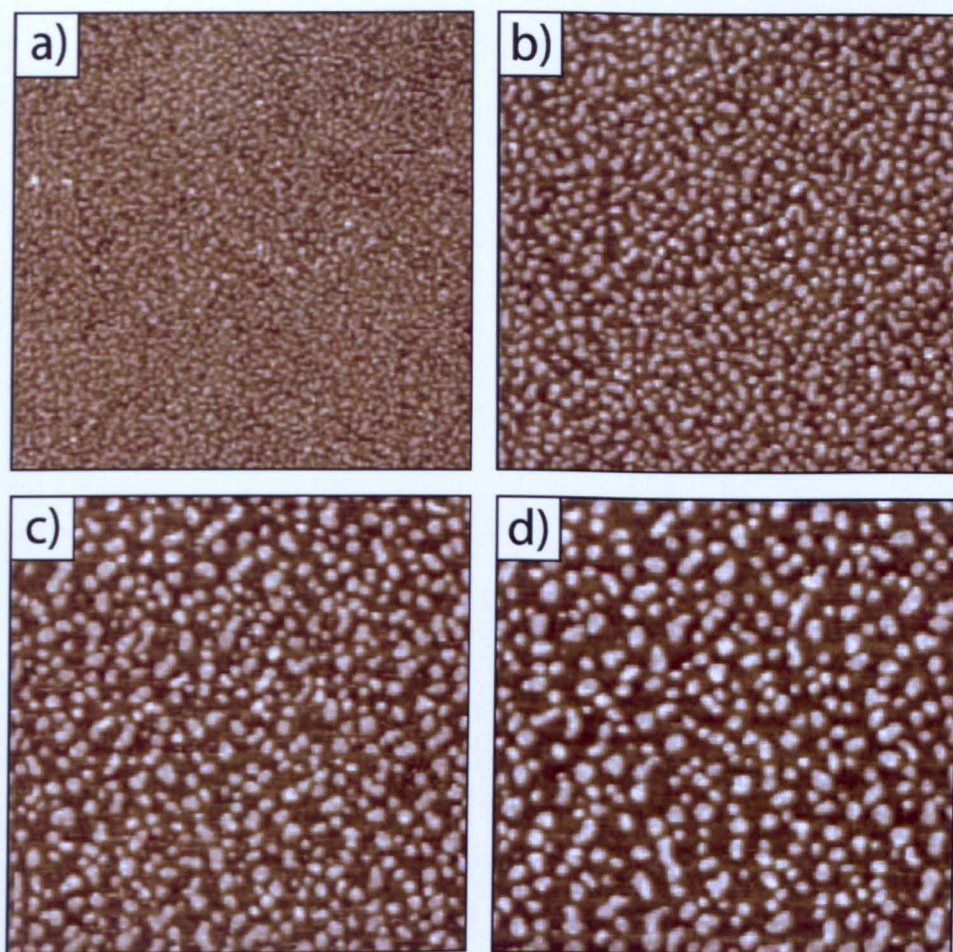
Figure 6.6: Coerced coarsening evolution of an ensemble of isolated nanoparticle islands. The images are taken from evenly spaced points throughout the experimental run, **(a)** 1st scan, **(b)** 30th scan, **(c)** 60th scan, and **(d)** 90th scan. All images are $1\mu m \times 1\mu m$ and the fractional area coverage of nanoparticles remains constant at approximately 0.35ML throughout the experimental run.

insert is a graph of the average island height vs scan number.

The AFM probes used for these experiments had a tip radius of curvature of $\sim$ 10nm. This is substantially larger than the size of a single nanoparticle (radius nanoparticle + thiol coating $\sim$ 2.3nm). As such the resolution of individual nanoparticles within the islands is not possible. The value recorded for the height at a point in the image within one of the islands is an average value for the group of nanoparticles under the tip at that point. As such,
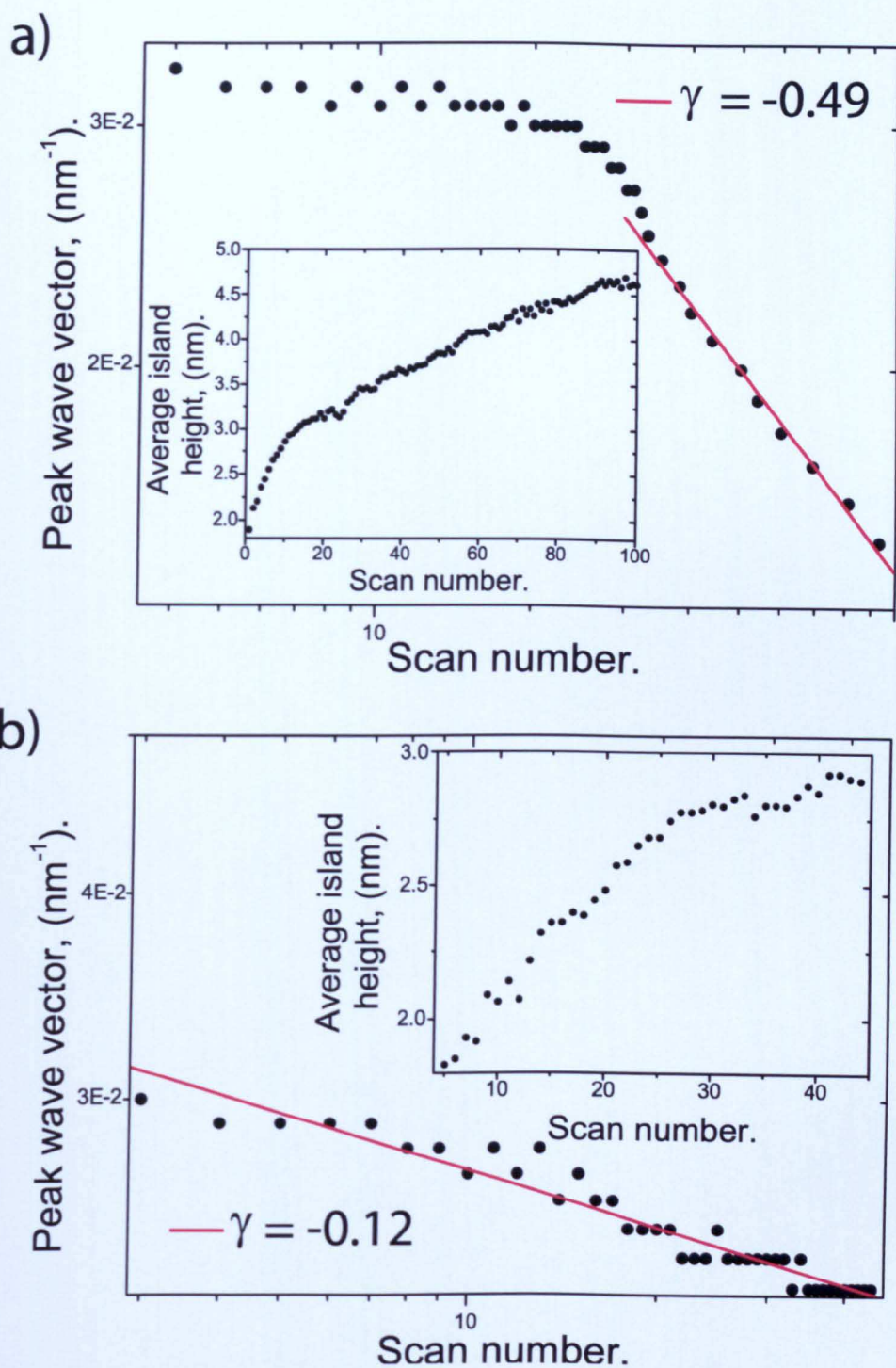
Figure 6.7: Peak value of the radially averaged 2D-FFT plotted against scan number for the coerced coarsening of two nanoparticle assemblies with isolated island morphologies. The inserts to parts (a) and (b) show the variation of average nanoparticle island height (nm) with scan number for the respective samples.

calculation of the average island height provides a measure of the density of nanoparticle packing within the islands.

In Figure 6.7 **(a)** (and many other experimental runs) the sharp transition in the value of γ corresponds directly to an abrupt change in the slope of the average height vs scan number curve. This occurs in Figure 6.7 **(a)** at approximately scan number 20 and at a *threshold* apparent height of ~ 3.2nm. This value of the threshold height is also reproduced in many other samples which display a transition to higher scaling exponent values. Corresponding to this sharp transition there is also a distinct increase in the degree of 'streaking' seen in the AFM images, indicative of significant mass transport. Conversely, in Figure 6.7 **(b)** the threshold height of 3.2nm is not reached (even after 50 scans) and the system remains in the transient regime with a correspondingly low value of the scaling exponent.

From these results we can infer that a significant percentage of the force exerted by the AFM probe in the initial scans of an experimental run accounts for driving the nanoparticles into more densely packed arrangements. Only when this initial packing phase induces a threshold density can we reliably begin to study the data for correspondence with different coarsening mechanisms. A tentative explanation for the presence of this transition concerns the nanoparticle's passivating thiol layer.

In the initial transient regime the nanoparticles are completely separated from each other with no overlap of their thiol coatings. As they are driven in to more densely packed arrangements a point is reached where the thiol chains coating different nanoparticles begin to interdigitate. This transition from a system of separate nanoparticles moving closer together to the forced interdigitation of the nanoparticle's thiol coating may account for the transition

in both the island height growth and the scaling exponent. As yet we have no definitive evidence for or against this hypothesis.

As mentioned above, the normalised island size distribution is often more sensitive to the dynamics of the coarsening process than the value of the scaling exponent. Therefore we produce plots of $F(s/<s>)$ vs $s/<s>$, (where $<s>$ is the average island size for a given image) for various frames of the experimental run depicted in Figure 6.6, only frames occurring after the transition (scan 20) to higher values of the scaling exponent are studied. These plots are shown in Figure 6.8 (**a**).

Although there is significant scatter in the data (due to the relatively small number of islands), it is clear that the functional form of the distribution is retained throughout the coarsening process. To improve the statistics we have therefore averaged the island size distributions for the final ten images in the experimental run and plotted this as the data points in Figure 6.8 (**b**). Also plotted in Figure 6.8 (**b**) are theoretical size distributions predicted for Ostwald ripening in both the evaporation-condensation (dashed blue line), and the diffusion (solid blue line) limited cases, equations 6.5 and 6.6. It is clear from this plot that the experimentally obtained size distribution is a particularly bad fit to either of these Ostwald ripening mechanisms.

However, by fitting the data to the scale invariant size distribution for coarsening by cluster diffusion-coalescence predicted by the Smoluchowski equation (equation 6.10) an extremely robust fit to the experimental data is obtained (red line). The value of α obtained from this fit is ~ 0. Using the relation between α and the growth scaling exponent (equation 6.9) this value of α should correspond to a value of $\gamma = 0.5$. This is also in excellent agreement with the experimental data shown in Figure 6.7.
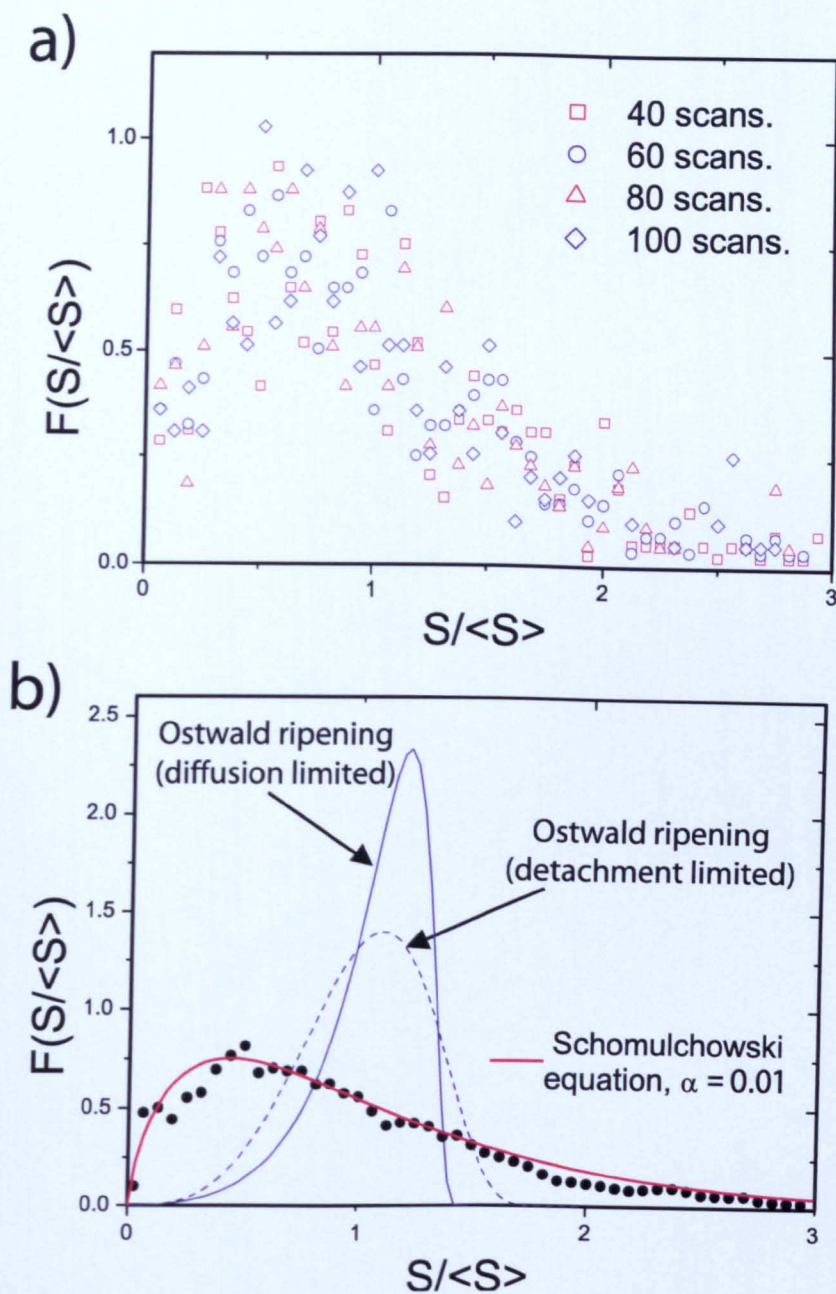
Figure 6.8: **a)** Normalised island size distributions plotted for several different images in the morphological evolution of the assembly detailed in Figure 6.6. **b)** Average of the normalised size distributions for the last ten scans of the experimental run. The red line shows a fit to the scale invariant size distribution predicted for a cluster diffusion coalescence coarsening mechanism by the Smoluchowski equation. Also plotted are the theoretical scale invariant size distributions for evaporation condensation limited, and diffusion limited, Ostwald ripening.

155

Within the Smoluchowski cluster diffusion-coalescence framework, the diffusion coefficient, D, is linked to the value of α by, $D \propto r^{-\alpha}$. A value of 0 for α directly implies a size independence of the diffusion coefficient for a nanoparticle island. This apparently counter-intuitive result can be rationalised on the basis of simple scaling arguments and by considering the raster motion of the AFM probe during scanning. The number of times that the tip interacts with an island during a single scan will be directly proportional to the radius of that island (assuming that the force is exerted at the edge of the island). If the diffusion coefficient for a *single* pass of the tip scales as r^{-1}, as is the case for thermally driven cluster hopping [52], then the overall diffusion coefficient becomes size independent.

6.5 Conclusions

We have shown that it is possible to mechanically drive the coarsening of spin-cast nanoparticle assemblies by repetitive scanning with an AFM probe. Although this mechanical drive towards equilibrium displays many of the characteristics of coarsening in thermally driven systems, there are some very significant differences.

The initial morphology of the nanoparticle assembly has a strong affect on the dynamics of the coerced coarsening process. For fractional area coverages of ~ 0.55ML, interconnected spinodal/labyrinthine nanoparticle structures are produced. The coerced evolution of these structures shows a remarkable degree of scaling, highlighted by the ability to collapse the radially averaged Fourier transform at any point in the evolution onto a time independent master curve. The values of the scaling exponent, γ, of 1/4 is related to a coarsening mechanism defined, primarily, by mass transport along the domain boundaries in

these interconnected structures. This relation is further reinforced by Monte Carlo simulations of the coarsening of similar interconnected morphologies which reproduce a scaling exponent of 1/4 with coarsening via interface mediated transport.

Nanoparticle assemblies consisting of isolated islands display markedly different coarsening dynamics. Following an initial transient regime the scaling exponent is shown to settle at a value of $\gamma = 1/2$. The initial transient regime is linked to the density of packing within nanoparticle islands. The initial scans of the coarsening process force the nanoparticles into closer packed arrangements. Once a threshold level of packing has been reached coarsening proceeds by a cluster diffusion coalescence mechanism. By fitting the island size distribution to the scale invariant size distribution predicted for diffusion coalescence coarsening by the Smoluchowski equation we obtain a value for the diffusion scaling exponent of 0. This apparent size independence of an island's diffusion coefficient is explained with simple scaling arguments and by taking into account the mechanism of the scanning process.

There are a few unresolved issues highlighted by these experiments. One particularly vexing question is why we observe coerced coarsening in nanoparticle assemblies which have been spin cast from a nonane solvent, but not in ones spin cast from a toluene solvent? An answer to this issue has been tentatively suggested as being related to the differences in solubility of tetraoctlyammoniumbromide (TOAB) in nonane and toluene [98]. The TOAB molecule plays an integral role in the synthesis method used to fabricate the nanoparticles used in this study [6] (see Chapter 2). Despite multiple purification steps it has been suggested by M. Brust that significant amounts of TOAB remain in toluene nanoparticles solutions following synthesis. The TOAB molecules, however,

have a markedly lower solubility in nonane than in toluene. Thus, following the evaporation of toluene and the redissolving of the dry nanoparticle precipitate into nonane which precedes these coarsening experiments, we would expect a significant decrease in the TOAB concentration. This reduction/absence of TOAB from the nonane nanoparticle solutions may be the reason that the assemblies spun from these solutions undergo coarsening. Coarsening experiments using ultra-purified toluene nanoparticle solutions are being carried out and as yet them seem to suggest an increased propensity for coarsening than assemblies produced from *dirty* toluene solutions.

Controlled, mechanical coarsening represents an intriguing and powerful method of guiding the evolution of nanostructures. A key feature of such a scanning probe-driven approach to equilibrium is the ability to quench the system simply by switching off the scanning process. This has particular potential in the generation of nanostructured assemblies with predefined correlation lengths.

Chapter 7

Electrical transport in cellular nanoparticle networks

The DC electrical transport through two-dimensional, topologically complex, spin cast nanoparticle networks, has been studied in the temperature range 4.5K-80K. The non-linear conduction through such networks displays nonlinearity exponent values $\zeta > 4.0$, significantly higher than similar exponents measured for networks possessing uncorrelated disorder. The high values of the scaling exponent ζ, along with a variable functional form of the I(V) characteristics for changing temperature, is attributed to the correlated disorder present in such networks.

7.1 Introduction

Following significant advances in self assembly and synthesis techniques [49, 53–55], the understanding of transport behaviour through both topologically ordered and disordered nanoparticle arrays has undergone key advances. Knowledge of how transport is affected by the level of structural disorder in

such networks is pivotal for the successful integration of nanoparticle arrays into the next generation of electronic devices.

Spin-cast nanoparticle networks have been shown to exhibit a wide array of different pattern morphologies. Spin-casting has the advantage over other nanoparticle array fabrication techniques that it is a quick and facile way of producing two-dimensional nanoparticle structures with well defined correlation lengths. These correlation lengths can range from tens of nanometers up to tens of microns [1, 11], as discussed in Chapter 4. Spin-coating has also displayed the ability to produce *hierarchical* structures, possessing multiple well defined correlation lengths.

In order to employ spin-cast nanoparticle networks in the fabrication of electrical devices and nanostructured designer materials, a greater understanding of the effect that the correlated disorder in such arrays has on electrical transport is required. In the following chapter we study the role that network morphology has on DC conduction through two-dimensional nanoparticle arrays with varying degrees of topological complexity.

7.2 Electronic transport in nanoparticle arrays

In the following sections an outline of the theory of electrical transport in two-dimensional nanoparticle arrays will be given. These ideas lead on from discussions of the electronic structure and charging properties of single nanoparticles given in Chapter 2. Particular attention will be paid to the role that disorder plays in defining the transport characteristics of such arrays.

Using the analogy of nanoparticles as artificial atoms, in a 2D hexagonal close packed array of atoms all of the atoms will be identical and evenly spaced. In a similar 2D array of nanoparticles, however, the presence of disor-

der is unavoidable. The distribution of nanoparticle sizes and of interparticle distances will lend an inherent level of disorder to any nanoparticle network. Variations in the inter-particle distance are of particular importance for electrical transport in such arrays as the tunnelling current between nanoparticles is exponentially sensitive to this distance. Disorder will also be present in the form of asymmetries in the potential landscape which the array inhabits, as we shall see in the following sections, mainly due to randomly positioned charge impurities trapped in the substrate supporting the array. In order to understand the conduction behaviour of nanoparticle networks it is vital to understand the roles that these different forms of disorder play.

7.2.1 Non-linear transport

The effect of disorder on conduction through a linked array of resistors was discussed by Roux *et. al.* [99]. In that work, simulations of conduction through two dimensional arrays of resistors were carried out. Each resistor was assigned a threshold voltage, below which it was an insulator and above which it conducted in accordance with Ohm's law. With threshold values set equally for all resistors the conduction behaviour of the array as a whole was similar to that of a single resistor. This behaviour comprised of; *(i)* a region around zero voltage where no current flowed; *(ii)* onset of conduction at a fixed threshold voltage which was proportional to the threshold voltage of an individual resistor and the width of the array in terms of the number of resistors; and *(iii)* linear behaviour of the conduction after the threshold voltage was exceeded.

Importantly, when disorder was introduced by assigning threshold values for the individual resistors randomly from a normal distribution, the conduction behaviour was significantly altered. The conduction behaviour of the array

was now split into three distinct regimes. Once again, a region of zero conductance around zero volts was present with the onset of conduction occurring at a threshold voltage defined by the path of minimum resistance across the array. After this threshold voltage was exceeded the conductance was nonlinear with respect to the voltage. The current through the array in this regime was related to the voltage via a power law dependence,

$$I \propto (V - V_t)^\zeta, \tag{7.1}$$

where V_t is the threshold voltage of the array, and the scaling parameter ζ was found to be approximately equal to 2 for large array sizes.

The nonlinear nature of the conduction exemplified by equation 7.1 may be explained in terms of the many different conduction paths through the array. The threshold voltage for a particular conduction path through the array is simply the sum of the threshold voltages for the individual resistors constituting this path. As such, the threshold voltages for the various possible conduction paths through the array have a distribution similar in form to that of the distribution of thresholds for the individual resistors. As the voltage across the array is increased past its threshold value an ever-increasing portion of these paths become available for conduction. Conduction through the paths that are already open increases linearly with the potential across the array. The opening of new conduction paths produces the nonlinear nature of the conduction behaviour. Finally, when the potential across the array exceeds the threshold values for all the possible conduction paths through the array, the current in the array will once again adopt a linear relationship to the voltage.

7.2.2 Reduced voltage and power law scaling

Following on from the study of Roux *et al.*, work by Middleton and Wingreen (MW) in 1993 [100] centered on the simulation, and theoretical treatment, of the conduction properties of arrays of capacitively coupled metal dots. A unique conduction property of quantum dots, namely Coulomb blockade induced threshold conduction behaviour, make them the perfect experimental basis to test the nonlinear conduction predictions made by Roux *et al.*, [99].

The simulated system studied by MW consisted of 1 and 2 dimensional square arrays of metal dots between planar electrical contacts. Each dot is linked via tunnel barriers to neighbouring dots and the planar contacts, and the whole array is capacitively coupled to an underlying ground contact, see Figure 7.1.
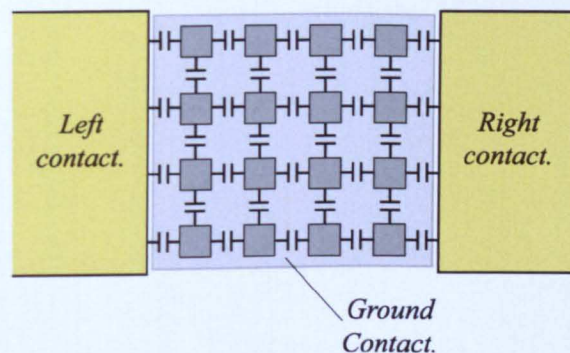
Figure 7.1: Schematic representation of the capacitively coupled metal dot array studied by Middleton and Wingreen [100]. The dots are capacitively coupled to their neighbours, and to a ground contact which underlies the entire array. Each dot is separated from its neighbours, and the left and right contacts, by tunnel barriers.

The tunnelling resistance between neighbouring dots, and between the left and right contacts and adjacent dots, was assumed to be constant, and large compared to the resistance quantum $(R \gg h/e^2)$. The thermal energy was also assumed to be much lower than the charging energy of an individual dot $(k_B T \ll e^2/C)$. With these assumptions in place the dots are in the Coulomb

blockade regime, where single electron charging will dominate the transport properties.

The most striking difference between the work of Middleton and Wingreen and previous simulations of similar systems [101] was the inclusion of disorder in the system. In this case disorder was included in the form of random offset charges placed on each of the dots, q. The presence of these charges is rationalised as being caused by the presence of nearby charged impurities within the array or in the underlying substrate. The magnitude of the offset charges was set by MW to be in the range $0 \leq q \leq e$.

Another key assumption in the model of MW was that of *short screening length*. The screening length describes to what degree a charge on a particular dot is screened from the effects of charges on other dots. It was shown that the screening length was dependent on the ratio C/C_g, where C is the capacitance between adjacent dots, and between dots and the planar contacts, and C_g is the capacitance between dots and the ground contact. As this ratio approaches zero, charges on a particular dot are effectively completely screened from the charges on other dots as the capacitative coupling between dots is negligible compared to that between dots and the ground contact.

The picture of charge transport described by MW through such an array is that of an advancing *front* of charge. By combining the short screening length assumption, and the basic capacitance equation $Q=CV$, we see that the on-site potential felt by dot i is equal to,

$$(Q_i + q_i)/C_g, \qquad (7.2)$$

where Q_i is the charge on dot i due to conduction electrons and q_i is the random induced charge on dot i due to the local charge disorder. Thus, to add one

electron to a dot (an increase in charge of e), the on-site potential must be increased by an amount e/C_g. Figure 7.2 (a) shows a schematic representation of charge flowing onto a 1D array of dots with the potential across the array slightly less than the array's threshold potential.

For 2D arrays we can imagine that, with an increasing potential difference applied to the contacts, we have an advancing front of charge moving across the array, Figure 7.2 (b). For a certain voltage below threshold, charges will penetrate further into the array at different points, dependent on the local charge disorder. Conduction through the array commences when the first part of this advancing charge front touches the far side of the array, i.e when the first conduction path opens up through the array.

The simulations and theoretical treatment predicted that the size of the threshold voltage is proportional to the array width. In addition, by using arguments based on the growth of interfaces [102], Middleton and Wingreen predicted a current voltage relationship of,

$$I \sim (V/V_T - 1)^\zeta, \qquad (7.3)$$

with values of $\zeta = 1$ or $5/3$ for 1 and 2 dimensional arrays respectively. The term *reduced voltage* is used for the quantity *(V/V_T-1)*, logarithmic plots of the current against the reduced voltage should produce a straight line with a gradient equal to ζ if the power law relationship of equation 7.3 holds.

Experimental verification of the work by Middleton and Wingreen on lithographically patterned arrays of metallic islands was quick to follow [103–105]. Experimental values for the scaling parameter ζ measured on arrays of size N were recorded as $1.4 < \zeta < 1.7$ (2D, $N = 200$) [103]; $\zeta = 1.36$ (1D, $50 < N < 2000$), and $\zeta = 1.80$ (2D, $40 < N < 400$) [104]; and $\zeta = 1.58$ and 2.01 (2D, N
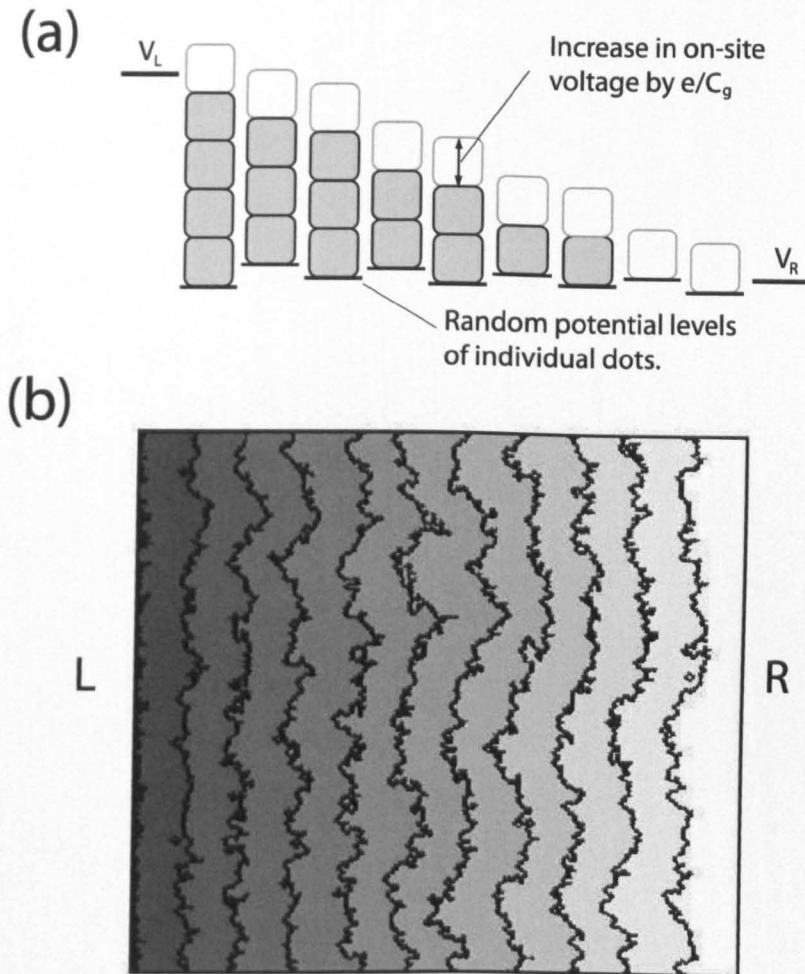
Figure 7.2: **(a)** Schematic representation of charge flowing onto a 1D array of dots. The voltage across the array $(V_L\text{-}V_R)$ is less than the threshold voltage for the array. V_L is high enough to overcome the random potential of the first dot and to move four electrons onto it (shaded boxes). The random potential of the second dot is higher than that of the first therefore the on-site potential is only enough to move three electrons onto the second dot. The potential across the array must be increased by e/C_g for each such up-step in the random potential. **(b)** Advancing charge front in a 2D array of metal dots (array size 160×160), the lines are contours of constant charge occupation (contour spacing is 5 charges). The lines represent the extent to which charge flows onto the array for different voltages below threshold. Transport across the array commences when the first charge reaches the right hand contact [100].

= 40) [105].

These values are in rough agreement with those produced by the theoretical treatment of Middleton and Wingreen. There are, however, some noticeable differences. These deviations from the predictions of Middleton and Wingreen's theories were attributed to either finite size effects or the presence of forms of disorder other than that due to random charges.

7.2.3 The role of disorder

With the advent of simple synthesis methods for large quantities of stable ligand-passivated nanoparticles, [6], attention moved away from charge transport studies using lithographically patterned arrays of metal dots towards arrays of close packed colloidal nanoparticles. The greatly reduced size of nanoparticles, as compared to lithographically patterned structures, allowed the Coulomb blockade regime to be studied at more easily obtainable experimental temperatures, 10K-100K as opposed to a few mK. The extreme versatility of nanoparticle synthesis methods also allowed a more precise control of particle size, inter-particle distance and thus inter-particle electrical resistance. This combination of easily obtained experimental conditions, and wide ranging control over the system parameters, fuelled a vast quantity of research into electrical conduction through nanoparticle arrays.

Many studies initially considered extremely small 2D arrays (<100nm array size) [106, 107], or large 3D arrays with no accurate measurement of the level of disorder present [108]. The first work to deal separately with the different aspects of local disorder in 2D nanoparticle arrays in a systematic manner was that of Parthasarathy *et. al.* [109]. Using methods developed by Lin *et. al.* [49], 2D arrays of nanoparticles with long range structural order were

formed. By comparison of the conduction through arrays with varying degrees of structural order, the separate effects of three main types of disorder could be observed (see Figure 7.3). These three distinct types of disorder which may be present in two dimensional nanoparticle arrays are cited by Parthasarathy *et. al.* [109] as random charge disorder local structural disorder, and long-range topological disorder, see Figure 7.3.

1) Random charge disorder:

This is similar to the disorder introduced by Middleton and Wingreen into their simulations [100]. Randomly positioned trapped charges in the substrate induce a charge in nearby nanoparticle altering their charging energies.

2) Local structural disorder:

This means variations in the distances between individual nanoparticles in a close packed array and thus variations in the inter particle resistance values. This type of disorder is caused by packing irregularities within the array, and variations in nanoparticle size.

3) Long-range topological disorder:

This takes the form of voids in the nanoparticle array, or areas consisting of multiple nanoparticle layers. As will be discussed later, the effect this disorder has will be strongly dependent on the correlation of the structural features which cause it.

By using nanoparticle solutions with known size dispersions (mono-dispersed within 5%), Parthasarathy *et. al.* were able to effectively remove the effects of local structural disorder. Conduction behaviour was measured for arrays of width $200nm < D < 700nm$. Some arrays had long-range structural order, while others contained large voided areas or areas of double layered array.
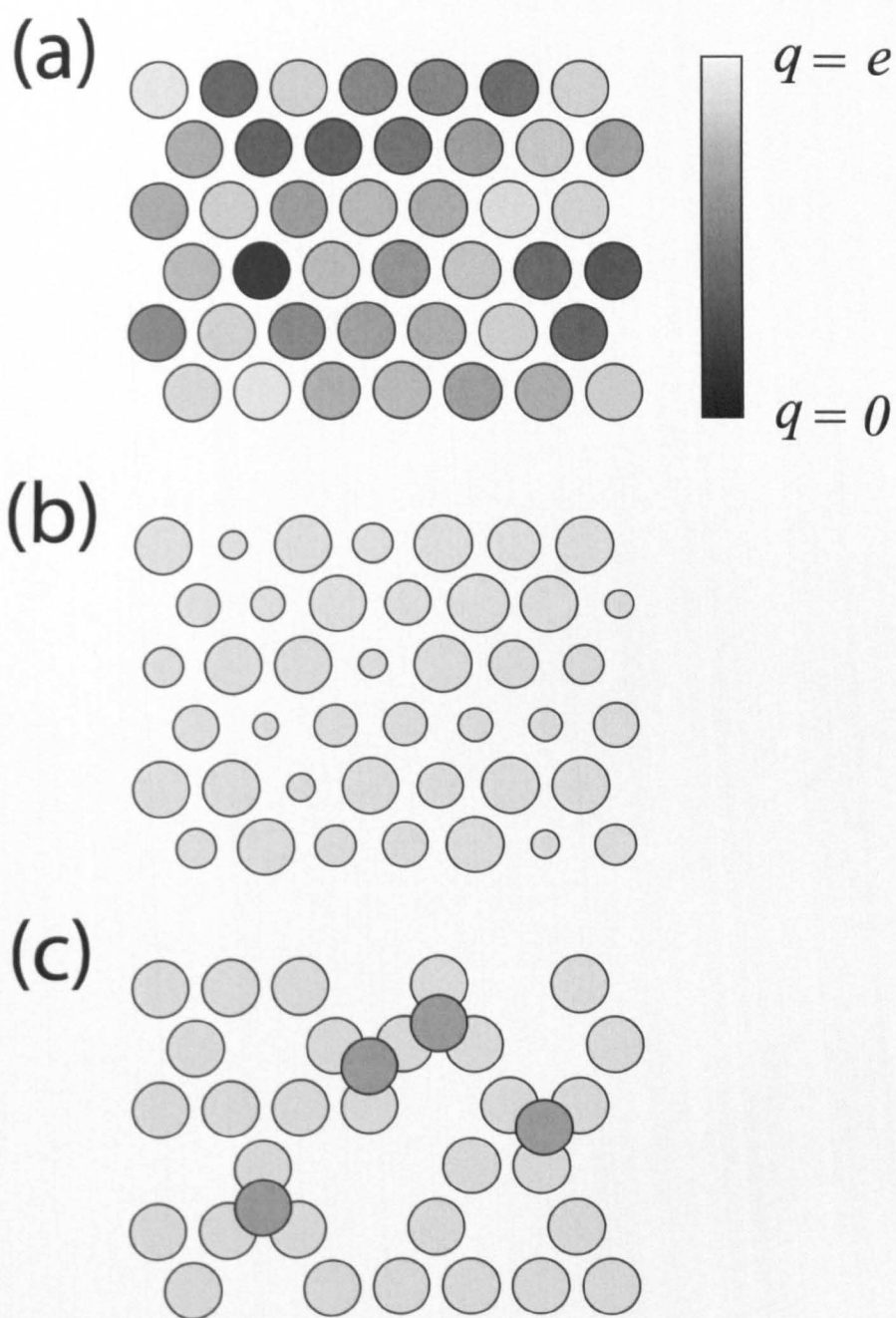
Figure 7.3: The three types of disorder present in nanoparticle arrays, **(a)** random charge disorder, **(b)** local structural disorder, and **(c)** long-range topological disorder.

The structurally ordered arrays showed uniform scaling behaviour from sample to sample, with a constant value of the scaling parameter $\zeta = 2.25$. The structurally ordered arrays also displayed a linear dependence between the threshold voltage and the width of the array, as predicted by MW [100]. For the structurally disordered arrays, however, a much wider range of scaling parameters was obtained. Importantly, it was no longer possible to fit the data to the power law dependence outlined in equation 7.4 by using a single value of the exponent ζ, see Figure 7.4.
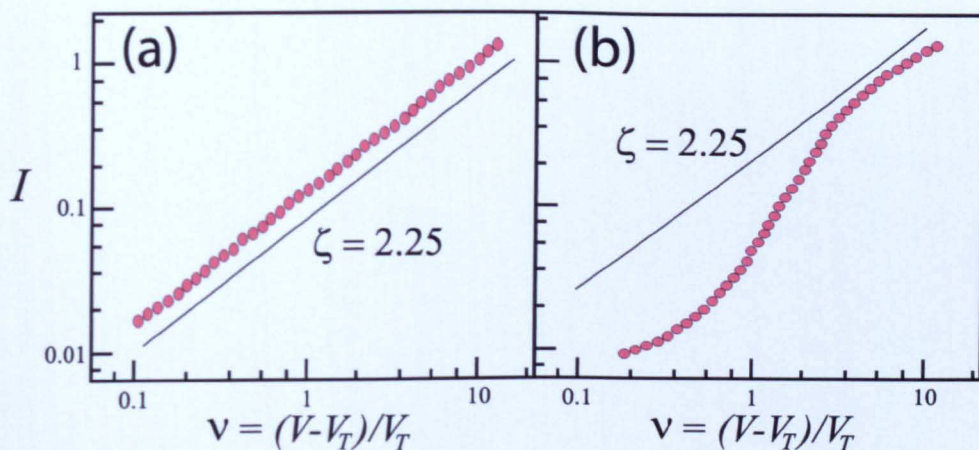
Figure 7.4: Schematic representations of conduction scaling behaviour in nanoparticle arrays **(a)** with, and **(b)** without, long range topological order.

These deviations from simple power law scaling behaviour are explained in terms of the presence of bottlenecks for charge transport in the array caused by the topological disorder. Voided areas within a nanoparticle network produced what were essentially an array containing locally 2D patches, linked via 1D bottlenecks. The scaling parameter ζ was seen to adopt a "transiently" larger value for the structurally disordered arrays, see Figure 7.4. The transient increase in the value of ζ occurs because of the narrower distribution of threshold values for the one-dimensional bottlenecks in the array.

Once the threshold voltages of each of the bottlenecks has been surpassed

the array becomes essentially an amalgam of 2D arrays. The scaling behaviour then returns to that expected of an ordered 2D array and, indeed, this behaviour was observed as the scaling parameter decreased at higher voltages [109].

Even though the values of ζ were constant for the arrays possessing long range topological order, they were however significantly higher than the ζ = 5/3 value predicted by theory for 2D arrays [100]. This difference was attributed to the short range structural disorder present within the arrays. Specifically the MW model only includes disorder in the form of random charges induced on nanoparticles. The tunnelling resistance between the particles maintains a constant value. However, in reality, the tunnelling resistance will have an exponential dependence on the particle separation. Thus, even small variations in the particle dimensions and packing will induce non-negligible amounts of disorder.

Along with the inter-particle resistance, a nanoparticle's charging energy is also dependent upon its dimensions (see Chapter 2). Therefore, variations in nanoparticle size will also bring about disorder in the form of a distribution of charging energies. It was these sources of short range structural disorder that Parthasarathy *et. al.* put forward as the explanation for the higher-than-expected values of the scaling parameter in arrays with long range structural disorder. The level of disorder has vital implications for the conduction properties of nanoparticle arrays. Both the global structural disorder and the local structural disorder will effect the way current paths meander through the array, affecting the scaling behaviour of the conduction [109].

In the following work we study the effect that long range topological disorder in spin cast nanoparticle films has on conduction. Spin cast nanoparticle films form a subset of array morphologies, the conduction properties of which

have not previously been studied. Although the effects of long range structural disorder have previously been observed, this disorder has always been present in an uncorrelated form [100, 109]. The well defined correlation lengths obtained in spin cast nanoparticle networks allow us to probe the affects that *correlated* structural disorder has on conduction through nanoparticle arrays.

7.3 Experimental details

Colloidal gold nanoparticles in toluene solutions were synthesised using the method outlined by Brust *et. al.* [6]. Nanoparticles were ~2nm in diameter, with a ~15% size distribution as measured by small angle X-ray scattering (SAXS). Two separate solutions were synthesised, each with a particular length of passivating thiol molecule, namely, pentanethiol (C_5) and octanethiol (C_8). The substrates used in these experiments were silicon, coated with a 200nm layer of thermally grown silicon dioxide. The presence of the thick oxide layer prevented contamination of the conduction data by parasitic conductance through the underlying silicon layer.

Nanoparticle networks were formed on these substrates by the spin casting of quantities of the desired nanoparticle solutions. The coverage and morphology of the networks obtained in this fashion were controlled by the variation of the nanoparticle concentration in solution prior to spin coating (see Chapter 4). In order to study the conduction through these networks, electrical contacts need to be deposited onto the arrays. The standard fabrication routes for electrical contacts with micron spacing and below are lithographic processes. Lithographic processes, however, entail the deposition of a layer of material known as a resist onto the surface. This resist layer is then patterned by either selective exposure to UV light, or by an electron beam. The resist is then

exposed to a solvent which removes the resist layer from the substrate in the patterned areas. Metal contacts are then deposited onto the exposed regions of substrate, and the remaining resist removed to leave the desired metallic structures on the surface.

This technique creates a range of difficulties when attempting to contact nanoparticle networks. Nanoparticle networks cannot be deposited prior to a lithography process. The various stages of the lithographic process, most notably the solvent immersion steps for the removal of resist layers, cause irreversible damage to nanoparticle networks. However, if the lithography process is performed prior to the spin casting of the nanoparticle networks the presence of the metallic contacts on the surface during the spin coating process greatly perturbs network formation.

In order to solve these problems a novel shadow mask technique was derived for the evaporation of gold contacts directly on top of nanoparticle networks. A mask was produced which consisted of an array of 200μm wide slits. At right angles to these slits, lengths of 5μm and 10μm tungsten wire were attached to the surface of the mask. The sample to be contacted is then laid face down on this mask, and gold evaporated through the mask onto the surface. This technique produces pairs of planar gold contacts 200μm wide and with contact separations of either 5μm or 10μm.

The complete lack of any surface preparation steps prior to contact deposition means that virtually no damage to the nanoparticle networks occurs. Also, as the gold is deposited after the spin coating of the network, and directly on top of the network, excellent electrical contact is obtained whilst exerting no influence on the network morphology.

Contact separations smaller than 5μm were obtained via a two stage con-

tact evaporation. Two evaporation steps were carried out with the mask held at different angles to the evaporation source, see Figure 7.5. A three-dimensional representation of a typical set of contacts produced in this fashion is also shown in Figure 7.5. Following contact deposition samples were mounted on standard To5 headers, and the deposited gold contacts bonded to the pins of these headers. Each sample consisted of a number of different electrode gaps, each with different dimensions. Prior to taking electrical measurements the nanoparticle network within each electrode gap was imaged extensively using AFM.
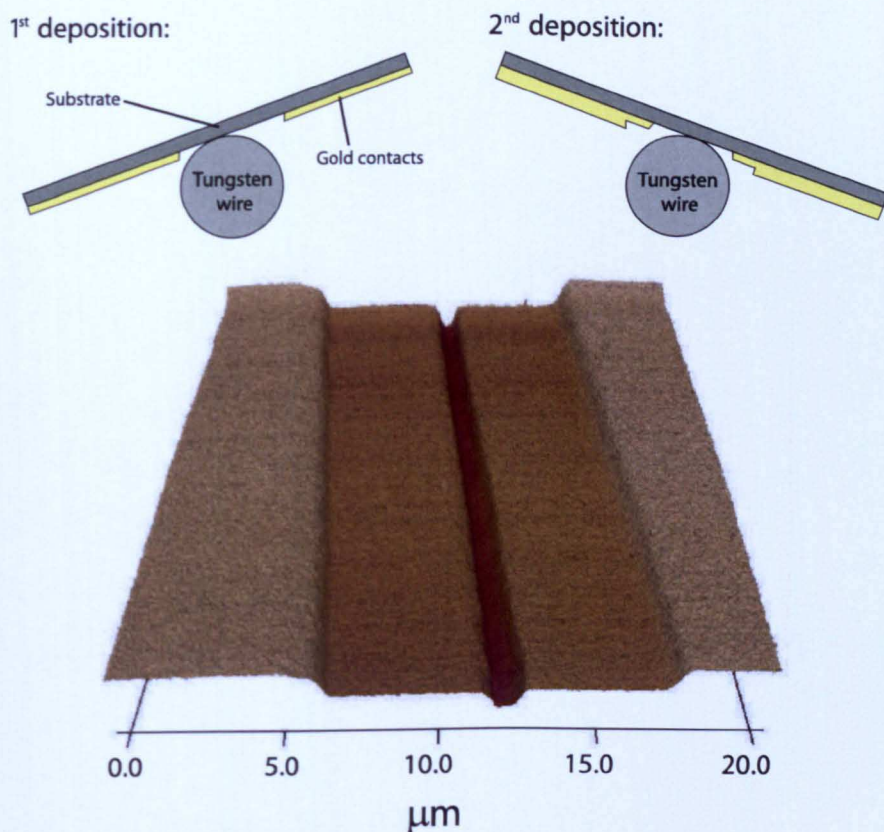
Figure 7.5: Contacts are deposited directly onto substrates via a shadow masking technique. By employing two deposition steps, performed at different angles relative to the evaporation source, contact separations smaller than the minimum diameter of tungsten wire may be obtained. Also shown is a three-dimensional representation of a typical set of contacts obtained by this process.

Samples were then placed in a liquid helium flow cryostat and electrical

transport measurements across the various electrode gaps was carried out at temperatures between 4.5K-80.0K. DC I(V) curves were obtained between ±20V, with a current resolution of ~ ±100 femto amps.

7.4   4.5K measurements

7.4.1   Uncorrelated disorder

Before beginning to study the conduction behaviour of the more topologically complex cellular nanoparticle networks, a sample was prepared which was made as close to a complete monolayer of nanoparticles as possible. Figure 7.6 shows a three-dimensional representation of an AFM image of a section of this network. The beginnings of the gold contacts are just visible at the edges of this image as the areas of increased roughness.

From Figure 7.6 we can see that this network consists of large areas of well-packed nanoparticle monolayer, interspersed with a number of randomly positioned voids. The random nature of the positioning of these voids gives the structural disorder present in this array an uncorrelated nature. On this sample two sets of contacts were found which displayed measurable conduction properties, with 1.0μm and 4.0μm electrode spacings. The current plotted against the reduced voltage $(I \ vs \ (V\text{-}V_T)/V_T)$ for the 1.0μm electrode gap is displayed in Figure 7.7 **(a)**.

Determination of the value of the threshold voltage (V_T) for each electrode gap was performed using a method outlined by Ancona *et. al.* [110]. The current, I, multiplied by dV/dI is plotted against the voltage, V. A linear fit is made to the data in a voltage range well past the threshold voltage, this line
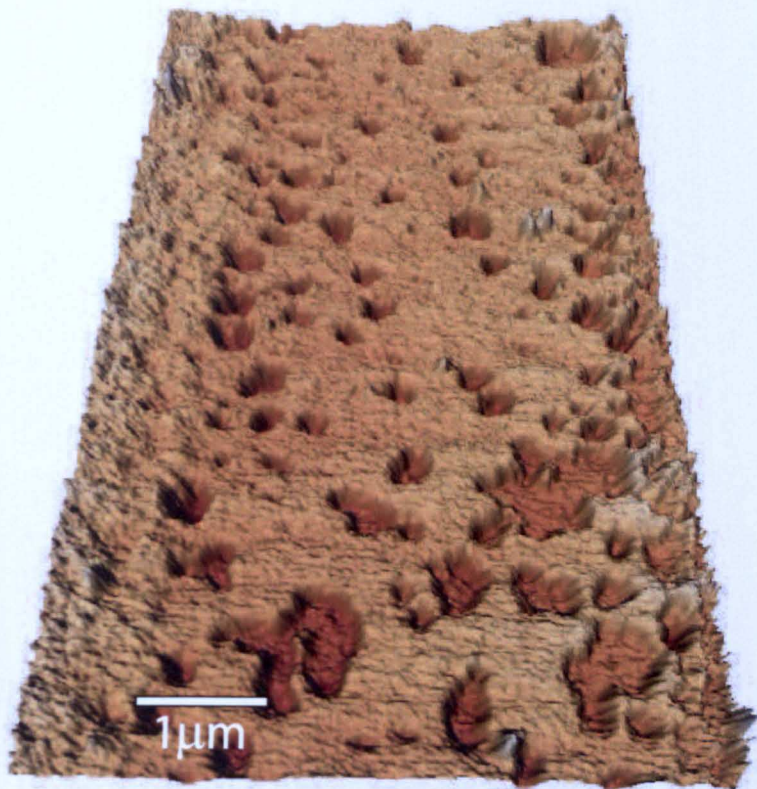
Figure 7.6: Three-dimensional representation of an AFM image of a well ordered C_5 passivated nanoparticle network between gold contacts.

is then extrapolated back to zero current, and the value of the intercept with the x-axis taken as the threshold voltage value, see Figure 7.7 **(b)**.

A value of $\zeta = 2.37\pm0.05$ was obtained for the 1.0μm electrode gap. This value was obtained for reduced voltage values, $V_T > 2$. At lower values of the reduced voltage $(0.6 < V_T < 1.6)$ ζ adopts a value of 2.56 ± 0.09. This small deviation from a power law dependence with a single value of ζ is a reflection of the small, but however still visible, level of structural disorder present in the nanoparticle network, see Figure 7.6.

Parthasarathy *et. al.* [109], observed constant values of $\zeta = 2.25\pm0.1$ for arrays with almost perfect structural order. This single value for ζ is expected in the MW theory of charge transport through a structurally ordered
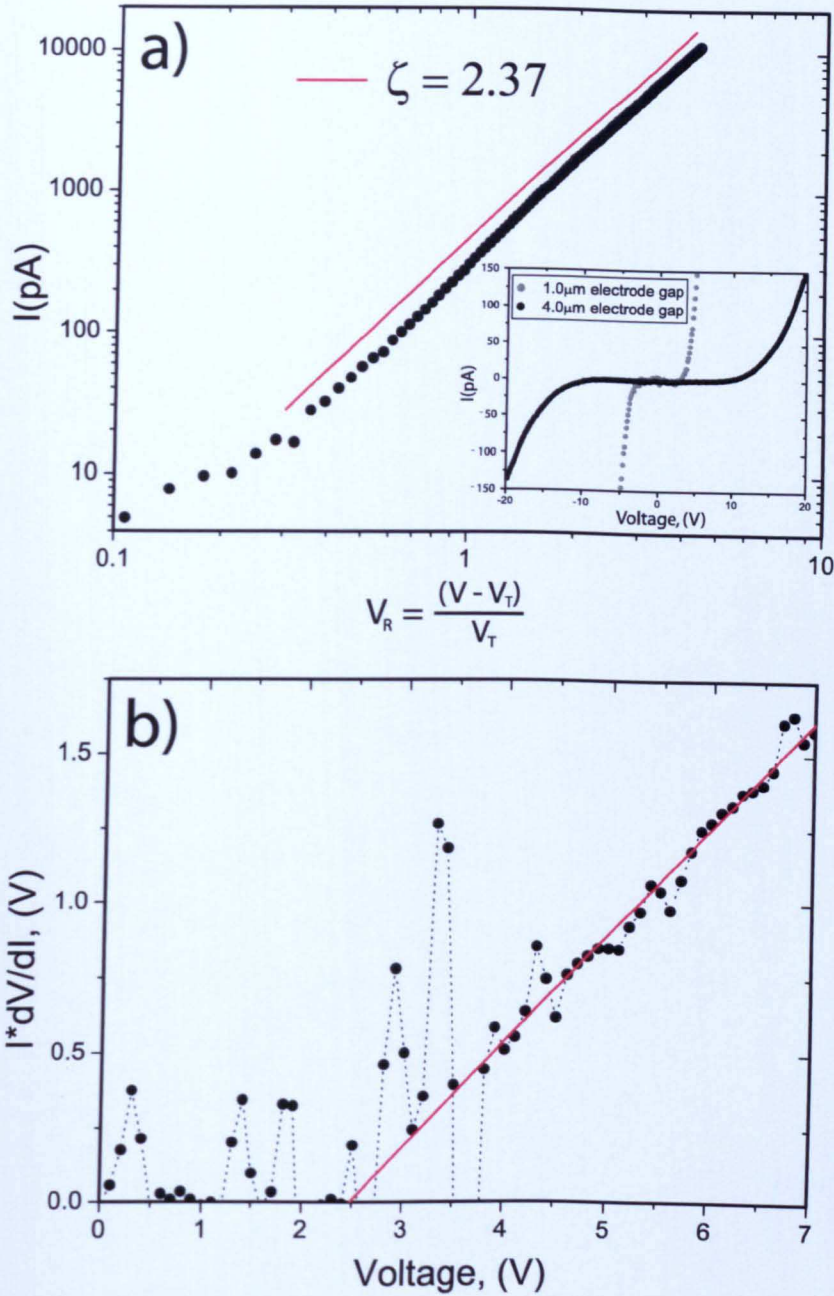
Figure 7.7: Results of DC electrical transport measurements for the well ordered C_5 passivated nanoparticle network. **(a)** Current against reduced voltage plotted for the $1.0\mu m$ electrode gap, linear fit is for $v > 2$. The insert to a) shows the standard *I(V)* curves for both the $1.0\mu m$ and $4.0\mu m$ electrode gaps. **(b)** I*dV/dI against voltage showing the method of measuring the threshold voltage, the intercept with the x-axis for the fitted line is taken as the threshold voltage.

two-dimensional array. However, with the inclusion of a number of randomly positioned voids into the array, Parthasarathy *et. al.* observed ζ adopting a transiently higher value in the reduced voltage range $0.6 < V_T < 2$. At higher voltages the value of ζ returned to 2.25.

The results displayed here are in excellent agrement with those of Parthasarathy *et. al.* (despite a number of strong differences between the sample, as discussed below). The value of ζ for $V_T > 2$ agrees with that calculated in [109] to within the respective experimental errors. A cursory observation of the network displayed in Figure 7.6 and the disordered networks studied in [109] show striking similarities in the level and distribution of voided areas.

This deviation from single exponent power law behaviour was explained in terms of neighbouring voids in the network creating bottlenecks to charge transport [109]. The basis of the conductivity exponent ζ in the MW theory concerns the meandering of current paths throughout the array [100]. Even in completely regular two-dimensional nanoparticle arrays current paths will meander due to the random potential landscape that the array inhabits.

The current paths display transverse fluctuations over a distance $\xi_\perp$ (the transverse correlation length) $\propto V_T^{-\eta}$, due to disorder. The total current through an array will be proportional to the number of separate conduction paths through the array. The number of separate conduction paths can be estimated from the transverse correlation length as $W/\xi_\perp$, where W is the width of the array.

From these two statements a relation between the current through the array and V_T can be obtained such that $I \propto W V_T^{\eta+1}$, where $\zeta = \eta + 1$. The precise value of the transverse correlation length exponent, η, can be obtained in several ways, MW theory uses a value based on the Kardar-Parisi-Zhang

(KPZ) model for interface growth [102]. This produces a value of $\zeta = 5/3$ for two-dimensional arrays.

The bottlenecks to charge transport created by voids in the array locally cut off transverse fluctuations in the conduction paths. In an extreme case of large levels of structural disorder, conduction may be limited to a few, essentially one-dimensional, conduction paths. The presence of these bottlenecks changes the nature of the array from purely two-dimensional to an amalgam of two-dimensional patches linked by one-dimensional bottlenecks.

The "transient" values of ζ correspond to the voltage range where the thresholds for these one-dimensional bottlenecks are being surpassed. After these one-dimensional channels have all been opened, conduction behaviour reverts to that of a two-dimensional system, as observed in [109] with ζ for the disordered arrays at high voltages returning to the value obtained for ordered arrays.

The value of ζ obtained for the network displayed in Figure 7.6 is slightly higher than that obtained by Parthasarathy *et. al.*. This may be a reflection of certain differences between the experiments. Firstly, a much narrower nanoparticle size dispersion was present in [109] as compared to this work, 5% as compared to 15%. Secondly, the lithographically defined contacts used in [109] have far smoother and more well defined edges than the shadow mask fabricated contacts employed here.

Another key difference between this work and that described in Ref [109] is the width of the contact arrangements. These are two orders of magnitude greater in our study, 200μm compared to 2μm in [109]. However, previous studies have shown that there is a rapid saturation of ζ with respect to the array width [111]. This saturation arises because conduction paths which are

significantly longer than the inter-electrode separation provide a negligible contribution to the overall current. Therefore the much wider contacts employed in this study are not expected to induced significant differences between the results and those of [109].

The agreement seen between results for the array shown in Figure 7.6 and morphologically similar arrays in [109] shows that the shadow masking contact fabrication, the wider nanoparticle size distribution, and the greater contact widths, do not adversely affect the scaling properties of the network conduction in a major way.

7.4.2 Correlated disorder

Now we shall move on to study conduction through more topologically complex network structures. The network displayed in Figure 7.8 is a typical example of a network possessing what we term as *correlated* structural disorder. In cellular nanoparticle structures such as this, the length and width of the individual network branches have a strong correlation. This is a direct consequence of the evaporative de-wetting process by which they are formed. The overall structure of the network also shows correlation in the form of the larger scale network.

This correlated nature of the disorder has a radical influence on the scaling of conduction properties in these network structures. Due to extreme difficulties in obtaining contact-network arrangements which displayed measurable conduction behaviour, the results at present are limited to two samples. One sample consisted of a C_8 passivated nanoparticle network (an example of this network is displayed in Figure 7.8) which contained three viable sets of contacts with electrode separations of 0.5μm, 1.0μm, and 3.6μm. The second
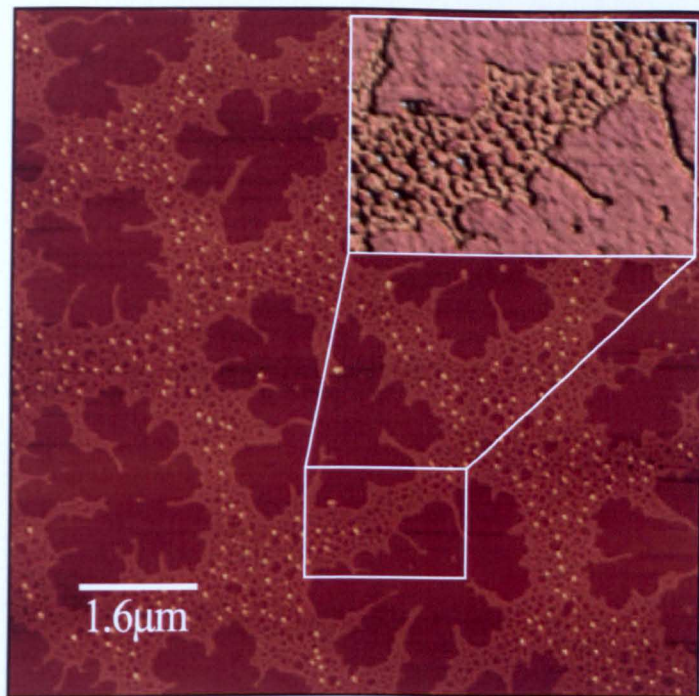
Figure 7.8: Typical tapping mode AFM image of one of the topologically complex nanoparticle networks used for the electrical transport measurements. The image size is 8μm $\times$ 8μm. Networks existing over two distinct length scales can be clearly seen. The inset shows an enlargement of the smaller scale network.

sample consisted of a C_5 passivated network with one set of contacts with an electrode gap of 0.5μm.

Threshold voltages for the networks between these various contact arrangements were once again obtained via the method outlined by Ancona *et. al.* [110]. Figure 7.9 shows plots of the current against the reduced voltage for the three electrode gaps on the C_8 passivated sample.

The most obvious difference between the conduction properties of these more complex network structures is the greatly increased values of ζ that are obtained. Values of ζ greater than four are obtained in certain voltage ranges for all of the electrode gaps on the C_8 sample, Figure 7.9. The form of the $I(V_T)$ curves also displays conduction behaviour that has been driven even further from a single power law dependence than for the network displayed in
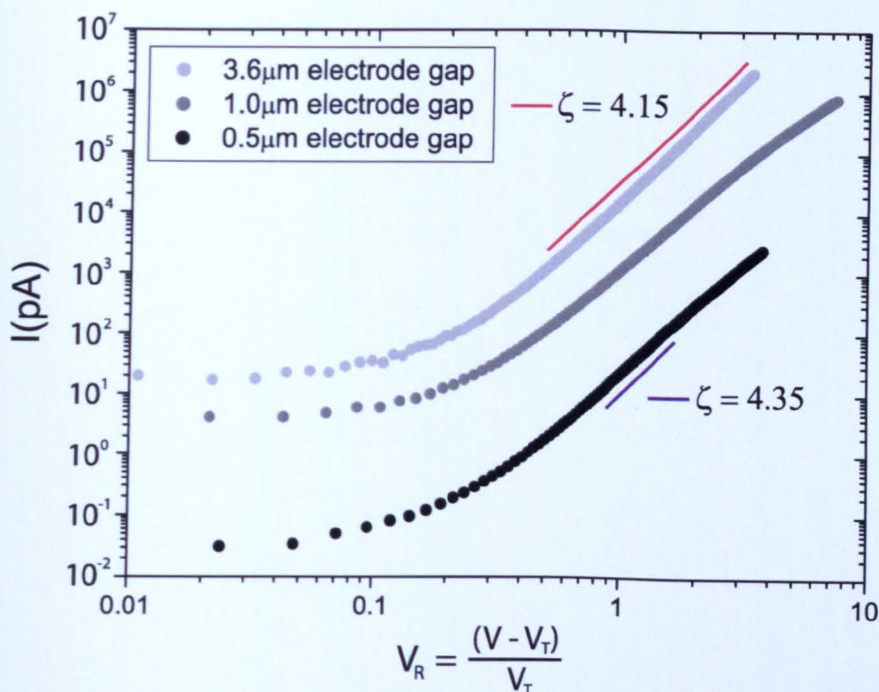
Figure 7.9: Current against reduced voltage for the three electrode spacings on the topologically complex C_8 sample. For the sake of clarity the plots for the $1.0\mu m$ and $3.6\mu m$ electrode gaps are offset from that of the $0.5\mu m$ gap by 2 and 3 decades respectively.

Figure 7.6.

An elongated "transient" regime exists at low voltages $(0.0 < V_T < 0.5)$ followed by a well defined scaling region with values of $\zeta > 4$ $(0.5 < V_T < 2.0)$. For the $0.5\mu m$ and $1.0\mu m$ electrode gaps this scaling region then falls off towards lower values of ζ for $V_T > 2$. Values of ζ obtained in previous experimental studies range from $1.4 < \zeta < 2.0$ for lithographically patterned array of metal dots [103–105], $1.6 < \zeta < 2.1$ for poly-disperse, two-dimensional nanoparticle arrays [112], and $\zeta = 2.25$ in size mono-disperse, structurally ordered nanoparticle arrays [109]. Values of ζ approaching 4 have been observed in single layer nanoparticle films with a coverage of 0.55ML [113]. However, as this coverage value was measured by X-ray photoemission spectroscopy detail concerning the correlation of the level of structural disorder was not available.

The significantly greater values of ζ which we observe are directly linked to the correlated nature of the structural disorder present in the cellular nanoparticle networks. The value of $\zeta = 5/3$ calculated by MW theory for structurally ordered two-dimensional arrays relies on the ability of conduction paths to meander throughout the array in response to the random offset-charge disorder, producing a set of individual conduction paths across the array that has a certain distribution of threshold voltages.

The removal of nanoparticles from a structurally ordered array curtails this meandering of conduction paths. If random nanoparticles are removed, equivalent to uncorrelated structural disorder, this locally curtails the meandering of conduction paths at random points throughout the array, thus producing a narrower distribution of conduction path threshold voltages than for a structurally ordered array. In cellular nanoparticle networks, however, the morphology of the networks means that current paths are constrained within the branches of the network. The correlated nature of branch size and width in the cellular networks produces a set of conduction paths across the array with a much narrower distribution of threshold voltages than in an array with uncorrelated structural disorder. This narrower distribution of path threshold voltages in turn produces a much higher value of the conduction scaling exponent ζ.

7.5 Temperature dependence

The MW theory of transport through arrays of capacitively linked metal dots centered on the extreme of low temperature $T=0$ [100]. Initial studies of the temperature dependence of conductivity through nanoparticle arrays displayed a linear reduction of the array threshold voltage with increasing temperature [114]. This linear dependence of the threshold voltage with increasing

temperature was explained in terms of a reduction in the threshold for conduction through a single nanoparticle by an amount equal to the excess thermal energy $k_b T/e$. Thus the threshold for conduction across the entire array would be reduced by an amount $Nk_b T/e$, where N is the width of the array in units of nanoparticles. Thus the threshold at a temperature T would be given by,

$$V_{th}(T) = V_{th}(0) - Nk_B T/e, \qquad (7.4)$$

and therefore,

$$\frac{dV_{th}}{dT} = -Nk_B/e. \qquad (7.5)$$

This relationship was upheld for the single array (*N=40*) studied by Bezryadin *et. al.* However, a later study by Parthasarathy *et. al.* [115] saw distinct deviations from this relationship for multiple two-dimensional samples with array widths ranging from 27 to 170 nanoparticles.

These results were explained by Parthasarathy *et. al.* [115] and later in more detail by Elteto *et. al.* [117] by once again returning to the seminal theory of MW [100]. In the limit of short screening length the threshold voltage for an array is defined by the path through the array with the minimum number of up-steps in the random offset-charge disorder. Each up-step contributes a value e/C_g, where C_g is the nanoparticle-gate capacitance, or, in the limit of short screening length, the nanoparticle self capacitance.

Importantly, due to the stochastic nature of the charge transport this contribution to the threshold voltage is insensitive to the size of the up-step. Any up-step no matter how small causes an increase in the threshold voltage of e/C_g. Thus, small reductions in the size of up-steps due to increased temper-

ature will have no effect on the size of the threshold voltage.

Reduction in the threshold voltage with increasing temperature comes with the complete removal of up-steps from the lowest resistance path across the array. Using a theory calculating the removal of up-steps based on the broadening of the individual nanoparticle energy bands with increasing temperature, Parthasarathy [115] successfully predicted dV_{th}/dT for numerous experimentally studied arrays. Another important result of [115] was that, by a simple linear translation along the voltage axis, the $I(V)$ curves for an array taken at different temperatures could be made to overlay onto a single master curve. This demonstrated that the non-linear form of the conduction remains unaffected by the linear reduction in threshold caused by increasing temperature.

Further work by Elteto *et. al.* [116] used electron beam patterning to fabricate quasi one-dimensional nanoparticle arrays. A structurally ordered array of thiol passivated gold nanoparticles was selectively exposed to an electron beam. This exposure causes cross linking of the passivating thiol molecules. The cross linked areas of the array now became insoluble in heated toluene, which could be used to remove the unexposed regions of the array.

Using this method arrays approximately 30nm ($\sim$4 nanoparticles) wide and $\sim$500nm in length were produced and their conduction properties studied. Even at array widths of 4 particles, significant non-linearity was observed in the conduction behaviour, with scaling exponent values of $\zeta = 1.95$ obtained, thus demonstrating that significant meandering and branching of conduction pathways is still possible even at this reduced array width. Another important result of this work was that, although the threshold voltage still displayed a linear dependence on temperature, the collapse of $I(V)$ curves for an array at different temperatures on to a single master curve was no longer possible. The

small array widths mean that there are only a limited number of conduction paths through the array.

The thresholds for these paths will be strongly dependent on the configuration of the offset-charge disorder. With increasing temperature the configuration of the offset-charge disorder changes due to the thermally induced repositioning of trapped charges in the substrate. For two-dimensional arrays of similar electrode separation the sheer number of possible conduction paths removes any sensitivity of the overall conduction behaviour to rearrangement of the offset-charge configuration, allowing the collapse of $I(V)$ curves at different temperatures onto a master curve. In the quasi one-dimensional arrays, however, the changes in the configuration of the offset-charge disorder shift the threshold values for the various conduction paths through the array, increasing some and decreasing others. As there are so few possible conduction paths these shifts in the path thresholds induce a strongly temperature dependent functional form of the $I(V)$ curves. This makes the collapse of the $I(V)$ data taken at different temperatures onto a single master curve impossible.

In Figure 7.10 **(a)** the $I(V)$ curves at temperatures between 4.5K and 80K for the 0.5μm electrode gap on the topologically complex C$_8$ passivated sample are shown. Figure 7.10 **(b)** shows an attempt to collapse these curves onto a single master curve by a translation in the voltage axis. From Figure 7.10 **(b)** we can clearly see that a collapse of the $I(V)$ data for different temperatures on to a single master curve is not possible for the topologically complex networks. The form of the non-linear $I(V)$ curve changes with increasing temperature.

This is not particularly surprising given the nature of these cellular networks. The networks consist mainly of branches which are roughly 20nm-30nm in width. Even with the smaller nanoparticle diameter used here in compar-
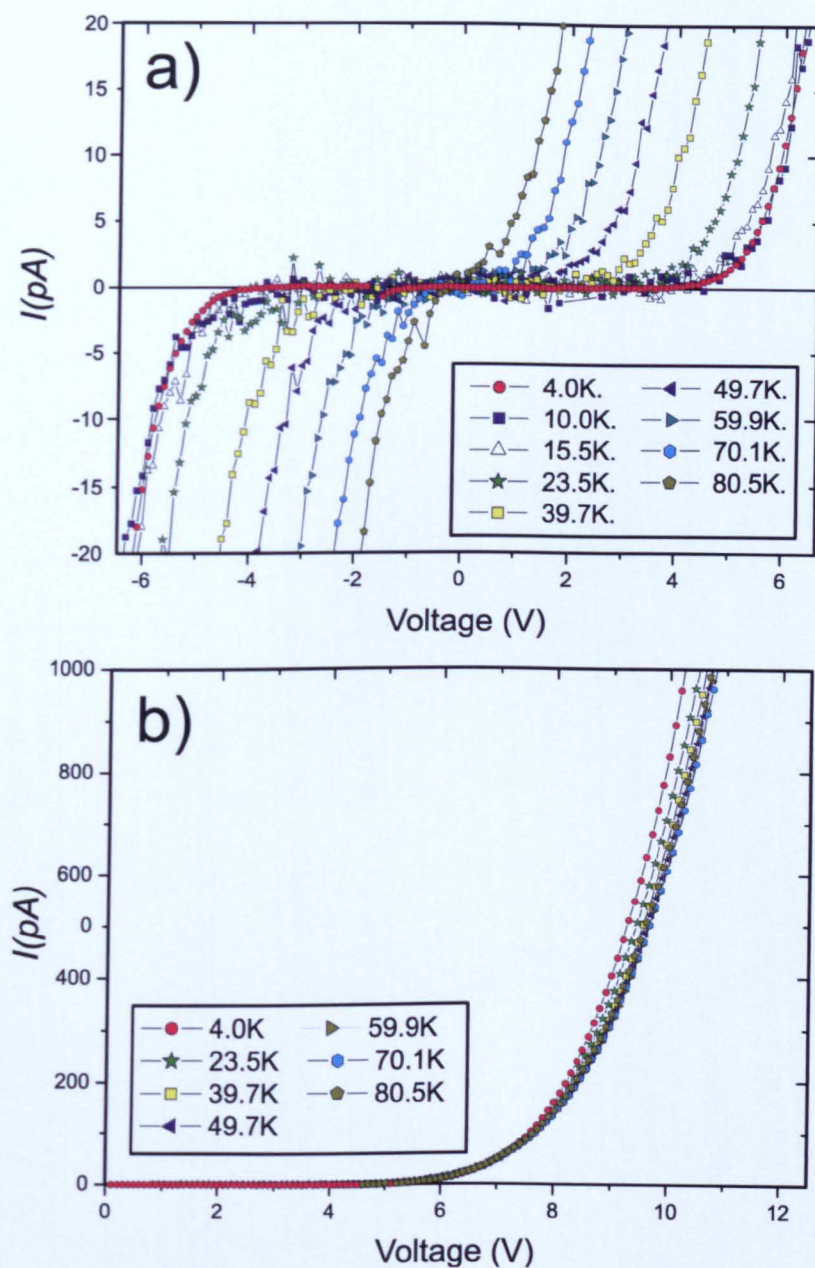
Figure 7.10: *I(V)* data taken at temperatures between 4.5K and 80K for the 0.5μm electrode gap on the topologically complex C_8 sample. **(a)** Shows the unaltered *I(V)* curves for the different temperatures. **(b)** Shows an attempt to collapse the *I(V)* data onto a single master curve by a translation in the voltage axis.

187

ison to [116] (~2nm as compared to ~5.5nm), we still have branches which are between 7 and 10 nanoparticles in width. This is close to the width of the quasi one-dimensional arrays studied in [116]. As such, thermally induced variations in the quenched charge disorder will noticeably alter the form of the non-linear conduction.

In Figure 7.11 we plot the variation of the threshold voltage with temperature for the 0.50μm electrode gap on the topologically complex C_8 sample. From this plot distinct deviations from a purely linear dependence of the threshold voltage on temperature can clearly be seen. This is in sharp contrast to strongly linear relationships between the threshold voltage and temperature that have been observed in previous studies [110, 115–117].
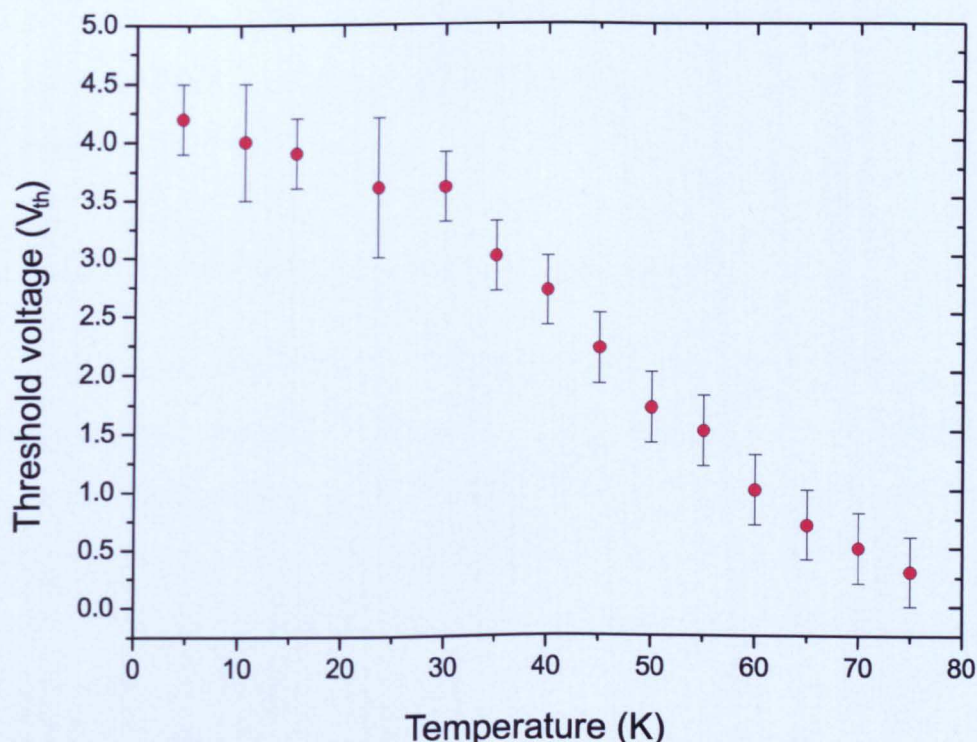
Figure 7.11: Plot displaying the variation of threshold voltage, V_{th}, with temperature for the 0.50μm electrode gap on the topologically complex C_8 sample.

The theoretical basis for a linear dependence of the threshold voltage on

temperature outlined in [115, 117] relies on the assumption of an *uncorrelated* (*i.e.* purely random) distribution of bonds throughout the array. Thus, the conduction may be modelled in terms of percolation through an ordered lattice with broken bonds. The topologically complex cellular nanoparticle networks studied here invalidate this basic assumption. They possess a strongly correlated bond distribution due to their complex morphology. As with the increased values of the conduction scaling exponent discussed earlier, this correlation in the width and length of the individual branches of the network greatly reduces the number of possible conduction paths across the array as compared to a structurally ordered two-dimensional array of the same size. As such, the overall conduction through this greatly reduced number of possible pathways shows a far greater sensitivity to temperature variations, producing the non-linear dependence of the threshold voltage on temperature seen in Figure 7.11.

7.6   EFM of nanoparticle networks

Having used DC conductivity measurements to probe conduction through nanoparticle arrays over a range of temperatures, an effort was now made to use electrostatic force microscopy (EFM) to directly image the motion of charge through nanoparticle networks.

Samples with similar contact arrangements as those studied above were fabricated, although electrode spacings of 10μm were used. EFM was performed on these samples with chromium-coated AFM probes using an Asylum MFP-3D AFM. A standard two pass scanning process was adopted. Topography data were collected on the first pass of the tip. The tip was then raised 50nm from the surface and the same line scanned again. The topographic data

collected in the first scan were used to maintain the tip at a fixed distance from the surface during the second scan.

Any electric field gradients felt by the tip due to electric charges on the surface will affect the image contrast during the second scan. The data collected by the tip during the second scan can thus be used to build up an image of the charge distribution on the surface. In these experiments changes in the phase of the oscillating tip were found to be the most sensitive method of measuring surface charge distributions.

Figure 7.12 shows the results for a C_8 passivated network where (a) shows a standard tapping mode image of the AFM topology, while (b) and (c) show the phase data for the EFM scan for 0V, and 10V, network bias respectively. The planar contacts are to the left and right of the network shown. To apply the bias the right contact is held at the desired voltage, while the left contact is connected to ground.

This particular section of the network was chosen because of the presence of a scratch, probably due to tweezer damage, through the center of the network. This scratch is clearly visible in the topographic data of Figure 7.12 (a). It was hoped that this sharply defined topographic feature would highlight any charge distribution on the surface due to the bias applied to the network.

As a comparison, Figure 7.12 part (b) shows the EFM scan phase data at 0V network bias. The scan is almost completely flat (the scratch in the network is just visible) showing that topology has a minor influence on the EFM scan. Figure 7.12 part (c) shows the phase data for the EFM scan when the network is biased at 10V.

The value of the phase changes gradually from left to right across the network as is to be expected considering the positioning of the planar electrodes
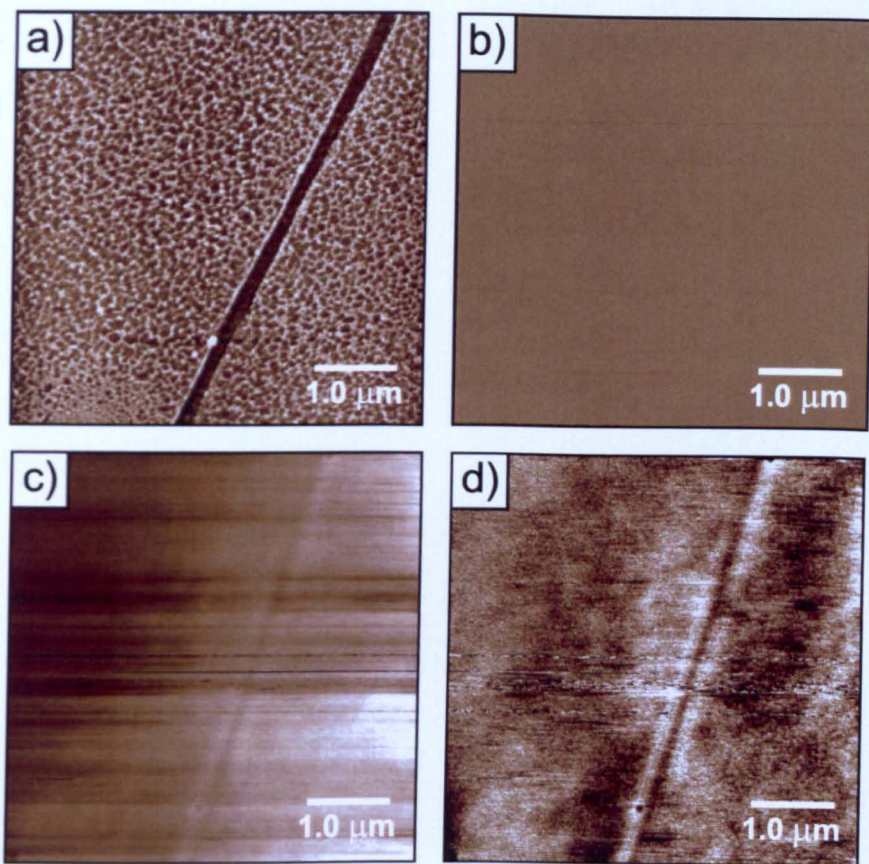
Figure 7.12: The results of EFM experiments on nanoparticle networks. **(a)** Standard tapping mode image of the network topology, the image size is $5.0\mu m \times 5.0\mu m$, the contacts are out of image to the left, and right. **(b)** Phase data for the EFM scan with the network held at a bias of 0V. **(c)** Phase data for the EFM scan with the network held at a bias of 10V. **(d)** Flattened phase data at 10V network bias.

to the left and right of the images shown. In an attempt to discern more detail in the EFM scans, this gradient was removed using the flattening facility provided with the MFP-3D software. The resulting image is shown in Figure 7.12 **(d)**.

If we compare the flattened EFM phase image from Figure 7.12 **(d)** to the topography data from Figure 7.12 **(a)** we can see that some of the small scale detail of the network is visible in the EFM scans. Areas of topographically more densely packed network appear brighter in the EFM image, while cor-
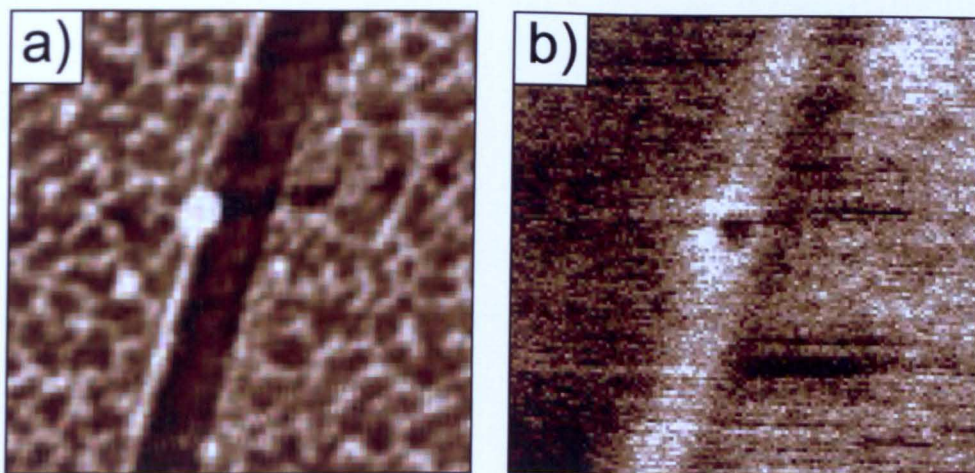
Figure 7.13: Enlargement of a $1.0\mu m^2$ area of the network shown in Figure 7.12, **(a)** shows the topographic data while **(b)** shows the flattened EFM phase data.

respondingly less dense regions appear darker. The edges of the scratch in the network are particularly bright in the EFM image, due to the excellent connectivity in the densely packed line of nanoparticles at the edges of the scratch. Figure 7.13 **(a)** and **(b)** show an enlargement of a $1.0\mu m^2$ area of the network in both topology and flattened EFM phase data. The details of the network showing through into the EFM image are clear

Unfortunately this was all of the detail it was possible to collect with the use of EFM. As the current studies were carried out at room temperature the networks are far from the Coulomb blockade regime. As such we could not expect to observe a charge front advancing across the array as the network bias is increased. As it is these results simply show the more well connected regions of the network are charged to a greater extent when a bias is applied across the network. Future work in this area will focus on the use of EFM/SCM (scanning capacitance microscopy) at cryogenic temperatures. In such experiments it should be possible to observe a charge front moving across a biased nanoparticle network.

7.7 Conclusions

The conduction properties of topologically complex nanoparticle networks have been studied over temperatures in the range 4.5K to 80K. A novel two-stage shadow-mask technique was used to deposit electrical contacts on top of spin-cast nanoparticle networks. This method afforded excellent electrical contact to the network, whilst keeping damage and perturbation of the network morphology to a minimum.

Nanoparticle networks display Coulomb blockade conduction behaviour, requiring a threshold voltage to be exceeded before the onset of conduction. At voltages above threshold conduction is non-linear in fashion. The non-linear conduction can be described by the conduction scaling exponent ζ [100]. The value of the conduction scaling exponent is shown to have a strong dependence not only on the level, but also the correlation, of a network's structural disorder. Nanoparticle networks possessing uncorrelated structural disorder reproduce both the scaling exponents and the deviations from a single power law behaviour that have been observed previously in nanoparticle arrays with similar morphologies [109].

Networks with highly correlated structural disorder produce values for the scaling exponent which are greatly in excess of the majority of previously reported experimental data. The highly correlated nature of the structural disorder in the spin cast nanoparticle networks confines the possible conduction paths through the networks to a much narrower distribution of threshold voltages than for a structurally ordered array. The narrower distribution of threshold voltages thus creates greatly increased values for the conduction scaling exponent.

With increasing temperature the threshold for conduction through the ar-

rays decreases in accordance with the majority of previously reported experimental data. However, whereas in the majority of previous studies this decrease has been linear in nature [110, 115–117], a nonlinear dependence is observed here. Also in contrast to previous studies [115], the functional form of network *I(V)* curves for voltages above threshold shows a marked temperature dependence. This precludes the collapsing of *I(V)* curves taken at different temperatures onto a single master curve by a simple translation in the voltage axis.

Both these effects are once again linked to the highly correlated nature of the structural disorder in cellular nanoparticle networks. The width and length of the branches in the networks are strongly correlated, this correlation narrows the distribution of possible path lengths across the array. The meandering of conduction pathways in response to the quenched charge disorder is also reduced by the pathways being constrained within the branches of the network.

The greatly reduced number of possible conduction pathways across the network is extremely sensitive to thermally induced local rearrangement of the quenched charge disorder. This produces the dependence on temperature in the form of the nonlinear conduction and the nonlinear dependence of the threshold voltage on temperature change.

Finally EFM was used to image the distribution of charge in cellular networks biased at voltages between 0V and 10V. The structural details of the network were clearly visible in the EFM images. The connectivity of the network in different areas controlled the level of charge forced into that area at different bias values.

Chapter 8

Summary and suggestions for further work

8.1 Summary of findings

The primary focus of this thesis has been a study of the formation, properties, and manipulation of far-from-equilibrium nanoparticle assemblies. Simple and highly controllable synthesis methods for colloidal clusters [6], combined with their high stability and unique electronic properties have made metallic nanoparticles a major area of modern scientific research. The central aim of much of this research has been the controlled deposition of such nanoparticles into ordered surface structures, the first step towards their use in functional materials and electronic devices.

Throughout the work described in this thesis, a far-from-equilibrium fabrication route for nanoparticle assemblies has been used. This method involves the spin-casting of nanoparticle solution onto semiconductor substrates. Previous studies have shown that such spin casting techniques can produce a wide array of different nanoparticle network morphologies [11], and, im-

portantly, many of these nanoparticle assemblies possess well-defined correlation lengths. Such far-from-equilibrium techniques have many advantages over other nanoparticle deposition techniques, not least being their simplicity. In order to use such techniques for the controlled deposition of nanoparticle structures the physical mechanism underlying the pattern formation must be studied and understood.

In Chapter 4 some of the many factors which affect the morphology of spin cast nanoparticle networks were studied. These included nanoparticle concentration, the solvent used in nanoparticle solutions, and the nature of the substrate. Some of the possible mechanisms responsible for pattern formation during the spin coating process were discussed, namely dewetting via liquid flow, evaporative dewetting, and the Marangoni effect. Using arguments based on the experimental evidence, the majority of structures which are observed are linked to an evaporative dewetting process such as that discussed by Rabani *et. al.* [52]. Of particular interest were the formation of cellular nanoparticle networks possessing two distinct correlation lengths. Such networks were attributed to two separate regimes of an evaporative dewetting process, one initiated by surface contamination, the other due to the forced evaporation of solvent during the final stages of the spin coating process. Certain structures were also observed which displayed strong evidence supporting the Marangoni effect as a possible formation mechanism.

Chapters 5 and 6 focus on the manipulation and control of far-from-equilibrium nanoparticle networks. Chapter 5 describes the use of an AFM lithography technique to selectively oxidise areas of a hydrogen passivated silicon surface, where lithographic resolution down to ∼50nm was obtained. The morphology of nanoparticle networks spin cast on top of solid oxide pat-

terns was shown to display notable differences to the morphology observed on the rest of the surface. These differences were attributed to the differences in the RMS roughness and the thermal conductivity between the Si and SiO_2 surfaces. Both these factors act to slow the evaporation of solvent on the lithographically patterned oxide areas. This hypothesis was upheld by Monte Carlo simulations carried out by C. P. Martin at the University of Nottingham [82] which accurately reproduced the experimental data. Preferential dewetting of nanoparticle solutions at the edges of oxide patterns was linked to the sharpness of the oxide pattern boundary. This preferential dewetting effect was used to guide the formation of nanoparticle assemblies. Line patterns of oxide were used to initiate dewetting of the nanoparticle solution in desired positions on the surface, forcing the networks to adopt predefined correlation lengths and symmetries.

The *coerced* coarsening of far-from-equilibrium nanoparticle networks was studied in Chapter 6. Repetitive scanning of a nanoparticle network by an AFM probe was used to mechanically drive the network towards equilibrium. This novel coarsening mechanism displayed many of the hallmarks of thermally driven coarsening, most notably that the nanoparticle network structure displayed a high degree of self-similarity during its evolution. The coarsening of interconnected spinodal like structures was linked to probe induced mass transport along the network boundaries, while coarsening of isolated nanoparticle islands was explained in terms of probe-induced cluster diffusion and coalescence.

Chapter 7 centered on the electrical properties of spin cast nanoparticle networks. DC electrical transport measurements were taken over a range of temperatures between 4.5K and 80K. These measurements were used to study the

scaling of the conduction behaviour through far-from-equilibrium nanoparticle assemblies. Values of the conduction scaling exponent were obtained which were far in excess of both theoretically predicted values [100] and previously obtained experimental values [109]. These large values of the conduction scaling exponent were explained in terms of the topological complexity present in the spin-cast nanoparticle networks. The highly correlated nature of the disorder present in the cellular network structures produces a set of conduction paths which has a much narrower distribution of threshold voltages in comparison to the distribution of possible paths across an ordered array. This produces the higher-than-expected values for the scaling exponent. The effect of increasing temperature on the conduction behaviour also shows noticeable departures from that expected for structurally ordered arrays [115]. These differences arise because of the quasi one-dimensional nature of the branches within the nanoparticle network structures. Electrostatic force microscopy was also employed to directly image the charging on a nanoparticle network at room temperature.

8.2 Further work

This work has begun to address the roles that different experimental parameters play during the formation of far-from-equilibrium nanoparticle assemblies. Further work is required to separate the effects of different formation mechanisms such as evaporative dewetting, convective dewetting, and the Marangoni effect. The large number of possible parameters make this an area with vast possibilities for experimental study. An intriguing experiment might involve the use of circular oxide patterns, such as those shown in Chapter 5 (Figure 5.8), to investigate nano-fluidics. As the nanoparticle solution dewets from the

circular oxide line it would be expected to produce a small droplet within the circular pattern. By leaving a small break in the perimeter of the pattern it might be possible to use the Laplace pressure of the droplet to drive nanoparticle solution out of the pattern. This could lead to new ways of controlling not only the evaporation but also the flow of nanoparticle solutions over micron length scales and below.

The mechanically-induced coarsening of nanoparticle networks discussed in Chapter 6 opens up an entirely novel method for the study of coarsening. The remaining question of why mechanical coarsening occurs in networks which are spin cast from certain solvents and not others needs to be answered. In addition, experiments in which the coarsening is mechanically driven at different temperatures are required so that the role which thermal coarsening plays can be separated from purely mechanical coarsening effects.

The study of electrical transport through topologically complex nanoparticle arrays is of particular interest. Observation of the conduction scaling behaviour through a wider range of network morphologies may help to bring about a more quantitative link between the topological nature of the assemblies and their conduction characteristics. Such a study might employ the manipulation techniques discussed in Chapters 5 and 6 to directly control the morphology of nanoparticle networks. Using these techniques it may be possible to perform a truly systematic study of the effect that array topology has on the conduction properties. For example the subtle mechanical coarsening discussed in Chapter 6 might be used to drive a "spinodal" assembly of nanoparticles through several stages of a self-similar evolution. The conduction properties could then be measured at these stages and related to the topological nature of the nanoparticle array. With the use of cryogenic temperature EFM

studies it may also be possible to directly observe the flow of charge across such topologically complex arrays, allowing a deeper understanding of the way current paths across the array are constrained by the array's structure. These experiments are planned within the Nottingham Nanoscience group using a liquid helium temperature SCM (scanning capacitance microscope) which has been developed and built by Dr. C. Mellor.

Bibliography

[1] C. P. Martin, M. O. Blunt, P. J. Moriarty, **Nanoparticle networks on silicon: Self-organized or disorganized?** *Nano. Lett.* **4**, no.12, pp.2389-2392, **(2004)**.

[2] R. P. Feynman, **There's plenty of room at the bottom.** *Eng. Sci.* **(February 1960)**.

[3] M. D. Porter, T. B. Bright, D. L. Allara, C. E. D. Chidsey, **Structural characterization of n-alkyl thiol monolayers on gold by optical ellipsometry, infrared spectroscopy, and electrochemistry.** *J. Am. Chem. Soc.* **109**, no.12, pp.3559-3568, **(1987)**.

[4] C. A. Mirkin, R. L. Letsinger, R. C. Mucic, J. J. Storhoff, **A DNA-based method for rationally assembling nanoparticles into macroscopic materials.** *Nature.* **382**, no.6592, pp.607-609, **(1996)**.

[5] M. C. Cross, P. C. Hohenberg, **Pattern formation outside of equilbrium.** *Rev. Mod. Phys.* **65**, no.3, pp.851-1112, **(1993)**.

[6] M. Brust, M. Walker, D. Bethell, D. J. Schriffrin, R. Whyman, **Synthesis of thiol-derivatised gold nanoparticles in a two-phase liquid-liquid system.** *J. Chem. Soc. Chem. Commun.* **7**, pp.801-802, **(1994)**.

[7] R. P. Andres. J. D. Bielefeld, J. I. Henderson, D. B. Janes, V. R. Kolagunta. C. P. Kubiak, W. J. Mahoney, R. G. Osifchin **Self-assembly of a two-dimensional superlattice of molecularly linked metal clusters.** *Science.* **273**, no.5282, pp.1690-1693, **(1996)**.

[8] C. J. Kiely, J. Fink, M. Brust, D. Bethell, D. J. Schiffrin, **Spontaneous ordering of bimodal ensembles of nanoscopic gold clusters.** *Nature.* **396**, no.6710, pp.444-446, **(1998)**.

[9] G. Ge, L. Brus, **Evidence for spinodal phase separation in two-dimensional nanocrystal self-assembly.** *J. Phys. Chem. B.* **104**, no.41, pp.9573-9575, **(2000)**.

[10] M. Maillard, L. Motte, A. T. Nqo, M. P. Pileni, **Rings and hexagons made of nanocrystals: A Marangoni effect.** *J. Phys. Chem. B.* **104**, no.50, pp.11871-11877, **(2000)**.

[11] P. J. Moriarty, M. D. R. Taylor, M. Brust, **Nanostructured cellular networks.** *Phys. Rev. Lett.* **89**, no.24, pp.248303/1-4, **(2002)**.

[12] N. Rivier, **Statistical crystallography. Structure of random cellular networks.** *Philosop. Mag. B.* **52**, no.3, pp.795-819, **(1985)**.

[13] M. Faraday, **Experimental relations of gold (and other metals) to light.** *Phil. Trans. R. Soc.* **147**, 145 **(1857)**.

[14] G. Frens, **Controlled nucleation for regulation of particle size in monodisperse gold suspensions.** *Nature. Phys. Sci.* **241**, no.105, pp.20-22, **(1973)**.

[15] C. A. Mirkin, **Programming the assembly of two- and three-dimensional architectures with DNA and nanoscale iorganic building blocks.** *Inorg. Chem.* **39**, no.11, pp.2258-2272, **(2000)**.

[16] L. H. Dubois, B. R. Zegarski, R. G. Nuzzo, **Molecular ordering of organosulfur compounds on Au(111) and Au(100) - adsorption from sollution and in ultrahigh-vacuum.** *J. Chem. Phys.* **98**, no.1, pp.678-688, **(1993)**.

[17] F. Schreiber, A. Eberhardt, T. Y. B. Leung, P. Schwartz, S. M. Wetterer, D. J. Lavrich, L. Berman, P. Fenter, P. Eisenberger, G. Scoles, **Adsorption mechanisims, structures, and growth regimes of an archetypal self-assembling system: Decanethiol on Au(111).** *Phys. Rev. B.* **57**, no.19, pp.12476-12481, **(1998)**.

[18] D. V. Leff, P. C. Ohara, J. R. Heath, W. M. Gelbart, **Thermodynamic control of gold nanocrystal size: experiment and theory.** *J. Phys. Chem.* **99**, no.18, pp.7036-7041, **(1995)**.

[19] M. J. Hostetler, J. J. Stokes, R. W. Murray, **Infrared spectroscopy of three-dimensional self-assembled monolayers: N-alkanethiolate monolayers on gold cluster compounds.** *Langmuir.* **12**, no.15, pp.3604-3612, **(1996)**.

[20] L. A. Porter Jr, D. Ji, S. L. Westcott, M. Graupe, R. S. Czernuszewicz, N. J. Halas, T. R. Lee, **Gold and silver nanoparticles functionalized by the adsorption of dialkyl disulfides.** *Langmuir.* **14**, no.26, pp.7378-7386, **(1998)**.

[21] S. Chen. R. W. Murray, **Arenethiolate monolayer protected gold clusters.** *Langmuir.* **15**, no.3, pp.682-689, **(1999)**.

[22] J. R. Hook, H. E. Hall, **Solid state physics, second edition.** *Wiley,* **(1991)**.

[23] M. A. Kastner, **Artificial atoms.** *Phys. Today.* **46**, no.1, pp.24-31, **(1993)**.

[24] R. Palmer, **Welcome to clusterworld.** *New. Sci.* **2070**, **(1997)**.

[25] G. Schon. U. Simon, **A fascinating new field in colloid science: small ligand-stabilized metal clusters and their possible application in microelectronics Part II: Future directions.** *Colloid. Polymer. Sci.* **273**, no.3, pp.202-218, **(1995)**.

[26] E. Boubour, R. B. Lennox, **Insulating properties of self-assembled monolayers monitored by impedance spectroscopy.** *Langmuir.* **16**, no.9, pp.4222-4228, **(2000)**.

[27] M. H. Devoret, H. Grabert, **Single charge tunneling-coulomb blockade phenomena in nanostructures.** *NATO ASI series vol 294,* New york:Plenum, **(1992)**.

[28] J. A. G. Dubois, J. W. Gerritsen, S. E. Shafranjuk, E. J. G. Boon, G. Schmid. H. van Kempen, **Coulomb staircase and quantum size effects in tunnelling spectroscopy on ligand stabilized metal clusters.** *Europhys. Lett.* **33**, no,4, pp.279-284, **(1996)**.

[29] R. P. Andres, T. Bein, M. Dorogi, S. Feng, J. I. Henderson, C. P. Kubiak, W. Mahoney, R. G. Osifchin, R. Reifenberger, **"Coulomb staircase" at**

room temperature in a self-assembled molecular nanostructure. *Science.* **272.** no.5266, pp.1323-1325, **(1996)**.

[30] J. Israelachvili, **Intermolecular and surface forces.** *Academic press.* **(1991)**.

[31] F. London, *Trans. Fraday. Soc.* **33**, pp.8, **(1937)**.

[32] J. Israelachvili, D. Tabor, **The measurement of van der Waals dispersion forces in the range 1.5 to 130 nm.** *Proc. R. Soc. Lond.* **A 331**, pp.1938, **(1972)**.

[33] H. B. G. Casimir, D. Polder, **The influence of retardation on the London-Van der Waals Forces.** *Phys. Rev.* **73**, no.4, pp.360-372, **(1948)**.

[34] H. C. Hamaker, **The London-Van der Waals attraction between spherical particles.** *Physica.* **4**, pp.1058-1072, **(1937)**.

[35] I. M. Lifshitz, **The theory of molecular attractive forces between solids.** *Soviet. Phys. JETP.* **2**, no.1, pp.73-83, **(1956)**.

[36] D. B. Hough, L. R. White **The calculation of Hamaker constants from Lifshitz theory with applications to wetting phenomena.** *Adv. Coll. Int. Sci.* **14**, no.1, pp.3-41, **(1980)**.

[37] L. Bergström, **Hamaker constants of inorganic materials.** *Adv. Coll. Int. Sci.* **70**, pp.125-169, **(1997)**.

[38] P. H. Beton, A. W. Dunn, and P. Moriarty, **Manipulation of C_{60} molecules on a Si surface.** *App. Phys. Lett.* **67**, no.8, pp.1075-1077, **(1995)**.

[39] J. W. Cahn, **Phase separation by spinodal decomposition in isotropic systems.** *j. Chem. Phys.* **42**, no.1, pp.93-99, **(1965)**.

[40] R. A. L. Jones, **Soft condensed matter.** *Oxford University Press,* **(2002)**.

[41] I. Prigogine, R. Lefever, **Symmetry breaking instabilities in dissapative systems. II.** *J. Chem. Phys.* **48**, no.4, pp.1695-1700, **(1968)**.

[42] G. Binnig, H. Rohrer, **Scanning tunnelling microscopy.** *Helve. Physica. Acta.* **55**, no.6, pp.726-35, **(1982)**.

[43] G. Binnig, C. F. Quate, C. Gerber, **Atomic force microscope.** *Phys. Rev. Lett.* **56**, no.9, pp.930-933, **(1986)**.

[44] R. Wiesendanger, **Scanning probe microscopy and spectroscopy: methods and application.** *Cambridge University Press.* **(1994)**.

[45] Q. Zhong, D. Inniss, K. Kjoller, V. B. Elings, **Fractured polymer silica fiber surface studied by tapping mode atomic-force microscopy.** *Surf. Sci.* **290**, no.1-2, pp.L688-L692, **(1993)**.

[46] Digital Instruments, Santa Barbara, CA.

[47] S. S. Wong, E. Joselevich, A. T. Woolley, C. L. Cheunq, C. M. Lieber, **Covalently functionalized nanotubes as nanometre-sized probes in chemistry and biology.** *Nature.* **394**, no.6688, pp.52-55, **(1998)**.

[48] Y. Martin, D. W. Abraham, H. K. Wickramasinghe, **High-resolution capacitance measurement and potentiometry by force microscopy.** *App. Phys. Lett.* **52**, no.13, pp.1103-1105, **(1988)**.

[49] X. M. Lin, H. M. Jaeger, C. M. Sorensen, K. J. Klabunde, **Formation of long-range-ordered nanocrystalsuperlattices on silicon nitride substrates.** *J. Phys. Chem. B.* **105**, no.17, pp.3353-3357, **(2001)**.

[50] C. Stowell, B. A. Korgel, **Self-assembled honeycomb networks of gold nanocrystals.** *Nano. Lett.* **1**, no.11, pp.595-600, **(2001)**.

[51] B. A. Korgel, D. Fitzmaurice, **Condensation of ordered nanocrystal thin films.** *Phys. Rev. Lett.* **80**, no.16, pp.3531-3534, **(1998)**.

[52] E. Rabani, D. A. Reichman, P. L. Geissler, L. E. Brus, **Drying-mediated self-assembly of nanoparticles.** *Nature.* **426**, no.20, pp.271-274, **(2003)**.

[53] S. Narayanan, J. Wang, X. M. Lin, **Dynamical self-assembly of nanocrystal superlattices during colloidal droplet evaporation by in situ small angle x-ray scattering.** *Phys. Rev. Lett.* **93**, no.13, pp.135503, **(2004)**.

[54] J. Huang, F. Kim, A. R. Tao, S. Conner, P. Yang, **Spontaneous formation of nanoparticle stripe patterns via dewetting.** *Nature. Mat.* **4**, no.12, pp.896, **(2005)**.

[55] T. P. Bigioni, X. M. Lin, T. T. Nguyen, E. I. Corwin, T. A. Witten, H. M. Jaeger, **Kinetically driven sel assembly of highly ordered nanoparticle monolayers.** *Nature. Mat.* **5**, no.4, pp.265-270, **(2006)**.

[56] P. J. Durston, J. Schmidt, R. E. Palmer, **Scanning tunneling microscopy of ordered coated cluster layers on graphite.** *App. Phys. Lett.* **71**, no.20, pp.2940-2942, **(1997)**.

[57] D. Meyerhofer, **Characteristics of resist films produced by spinning.** *J. Appl. Phys.* **49**, no.7, pp.3393-3397, **(1978)**.

[58] G. Ge, L. E. Brus, **Fast surface diffusion of large disk-shaped nanocrystal aggregates.** *Nano. Lett.* **1**, no4., pp.219-222, **(2001)**.

[59] A. Vrij, J. Th. G. Overbeek, **Rupture of thin liquid fims due to spontaneous fluctuations in thickness.** *J. Am. Chem. Soc.* **90**, no.12, pp.3074-3078, **(1968)**.

[60] E. Ruckenstein, R. K. Jain, **Spontaneous rupture of thin liquid-films.** *J. Chem. Soc. Fraday. Trans. II.* **70**, pp.132-147, **(1974)**.

[61] R. Seemann, S. Herminghaus, K Jacobs, **Dewetting patterns and molecular forces: A reconcilliation.** *Phys. Rev. Lett.* **86**, no.24, pp.5534-5537, **(2001)**.

[62] J. Bischof, D. Scherer, S. Hermighaus, P. Leiderer, **Dewetting modes of thin metallic films: nucleation of holes and spinodal dewetting.** *Phys. Rev. Lett.* **77**, no.8, pp.1536-1539, **(1996)**.

[63] R. Xie, A. Karim, J. F. Douglas, C. C. Han, R. A. Weiss **Spinodal dewetting of thin polymer films.** *Phys. Rev. Lett.* **81**, no.6, pp.1251-1254, **(1998)**.

[64] U. Thiele, M. Mertig, W. Pompe, **Dewetting of an evaporating thin liquid film: heterogeneous evaporation and surface instability.** *Phys. Rev. Lett.* **80**, no.13, pp.2869-2872, **(1998)**.

[65] A. Sharma, J. Mittal, R. Verma, **Instability and dewetting of thin films induced by density variations.** *Lang.* **18**, no.26, pp.10213-10220, **(2002)**.

[66] D. R. Lied, ed., **CRC Handbook of Chemistry and Physics, Internet Version 2006,** <http://www.hbcpnetbase.com>. Taylor and Francis, Boca Ranton, FL, **(2006)**.

[67] A. M. Higgins, R. A. L. Jones, **Aniisotropic spinodal dewetting as a route to self-assembly of patterned surfaces.** *Nature.* **404**, no.6777, pp.476-478, **(2000)**.

[68] J. M. Calvert, **Lithographic patterning of self-assembled films.** *J. Vac. Sci. Tech. B.* **11**, no.6, pp.2155-2163, **(1993)**.

[69] E. Meyer, H. G. Braun, **Controlled dewetting processes on microstructured surfaces - a new procedure for thin film microstructuring.** *Macromol. Mater. Eng.* **276/277**, pp.44-50, **(2000)**.

[70] Z. Zhang, Z. Wang, R. Xing, Y. Han, **Patterning thin polmer films by surface-directed dewetting and pattern transfer.** *Polymer.* **44**, pp.3737-3743, **(2003)**.

[71] K. Karagupta, A. Sharma, **Templating of thin films induced by dewetting on patterned surfaces.** *Phys. Rev. Lett.* **86**, no.20, pp.4536-4539, **(2001)**.

[72] K. Karagupta, A. Sharma, **Creation of ordered patterns by dewetting of thin films on homogeneous and heterogeneous substrates.** *J. Coll. Interf. Sci.* **245**, pp.99-155, **(2002)**.

[73] K. Karagupta, A. Sharma, **Mesopatterning of thin liquid films by templating on chemically patterned complex substrates.** *Langmuir.* **19**, pp.5153-5163, **(2003)**.

[74] L. L. Sohn, R. L. Willett, **Fabrication of nanostructures using atomic-force-microscopy-based lithography.** *App. Phys. Lett.* **67**, no.11, pp.1552-1554, **(1995)**.

[75] R. D. Piner, J. Zhu, F. Xu, S. H. Hong, C. A. Mirkin, **"Dip-pen" nanolithography.** *Science.* **283**, no.5402, pp.661-663, **(1999)**.

[76] J. A. Dagata, J. Schneir, H. H. Harary, C. J. Evans, M. T. Postek, J. Bennett, **Modification of hydrogen-passivated silicon by a scanning tunneling microscope.** *App. Phys. Lett.* **56**, no.20, pp.2001-2003, **(1990)**.

[77] V. A. Burrows, Y. J. Chabal, G. S. Higashi, K. Raghavachari, S. B. Christman, **Infrared-spectroscopy of Si(111) surfaces after HF treatment - hydrogen termination and surface-morphology.** *App. Phys. Lett.* **53**, no.11, pp.998-1000, **(1988)**.

[78] G. S. Higashi, R. S. Becker, Y. J. Chabal, A. J. Becker, **Comparison of Si(111) surfaces prepared using aqueous solutions of NH$_4$F versus HF.** *App. Phys. Lett.* **58**, no.15, pp.1656-1658, **(1991)**.

[79] A. E. Gordon, R. T. Fayfield, D. D. Litfin, T. K. Higman, **Mechanisms of surface anodization produced by scanning probe microscopes.** *J. Vac. Sci. Tech. B.* **13**, no.6, pp.2805-2808, **(1995)**.

[80] R. Garcia, M. Calleja, **Patterning of silicon surfaces with non-contact atomic force microscopy: field-induced formation of**

nanometer-size water bridges. *J. App. Phys.* **86**, no.4, pp.1898-1903, **(1999)**.

[81] Private communications with C. van den Brom, the University of Groningen.

[82] Monte Carlo simulations of the evaporative dewetting of nanoparticle solutions on patterned substrates was carried out by C. P. Martin at the University of Nottingham using modifications to the code detailed in [1].

[83] edt. C. Domb, J. L. Lebowitz, **Phase transitions and critical phenomena.** *Academic press, New York.* **(1993)**.

[84] H. A. Furukawa, **A dynamic scaling assumption for phase-separation.** *Adv. Phys.* **34**, no.6, pp.703-750, **(1985)**.

[85] A. J. Bray, **Coarsening dynamics of phase-separating systems.** *Phil. Trans. Roy. Soc London A.* **361**, no.1805, pp.781-791, **(2003)**.

[86] W. Z. Ostwald, *Phys. Chem.* **37**, pp.385, **(1901)**.

[87] I. M. Lifshitz, V. V. Slyosov, **The kinetics of precipitation from supersaturated solid solutions.** *J. Phys. Chem.* **19**, no.1-2 pp.35-50, **(1961)**.

[88] M. von Smoluchowski, *Phys. Z.* **17**, pp.585, **(1916)**.

[89] V. M. Kaganer, K. H. Ploog, **Coarsening of facetted two-dimensional islands by dynamic coalescence.** *Phys. Rev. B.* **73**, no.11, pp.115425-1-115425-8, **(2006)**.

[90] F. Family, T. Vicsek, **Scaling of the active zone in the Eden process on percolation networks and the ballistic deposition model.** *J. Phys. A.* **18**, no.2, pp.L75-L81, **(1985)**.

[91] W. W. Pai, A. K. Swan, Z. Y. Zhang, J. F. Wendelken, **Island diffusion and coarsening on metal (100) surfaces.** *Phys. Rev. Lett.* **79**, no.17, pp.3210-3213, **(1997)**.

[92] C. DeW. van Siclen, **Single jump mechanisms for large cluster diffusion on metal surfaces.** *Phys. Rev. Lett.* **75**, no.8, pp.1574-1577, **(1995)**.

[93] S. V. Khare, N. C. Bartlet, T. L. Einstein, **Diffusion of monolayer adatom vacancy clusters: Langevin analysis and Monte Carlo simulations of their Brownian motion.** *Phys. Rev. Lett.* **75**, no.11, pp.2148-2151, **(1995)**.

[94] J. M. Wen, S. L. Chang, J. W. Burnett, J. W. Evans, P. A. Thiel, **Diffusion of large two-dimensional clusters on Ag(100).** *Phys. Rev. Lett.* **73**, no.19, pp.2591-2594, **(1994)**.

[95] G. S. Grest, D. J. Srolovitz, **Structure and evolution of quenched Ising clusters.** *Phys. Rev. B.* **30**, no.9, pp.5150-5155, **(1984)**.

[96] H. -J. Ernst, F. Fabre, J. Lapujoulade, **Observation of dynamic scaling in "spinodal decomposition" in two dimensions.** *Phys. Rev. Lett.* **69**, no.3 , pp.458-461, **(1992)**.

[97] D. A. Huse, **Corrections to late-stage behaviour in spinnodal decomposition: Lifshitz-Slyozov scaling and Monte Carlo simulations.** *Phys. Rev. B.* **34**, no.11 , pp.7845-7850, **(1986)**.

[98] Private communications with M. Brust, The Nanochemistry Group at The University of Liverpool.

[99] S. Roux, H. J. Herrmann, **Disorder-induced nonlinear conductivity.** *Europhys. Lett.* **4**, no.11, pp.1227-1231, (**1987**).

[100] A. A. Middleton, N. S. Wingreen, **Collective transport in arrays of small metallic dots.** *Phys. Rev. Lett.* **71**, no.19, pp.3198-3201, (**1993**).

[101] U. geigenmuller, G. Schon, **Single electron effects in arrays of normal tunnel junctions.** *Europhys. Lett.* **10**, no.8, pp.191-200, (**1989**).

[102] M. Kardar, G. Parisi, Y. C. Zhang, **Dynamic scaling of growing interfaces.** *Phys. Rev. Lett.* **56**, no.9, pp.889-892, (**1986**).

[103] C. I. Duruöz, R. M. Clarke, C. M. Marcus, J. S. Harris. Jr, **Conduction threshold switching, and hysteresis in quantum dot arrays.** *Phys. Rev. Lett.* **74**, no.16, pp.3237-3240, (**1994**).

[104] Ç. Kurdak, A. J. Rimberg, T. R. Ho, J. Clarke, **Activated transport and scaling behaviour in the current-voltage characteristics and Coulomb-blockade oscillations of two-dimensional arrays of metallic islands.** *Phys. Rev. B.* **57**, no.12, pp.R6842-R6845, (**1997**).

[105] A. J. Rimberg, T. R. Ho, J. Clarke, **Scaling behaviour in the current-voltage characteristic of one- and two-dimensional arrays of small metallic islands.** *Phys. Rev. Lett.* **74**, no.23, pp.4714-4717, (**1995**).

[106] W. Chen, H. Ahmed, K. Nakazoto, **Coulomb Blockade at 77K in nanoscale metallic islands in a lateral nanostructure.** *App. Phys. Lett.* **66**, no.24, pp.3383-3384, **(1995)**.

[107] C. T. Black, C. B. Murray, R. L. Sandstrom, S. Sun, **Spin dependent tunneling in self-assembled cobalt-nanocrystal superlattices.** *Science.* **290**, no.5494, pp.1131-1134, **(2000)**.

[108] L. Clarke, M. N. Wybourne, M. Yan, S. X. Cai, J. F. W. Keana, **Transport in gold cluster structures defined by electron-beam lithography.** *App. Phys. Lett.* **71**, no.5, pp.617-619, **(1997)**.

[109] R. Parthasarathy, X. M. Lin, H. M. Jaeger, **Electronic transport in metal nanocrystal arrays: The effect of structural disorder on scaling behaviour.** *Phys. Rev. Lett.* **87**, no.18, pp.186807/1-4, **(2001)**.

[110] M. G. Ancona, S. E. Kooi, W. Kruppa, A. W. Snow, E. E. Foos, L. J. Whitman, **Patterning of narrow Au nanocluster lines using V_2O_5 nanowire masks and ion-beam milling.** *Nano. Lett.* **3**, no.2, pp.1335-138, **(2003)**.

[111] R. W. Rendell, M. G. Ancona, W. Kruppa, **Electron transport in nanocluster films with rndom voids.** *IEEE Trans. Nanotech.* **2**, no.2, pp.75-81, **(2003)**.

[112] M. N. Wybourne, L. Clarke, M. D. Yan, S. X. Cai, L. O. Brown, J. Hutchison, J. W. F. Keana, **Coulomb-blockade dominated transport in patterned gold-cluster structures.** *Jap. J. Appl. Phys.* **36**, no.12B, pp.7796-7800, **(1997)**.

[113] M. G. Ancona, W, Kruppa, R. W. Rendell, A. W. Snow, D. Park, J. B. Boos, **Coulomb blockade in single-layer Au nanocluster films.** *Phys. Rev. B.* **64**, no.3, pp.033408, **(2001)**.

[114] A. Bezryadin, R. M. Westerveld, M. Tinkham, **Self-assenbled chains of graphitized carbon nanoparticles.** *App. Phys. Lett.* **74**, no.18, pp.2699-2701, **(1999)**.

[115] R. Parthasarathy, X. M. Lin, K. Elteto, T. F. Rosenbaum, H. M. Jaeger, **Percolating through networks of random thresholds: Finite temperature electron tunneling in metal nanocrystal arrays.** *Phhys. Rev. Lett.* **97**, no.7, pp.076801- 1-4, **(2004)**.

[116] K. Elteto, X. M. Lin, H. M. Jaeger, **Electronic transport in quasi-one-dimensional arrays of gold nanocrystals.** *Phys. Rev. B.* **71**, no.20, pp.205412, **(2005)**.

[117] K. Elteto, E. G. Antonyan, T. T. Nguyen, H. M. Jager, **Model for the onset of transport in systems with distributed thresholds for conduction.** *Phys. Rev. B.* **71**, no.6, pp.064206, **(2005)**.

List of Figures

List of Tables

.